



**HAL**  
open science

# Cobaltates in the high-doping regime: Insights from first-principles calculations and extended dynamical mean-field theory

Sophie Chauvin

► **To cite this version:**

Sophie Chauvin. Cobaltates in the high-doping regime: Insights from first-principles calculations and extended dynamical mean-field theory. Condensed Matter [cond-mat]. Université Paris Saclay (COmUE), 2016. English. NNT: 2016SACLX110 . tel-01527477

**HAL Id: tel-01527477**

**<https://pastel.hal.science/tel-01527477v1>**

Submitted on 24 May 2017

**HAL** is a multi-disciplinary open access archive for the deposit and dissemination of scientific research documents, whether they are published or not. The documents may come from teaching and research institutions in France or abroad, or from public or private research centers.

L'archive ouverte pluridisciplinaire **HAL**, est destinée au dépôt et à la diffusion de documents scientifiques de niveau recherche, publiés ou non, émanant des établissements d'enseignement et de recherche français ou étrangers, des laboratoires publics ou privés.

NNT : 2016SACLX110

THÈSE DE DOCTORAT  
DE L'UNIVERSITÉ PARIS-SACLAY  
PRÉPARÉE À L'ÉCOLE POLYTECHNIQUE

Ecole doctorale n°564  
Physique de l'Ile-de-France  
Spécialité de doctorat : Physique  
par

**MME SOPHIE CHAUVIN**

Etude des cobaltates fortement dopés par calculs premiers principes et théorie du champ moyen dynamique étendue

Thèse présentée et soutenue à Palaiseau, le 14 Décembre 2016.

Composition du Jury :

M.	PATRICK RINKE	Professeur associé Aalto University	(Président du jury)
M.	CHRIS MARIANETTI	Professeur associé Columbia University	(Rapporteur)
M.	FRANK LECHERMANN	Professeur TU Hamburg Harburg	(Rapporteur)
M.	MARK VAN SCHILFGAARDE	Professeur King's College London	(Examineur)
M.	ALESSANDRO NICOLAOU	Chercheur Synchrotron Soleil	(Examineur)
Mme	CLAUDIA RÖDL	Chercheuse Fr.-Schiller-Universität Jena	(Membre invité)
Mme.	SILKE BIERMANN	Professeure Ecole Polytechnique	(Directrice de thèse)
Mme.	LUCIA REINING	Directrice de recherche Ecole Polytechnique	(Directrice de thèse)



*Alors commença entre le médecin et l'archidiacre un de ces prologues congratulateurs qui précédaient à cette époque, selon l'usage, toutes conversations entre savants, et qui ne les empêchaient pas de se détester le plus cordialement du monde. Au reste, il en est encore de même aujourd'hui, toute bouche de savant qui complimente un autre savant est un vase de fiel emmiellé.*

— Victor Hugo, *Notre-Dame de Paris*, V, 1



# Remerciements

Je tiens d'abord à remercier mes directrices de thèse, Lucia et Silke, qui ont eu l'audace de proposer un sujet à cheval entre leurs deux domaines de recherche. Elles ont toujours fait preuve d'enthousiasme et d'ouverture d'esprit, et m'ont laissé beaucoup de liberté dans mon travail.

Je voudrais ensuite adresser mes sincères remerciements à Thomas et Claudia. Ils m'ont menée avec patience à travers les méandres des fermions fortement corrélés et des calculs *ab initio*. Ils ont aussi été de bon conseil pendant les moments difficiles qui ne manquent pas de jalonner une thèse.

Je remercie également les membres de mon jury pour s'être déplacés, avoir lu et commenté ma thèse. J'ai beaucoup apprécié discuter avec eux avant et lors de la soutenance.

Je remercie le service informatique et le secrétariat du CPHT et du LSI pour leur compétence et leur disponibilité.

Merci à Olivier, Michel et Hartmut pour m'avoir montré toutes les astuces de TRIQS.

Je remercie les deux groupes du LSI et du CPHT pour leur accueil toujours chaleureux. Ils ont su créer un environnement de travail agréable et une animation scientifique stimulante.

En vrac, merci à Pascal, Priyanka, Yusuke, Philipp, Jakob, Swarup, Steffen, Ambroise, Marcello, Jan, Feng, Nicolas, Walter, Giorgia, Marilena, Marco, Sky, Lucie, Francesco, Matteo, Christine, Valérie, Igor, Lorenzo, Martin, Pierluigi, Stefano, Ilia, ainsi que tous les organisateurs du YRM et les membres du groupe du Collège de France.

Tout au long de ma thèse, j'ai pu me changer les idées grâce à la musique. Je me dois de remercier l'Orchestre du plateau de Saclay, ainsi que Brahms, Dvořak, Prokofiev et Beethoven.

Merci à Ghislaine pour m'avoir permis de faire zoom arrière.

Je n'oublierai pas le rôle joué par ma famille qui m'a toujours encouragée, même lorsqu'elle ne comprenait pas mes choix de parcours. Enfin, merci à Frédéric pour sa précieuse présence.



# Résumé

Comme de nombreux autres oxydes de métaux de transition lamellaires, les cobaltates dopés au sodium,  $\text{Na}_x\text{CoO}_2$ , présentent un riche diagramme de phase. Les nombreuses instabilités (magnétiques, de charge) qui les caractérisent seraient notamment le fruit des corrélations électroniques. Dans cette thèse, nous nous intéressons au cas fortement dopé  $x = 2/3$  (proche de la limite de l'isolant de bande). Expérimentalement, ce composé est sujet à une disproportion de charge locale sur les atomes de cobalt, ce qui en fait un terrain d'étude privilégié pour le calcul des fonctions de corrélation de charge. Le traitement théorique de ce système est difficile à bien des égards. D'abord, la corrélation électronique demande de recourir à des approximations avancées. Ensuite, le système est sensible aux détails microscopiques, tels que transcrits dans la structure électronique réelle. Dans cette thèse, nous abordons ces deux aspects, à travers une approche sur modèle et une approche *ab initio*.

Nous examinons d'abord l'effet des corrélations au niveau d'un modèle sur réseau triangulaire, pertinent pour les cobaltates. La compétition entre les interactions de Coulomb locale et non-locale sur un modèle de Hubbard étendu donne lieu à des fluctuations de charge, que nous traitons grâce à la théorie du champ moyen dynamique étendue. Nous dressons le diagramme de phase de notre modèle en fonction des interactions locale et non-locale. Celui-ci présente une transition du second ordre entre un état métallique homogène et une phase ordonnée de charge. Nous calculons les observables à une et deux particules dans la phase homogène, et nous déterminons l'effet des corrélations sur ces deux types d'observables. Nous interprétons ces résultats comme des conséquences du fort dopage. Nous identifions une région du diagramme de phase où la partie statique de l'interaction de Coulomb écrantée devient négative. Enfin, nous montrons comment incorporer un terme de Fock non-local à ces calculs, et nous détaillons son effet sur le diagramme de phase et sur les observables physiques.

En complément de notre approche sur modèle, nous étudions les détails microscopiques du matériau réel grâce à la théorie de la fonctionnelle de la densité. Nous analysons le rôle de l'hybridation avec l'oxygène et des processus de saut électronique sur la structure de bandes pour les plans de cobalt-oxygène. Nous clarifions l'effet de certains paramètres physiques, tels que le dopage au sodium, l'arrangement cristallin ou le magnétisme, sur la structure électronique. Puis nous calculons la susceptibilité de charge selon les premiers principes, selon des approximations suggérées par notre étude de modèle sur réseau.

La comparaison entre les calculs sur modèle et *ab initio* montre que ces approches se

## Remerciements

---

complètent l'une l'autre. D'une part, le modèle permet de dégager les approximations pertinentes pour le calcul des fonctions de corrélation de charge. D'autre part, les calculs *ab initio* et la compréhension des processus microscopiques sont le préalable à la construction d'un modèle réaliste et prédictif.

# Abstract

As many other layered transition-metal oxides, sodium-doped cobaltates,  $\text{Na}_x\text{CoO}_2$ , present a rich phase diagram. They display numerous instabilities (magnetic, charge-order), originating most likely from electronic correlations. In this thesis, we focus on the case  $x = 2/3$ , in the strong-doping limit (close to the band-insulating limit). An experimentally-observed charge disproportionation on the cobalt atoms makes this particular composition an interesting playground to study charge-correlation functions. The theoretical treatment of this system is difficult in several aspects. In order to capture electronic correlations, one needs to resort to advanced non-perturbative approaches. Also, the system is sensitive to its microscopic details, as encoded in the real electronic structure. This is why, in this thesis, we adopt model as well as *ab initio* approaches to address both these issues.

We first study the effect of correlations at the model level, on a triangular lattice, specifically designed for the cobaltates. The interplay between local and non-local Coulomb interactions gives rise to charge fluctuations, which we capture using the Extended Dynamical Mean-Field Theory. We establish the phase diagram of our model as a function of local and non-local interactions. It displays a second-order phase transition between a homogeneous metallic phase, and a charge-ordered phase. We compute one and two-particle observables in the homogeneous phase, and we analyse how they are influenced by correlations. We show that our findings can be understood as a consequence of the strong doping. We find a region of the phase diagram where the static screened Coulomb interaction becomes negative. Finally, we show how to incorporate a non-local Fock term in the calculation of the self-energy, and how it influences the phase diagram and the physical observables.

Next, in order to complement the model approach, we study the microscopic details of the real sodium-cobaltates by using Density-Functional Theory. We analyse the effect of oxygen hybridisation and electronic hopping processes on the band structure of cobalt-oxygen planes. We study the effects of sodium doping, crystal structure and magnetism, on the band structure of this material. Then, we compute the charge susceptibility from first principles in the independent-particle approximation and in the random-phase approximation. We use the insight gained from the model calculation to discuss these results.

The comparison between the model and the *ab initio* calculations shows that these approaches are complementary. The model enables us to define the best approximations

## Remerciements

---

for the calculation of charge correlation functions. The *ab initio* calculations, and the detailed understanding of microscopic electronic processes are the prerequisite for a model that is both realistic and predictive.

# Contents

Preface	3
<b>I Introduction</b>	<b>5</b>
<b>1 Phenomenology of correlated metals</b>	<b>7</b>
1.1 Landau's Fermi-liquid theory . . . . .	7
1.2 Mott transition and the atomistic viewpoint . . . . .	12
1.3 Actual materials: complex transition metal oxides . . . . .	13
<b>2 Introduction to sodium-doped cobaltates</b>	<b>17</b>
2.1 Crystallography . . . . .	17
2.2 Local atomic states . . . . .	18
2.3 Experimental phase diagram . . . . .	20
2.4 Electronic structure of $\text{Na}_x\text{CoO}_2$ . . . . .	24
<b>3 Theoretical methods for electronic structure</b>	<b>33</b>
3.1 Introduction to some physical observables . . . . .	34
3.1.1 <i>Ab initio</i> approaches . . . . .	34
3.1.2 Lattice model approaches . . . . .	35
3.2 Auxiliary systems . . . . .	36
3.3 Ground-state properties: Density functional theory (DFT) . . . . .	38
3.4 Accessing spectroscopy: Dynamical mean-field theory (DMFT) . . . . .	39
3.4.1 DMFT . . . . .	39
3.4.2 Extended dynamical mean-field theory . . . . .	41
3.4.3 Fock + EDMFT . . . . .	45
3.4.4 <i>GW</i> + EDMFT . . . . .	46
<b>II Extended Dynamical Mean-Field Theory for the Extended Hubbard Model on a Triangular Lattice at High Doping</b>	<b>47</b>
<b>4 A model for the cobaltates</b>	<b>49</b>
4.1 Capturing charge fluctuations from non-local Coulomb interactions . . . . .	50

## Contents

---

4.2	A realistic model . . . . .	51
4.3	Choice of interaction parameters . . . . .	53
<b>5</b>	<b>Extended Dynamical Mean-Field Theory in Practice</b>	<b>55</b>
5.1	Implementation of the self-consistency condition . . . . .	55
5.2	The impurity solver . . . . .	58
<b>6</b>	<b>Results in the high-doping regime</b>	<b>61</b>
6.1	Computed phase diagram . . . . .	61
6.2	One-particle observables . . . . .	65
6.3	Two-particle observables . . . . .	68
6.3.1	The impurity susceptibility . . . . .	69
6.3.2	Auxiliary quantities: polarisation, screened Coulomb interaction and dynamical bare interaction . . . . .	72
6.4	Discussion . . . . .	74
<b>III</b>	<b><i>Ab-initio</i> study of strongly-doped cobaltates</b>	<b>75</b>
<b>7</b>	<b>Electronic structure of doped <math>\text{CoO}_2</math> planes</b>	<b>77</b>
7.1	Presentation of the $\text{CoO}_2$ planes . . . . .	78
7.2	Effect of doping on the band structure: a rigid band shift? . . . . .	79
7.3	Band structure of doped $\text{CoO}_2$ . . . . .	81
7.3.1	The electron-doped band structure . . . . .	81
7.3.2	Comparison to the model non-interacting band . . . . .	81
7.3.3	Orbital-projected density of states . . . . .	82
7.3.4	Partial-charge distribution in real space . . . . .	83
7.3.5	Fermi surface . . . . .	85
7.4	Effect of the oxygen stacking on the band structure . . . . .	86
<b>8</b>	<b>Impact of real-structure effects</b>	<b>87</b>
8.1	Effect of sodium doping . . . . .	87
8.1.1	The tripled unit cell: presentation . . . . .	87
8.1.2	Sodium: a pure electron-donor? . . . . .	89
8.1.3	Does sodium doping change the low-energy band structure? . . . .	90
8.1.4	Local valence and sodium-induced charge disproportionation . . . .	93
8.2	Effect of the crystalline structure: interplanar distance and oxygen positions	94
8.2.1	interplanar distance . . . . .	95
8.2.2	Oxygen positions . . . . .	96
8.3	Magnetism . . . . .	97

<b>9</b>	<b><i>Ab initio</i> susceptibilities</b>	<b>99</b>
9.1	The non-interacting susceptibility: $\chi_0$ . . . . .	99
9.1.1	The <i>ab initio</i> non-interacting susceptibility . . . . .	100
9.1.2	Comparison to the model . . . . .	103
9.2	The susceptibility in the random-phase approximation (RPA): $\chi_{\text{RPA}}$ . . . . .	105
9.2.1	The <i>ab initio</i> RPA susceptibility . . . . .	105
9.2.2	Comparison to the model . . . . .	109
9.3	Discussion . . . . .	111
<b>IV Conclusion</b>		<b>115</b>
<b>10 Conclusion and perspectives</b>		<b>117</b>
<b>Appendices</b>		<b>119</b>
<b>A Conventions</b>		<b>121</b>
A.1	Notations . . . . .	121
A.1.1	Time and frequencies . . . . .	121
A.1.2	Space and momentum . . . . .	121
A.1.3	Operators . . . . .	121
A.1.4	Units . . . . .	122
A.2	Fourier transforms . . . . .	122
A.2.1	Time-frequency domain . . . . .	122
A.2.2	Space domain . . . . .	122
A.3	Propagators . . . . .	123
<b>B The cobalt 3d orbitals in the octahedral environment</b>		<b>125</b>
B.1	Rotation of the 3d orbitals . . . . .	125
B.2	Model for the Co( $a_{1g}$ )-O hybridised complex . . . . .	128
<b>C Negative screening in the Hubbard dimer</b>		<b>131</b>
<b>D Susceptibilities</b>		<b>133</b>
D.1	Analytical expressions . . . . .	133
<b>Bibliography</b>		<b>147</b>



# Preface

The study of sodium-doped cobaltates dates back to the 1970's, when Fouassier *et al.*, from the University of Bordeaux, described a new layered oxide [1], of chemical formula  $\text{Na}_x\text{CoO}_2$  (where  $x$  denotes sodium content,  $0 \leq x \leq 1$ ). This new compound consists of a stacking of  $\text{CoO}_2$  sheets, between which sodium ions are intercalated.

Later on, the discovery of the technological possibilities offered by the cobaltates stimulated intensive research. In 1997, a large thermoelectric power was measured at sodium content  $x = 1/2$  by Terasaki *et al.* [2]. In 2003, superconductivity was reported by Takada *et al.* in a hydrated compound, of formula  $\text{Na}_x\text{CoO}_2 \cdot y\text{H}_2\text{O}$  ( $x \approx 0.35$ ,  $y \approx 1.3$ ), where water was intercalated between the  $\text{CoO}_2$  planes [3].

On a broader perspective, transition-metal oxides (a family to which the cobaltates belong) offer a wealth of technological possibilities, including high-temperature superconductivity for cuprates, colossal magnetoresistance for manganites, or relevance for batteries for lithium cobaltates. Yet, the study of materials with  $3d$  electrons still offers fundamental challenges to both experimentalists and theoreticians.

What is at stake in these materials and makes their study complicated is electronic correlation. An example of classical correlation is when people take the métro: most people try to avoid each other, and do not sit close to someone else. The motion of the passengers is correlated; crowd phenomena may appear under certain situations. This happens because people see each other. The collective behaviour of a correlated system is not the result of the addition of independent single-agent behaviour. In an electronic system, the Pauli principle has to be additionally taken into account. Correlations arise as a consequence of the Coulomb interaction. We broadly consider that electronic correlation is anything beyond an independent-particle picture. More specifically, correlation can be defined as anything beyond Hartree-Fock.

As Anderson puts it in his 1972 paper: “More is different” [4]. The many-body problem is complex, and correlation can lead to critical phenomena. This means that even if the elementary laws of nature are known, collective behaviour can be surprising. This is true for two reasons. First, nature finds itself in a complicated symmetry-broken state, where many symmetries of the elementary laws have been broken. Second, as

clarified by the renormalisation group [5], close to transitions, some microscopic details may not be relevant. Correlations in a many-body system lead to emergent behaviour and complexity.

In order to tackle many-body correlated problems, a strong belief has emerged that it is necessary to couple qualitative and numerical aspects, that they are intertwined. This is best summed up by a conversation between Fitzgerald and Hemingway, later reported by Anderson [4]: “The rich are different from us. - Yes, they have more money.” Quantitative differences ultimately lead to qualitative differences. This is true particularly in systems where a minute change in a parameter leads to drastic changes in the physical properties. Therefore, there is an ongoing effort to describe and compute the electronic structure of materials from first principles, from the fundamental laws of nature. The *ab initio* task is to take into account the realistic details of each specific material, and ideally to solve a many-body Schrödinger equation for electrons in a given potential. Of course, it is impossible to perform this task exactly; the goal of the *ab initio* project is to design the best approximations, that can best capture correlation effects.

Several approaches have emerged, with different types of approximations. In density-functional theory (DFT) [6, 7], and in many-body perturbation theory (MBPT) [8], many electrons are treated explicitly, over a wide window of energy. However, some correlation effects are usually neglected. In dynamical mean-field theory (DMFT) [9], only some low-energy degrees of freedom are included explicitly, but correlations are treated explicitly. In a context where many computational methods have emerged to treat the many-electron problem, it is important to draw connections between them.

In this thesis, we take the sodium cobaltates as a case study to make connections between these two established types of methods: the first-principles methods, used in the framework of DFT and MBPT, and the methods for strong correlations derived from DMFT. The cobaltates offer a challenging playground, even for these state-of-the-art techniques. As we will see, cobaltates display many competing degrees of freedom (of either structural or electronic origin), some of them occurring at similar energy scales. They lead to a particularly rich phase diagram, as a function of sodium content. Interestingly, the strongly-doped region (sodium content  $x > 1/2$ ), where the system is closest to a band insulator, and far away from the half-filling limit, displays some of the most intriguing phases. In this highly-doped regime, metallicity coexists with a plethora of phenomena, among which thermoelectricity, charge disproportionation, magnetic ordering...

In this thesis, we set our focus on the strongly-doped region, and in particular on the special case of  $x = 2/3$ . This sodium content has attracted particular attention, because a specific charge-ordering pattern was discovered in nuclear magnetic resonance experiments by Alloul *et al.* [10].

In particular, we aim at exploring the following questions: How can we describe and understand the electronic structure of the cobaltates at the sodium content  $x = 2/3$ ? What can we say about the charge-disproportionation at  $x = 2/3$ ? More generally, what insight can we gain from first-principle methods and DMFT-based calculations on model Hamiltonians, respectively, and how can we benefit from a joint study using both approaches?

We focus on two different types of observables. First, we want to obtain one-particle spectra, that can be compared to photoemission experiments. Second, assuming that the charge correlator is a central quantity to monitor charge disproportionation, we compute charge susceptibilities.

In Part I, we describe the general background of our topic and of the methods. Then, our approach is twofold. In Part II, the cobaltates are treated as a single-band, extended Hubbard model from a strongly-correlated perspective. This corresponds to assuming that the details of the high-energy physics do not matter much for the low-energy properties. In terms of renormalisation group ideas, this means that most microscopic details are irrelevant degrees of freedom at low-energy: they merely renormalise effective low-energy parameters. In Part III, we come back to the real electronic structure of the cobaltates, which we treat using first principles. We describe the main physical elementary processes behind the electronic structure. We take the perspective that some microscopic details can actually become central, even when looking at low energies. At the end of this thesis, we synthesise the insights gained from both approaches.



# Introduction **Part I**



# 1 Phenomenology of correlated metals

In this chapter, we look at general features of correlated metals. Indeed, except for the particular sodium content  $x = 1/2$ , sodium cobaltates are metallic over the whole experimental phase diagram. Therefore, we give some notions about correlated metals in the following.

Contrary to an insulator, a metal has a Fermi surface. It can feature excitations of arbitrarily low energy, across the Fermi level. In terms of bands, the Fermi level lies within the band. There is no gap, contrary to an insulator or a semiconductor. In the rest of this thesis, we will refer to low energies as energies close to the Fermi energy.

Good references for the topics of this chapter include the book by Kittel [11] for the general formalism; the book by Pines and Nozières [12], the lecture by Georges [13] and the review by Imada, Fujimori and Tokura [14] for more advanced notions.

## 1.1 Landau's Fermi-liquid theory

Treating correlations requires to go beyond the Hartree-Fock single-particle approach. However, effective single-particle descriptions (such as from DFT within the Kohn-Sham approach) are still the initial step to many techniques in the field of correlated fermionic systems. When computing excitations, a particle is assumed to move from an occupied single-particle state towards an empty single-particle state. How can this give a reasonable description of correlated systems? Strictly speaking, a many-body state results from the entanglement of many Slater determinants. What makes effective single-particle descriptions so successful? In this section, we describe how two ingredients, namely screening and Landau's Fermi liquid theory, save the independent-electron representation as an effective low-energy description of electronic excitations.

In a typical system with  $3d$  electrons, the bandwidth and hence the kinetic energy, is of the order of the electron volt. As for the interaction energy, the largest contribution

typically comes from the on-site matrix element. This bare repulsion is estimated as:

$$u \sim \int d\mathbf{r}d\mathbf{r}' |\chi_L(\mathbf{r} - \mathbf{R})|^2 \frac{e^2}{|\mathbf{r} - \mathbf{r}'|} |\chi_L(\mathbf{r}' - \mathbf{R})|^2, \quad (1.1)$$

where  $\chi_L(\mathbf{r} - \mathbf{R})$  can be thought of as a Wannier function centered around an atom at position  $\mathbf{R}$ . The resulting bare interaction energy is of the order of tens of electron volts. Hence, the bare Coulomb interaction cannot be thought of as a small perturbative parameter. The first ingredient saving the independent-particle representation is screening. The interaction between two electrons is effectively screened by all the other particles. Hence, the effective, screened interaction is of the order of a few electron volts. Additionally, in a metal, the screened interaction is short-ranged and typically takes a Yukawa form in the long-distance limit.

The second ingredient is the theory of Fermi liquids [15, 16, 17]. It emerged from the question: What is conserved from the non-interacting system, when continuously turning on the electron-electron interaction? Fermi-liquid theory assumes an adiabatic connection between the non-interacting low-energy spectrum (where states take the form of Slater determinants) and the many-body one. Hence, as long as low-energy physics is concerned, a Fermi liquid resembles a non-interacting system. More precisely, in the absence of a phase transition and close to the Fermi surface, there is a one-to-one correspondence between one-particle excitations of a non-interacting system and of the interacting one.

The adiabatic connection can be justified by analysing the scattering rate of an electron close to the Fermi surface or, equivalently, its lifetime. Let us assume the system takes the form of a homogeneous electron gas, with a well-defined Fermi surface. Let us analyse the lifetime of an additional electron with momentum  $\mathbf{k}$  and energy  $\epsilon_{\mathbf{k}}$ , added slightly above the Fermi surface (where the chemical potential is given by  $\mu$ ). Due to the electron-electron interaction, this electron will scatter: it will create electron-hole pairs across the Fermi sea. In the case where the effective interaction is screened and short-ranged, as in a metal, the details of the scattering rate can be derived from Fermi's golden rule and the lifetime  $\tau_{\mathbf{k}}$  of the additional electron is:

$$\frac{1}{\tau_{\mathbf{k}}} \propto \varepsilon_{\mathbf{k}}^2 + \pi^2 T^2. \quad (1.2)$$

Eq. (1.2) encodes the phase space accessible for electron-hole pair creation across the Fermi surface. Eq. (1.2) also means that the closer the additional particle lies to the Fermi surface, the sharper it is defined, with a longer lifetime. A finite temperature  $T$  enlarges the phase space for particle-hole transitions, hence the second term in Eq. (1.2).

The fact that a particle created at the Fermi surface can exist over an arbitrarily long time leads naturally to the notion of quasiparticle. Quasiparticles look like non-interacting particles and are at the basis of the description of low-energy excitations. Close to the Fermi-surface, they are well-defined and long-lived. They merely differ from non-

interacting particles, because they have renormalised masses (the quasiparticles are heavier) and are weakly interacting.

The renormalisation of the quasiparticle mass, as well as the finite lifetime, can both be captured within the more general framework of Green's functions and self-energies. Let us first give a brief overview on Green's functions and self-energies.

In a many-body system, one generally wants to look at more aggregated quantities than the many-body wave-function. The many-body wave-function is a tremendously complex object and is not even needed for the description of experiments. One of the strategies is to deal with propagators. One-particle Green's functions (in short: Green's functions) correspond to one-particle propagators: in imaginary-time, the Green's function is defined as  $G_{ij}(\tau) = -\langle \mathcal{T}_\tau c_i(\tau) c_j^\dagger(0) \rangle$ . The symbol  $\mathcal{T}_\tau$  is the time ordering operator. It describes the propagation of a particle created at time 0 and annihilated at time  $\tau$ .

In a non-interacting system, the Green's function  $G_0$  can be easily expressed in terms of the single-particle spectrum. It has peaks at single-particle energies. In an interacting system, however, the expression for  $G$  involves the full many-body spectrum. In order to quantify exchange and correlation effects in the interacting system, one defines the self-energy  $\Sigma$  via the Dyson equation:

$$G^{-1}(\mathbf{k}, \omega) = G_0^{-1}(\mathbf{k}, \omega) - \Sigma(\mathbf{k}, \omega). \quad (1.3)$$

By switching on the Coulomb interaction, the motion of the (quasi)-particles is modified, with respect to the non-interacting case. The self-energy describes this effect.

Let us analyse the Green's function and the self-energy in the case of a Fermi liquid. In a single-band system or in the homogeneous electron gas, the non-interacting Green's function behaves as:

$$G_0(\mathbf{k}, \omega) = \frac{1}{\omega - \epsilon_{\mathbf{k}} + \mu}. \quad (1.4)$$

The electron dispersion is given by the equation  $\omega_{\mathbf{k}} - \epsilon_{\mathbf{k}} + \mu = 0$ . The non-interacting Fermi-surface is defined as the set of momenta  $\mathbf{k}_F$  such that  $\omega_{\mathbf{k}_F} = 0$ .

Since the low-energy excitations of the non-interacting and Fermi-liquid systems are the same, then the poles of both Green's functions should have the same structure. In the Fermi liquid, the self-energy remains finite and a pole in the interacting Green's function obeys:

$$\omega = \epsilon_{\mathbf{k}} + \Sigma(\mathbf{k}, \omega). \quad (1.5)$$

If we restrict our description to the vicinity of the Fermi surface, where the Fermi-liquid

description is valid, then we can Taylor-expand the self-energy:

$$\text{Re } \Sigma(\mathbf{k}, \omega) \approx \text{Re } \Sigma(\mathbf{k} = \mathbf{k}_F, \omega = 0) - b_{\mathbf{k}_F} \omega + a(\mathbf{k}_F)(\mathbf{k} - \mathbf{k}_F), \quad (1.6a)$$

$$\text{Im } \Sigma(\mathbf{k}, \omega) \approx -\Gamma \omega^2 + \zeta(\mathbf{k}_F)(\mathbf{k} - \mathbf{k}_F)^2. \quad (1.6b)$$

The fact that the imaginary part of the self-energy goes as  $\omega^2$  is directly connected to the quasiparticle lifetime in Eq. (1.2). Eq. (1.6) provides an analytical form for the self-energy for small  $\omega$ . This analytical form will be useful to understand the low-energy behaviour of the self-energies in Part II. Injecting the Taylor expansion of the self-energy, Eq. (1.6), into the Dyson equation for the Green's function, Eq. (1.3), the Green's function for the interacting system takes the form:

$$G(\mathbf{k}, \omega) \approx \frac{Z_{\mathbf{k}_F}}{\omega - \epsilon^*(\mathbf{k} - \mathbf{k}_F) + \tilde{\mu} + i(Z_{\mathbf{k}_F} \Gamma \omega^2 - Z_{\mathbf{k}_F} \zeta(\mathbf{k}_F)(\mathbf{k} - \mathbf{k}_F)^2)}, \quad (1.7)$$

where we have defined the quasiparticle renormalisation factor:

$$Z_{\mathbf{k}_F} = \frac{1}{1 + b_{\mathbf{k}_F}}, \quad (1.8)$$

the renormalised dispersion

$$\epsilon^*(\mathbf{k} - \mathbf{k}_F) \approx Z_{\mathbf{k}_F} [\epsilon_{\mathbf{k}} + a(\mathbf{k}_F)(\mathbf{k} - \mathbf{k}_F)] \quad (1.9)$$

and the renormalised chemical potential

$$\tilde{\mu} = Z_{\mathbf{k}_F} [\mu - \text{Re } \Sigma(\mathbf{k} = \mathbf{k}_F, \omega = 0)]. \quad (1.10)$$

A necessary condition for the validity of the Fermi-liquid picture is that  $\epsilon^* \gg \text{Im } \Sigma$  for small  $\omega$  and small  $\mathbf{k} - \mathbf{k}_F$ . This is satisfied if  $Z_{\mathbf{k}_F} > 0$ .

To connect the quasiparticle renormalisation factor,  $Z$ , to the mass enhancement, one rewrites the renormalised dispersion:

$$\epsilon^*(\mathbf{k} - \mathbf{k}_F) \approx Z_{\mathbf{k}_F}(\mathbf{k} - \mathbf{k}_F) \cdot [\nabla_{\mathbf{k}} \epsilon_{\mathbf{k}} + a(\mathbf{k}_F)]. \quad (1.11)$$

The effective mass (tensor),  $m_{\alpha\beta}^*$  corresponds to the curvature of the renormalised dispersion, such that, assuming an isotropic system:

$$\frac{m^*}{m} = \frac{v_{F0}}{v_{F0} + a(\mathbf{k}_F)} \frac{1}{Z}, \quad (1.12)$$

where  $m$  is the bare electron mass and  $v_{F0} = \partial \epsilon_{\mathbf{k}} / \partial \mathbf{k} |_{\mathbf{k}=\mathbf{k}_F}$  is the bare Fermi velocity. In a Fermi liquid, interactions typically make the quasiparticles heavier.

In order to make connection to the lifetime of the quasiparticle, let us express the spectral

function, as measured in photoemission experiments:  $A(\mathbf{k}, \omega) = -\frac{1}{\pi} \text{Im } G(\mathbf{k}, \omega)$ :

$$A(\mathbf{k}, \omega) = -\frac{1}{\pi} \frac{\text{Im } \Sigma(\mathbf{k}, \omega)}{[\omega - \epsilon_{\mathbf{k}} - \text{Re } \Sigma(\mathbf{k}, \omega)]^2 + [\text{Im } \Sigma(\mathbf{k}, \omega)]^2}. \quad (1.13)$$

The spectrum thus has a Lorentzian shape, with

$$A(\mathbf{k}, \omega) = \frac{Z_{\mathbf{k}}}{\pi} \frac{[-Z_{\mathbf{k}} \text{Im } \Sigma(\mathbf{k}, \omega)]}{[\omega - \epsilon^*(\mathbf{k} - \mathbf{k}_F)]^2 + [Z_{\mathbf{k}} \text{Im } \Sigma(\mathbf{k}, \omega)]^2}. \quad (1.14)$$

$Z_{\mathbf{k}}$  is also called the quasi-particle residue and corresponds to the spectral weight of the quasiparticle peak.  $Z_{\mathbf{k}} \text{Im } \Sigma$  is the quasiparticle lifetime, translated in a broadening of the quasi-particle peak. It is directly connected to the imaginary part of the self-energy.

A typical photoemission spectrum for a non-interacting system and for a Fermi liquid is shown on Fig. 1.1. For the non-interacting case, the Dirac ( $\delta$ ) peaks correspond to single-particle excitations. For the Fermi-liquid case, the  $\delta$  peaks become broader Lorentzians, as in Eq. (1.14). The spectral weight carried by these quasi-particle peaks is the fractional number  $Z$ . The rest of the spectral weight is transferred to higher-energy satellites.

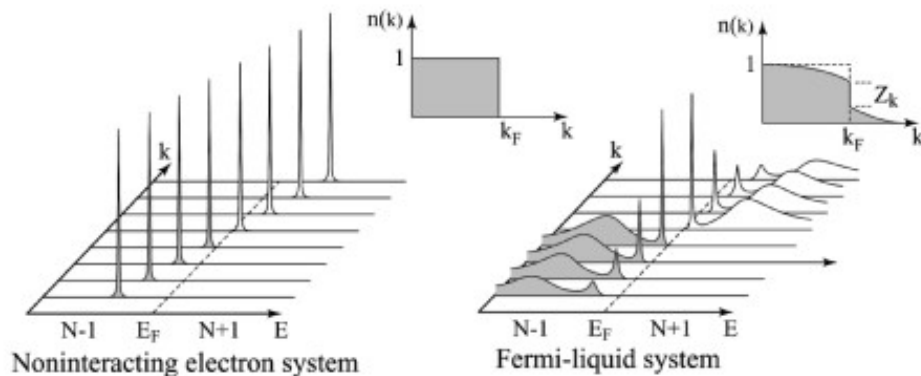


Figure 1.1: Schematic view of a photoemission spectrum, extracted from Ref. [18]. The left panel shows the spectrum of a non-interacting system. It is characterised by dispersive,  $\delta$ -shaped particle peaks, with occupation 1. The corresponding zero-temperature Fermi-Dirac distribution function is represented above. The right panel shows the spectrum for an interacting, Fermi-liquid-like system. The quasiparticle peaks, corresponding to single-particle-like excitations, carry a fractional weight  $Z$ , while the rest of the weight is carried by the incoherent part of the spectrum, with features called satellites. The interacting, zero-temperature distribution function is represented above. The quasiparticle distribution function is step-like, as in the non-interacting case. The height of the step is fractional and corresponds to  $Z_{\mathbf{k}}$ .

## 1.2 Mott transition and the atomistic viewpoint

As attractive as the Fermi-liquid description may be, it cannot explain all of the phenomenology of systems with partially-filled bands. We have stressed that the adiabatic connection of Landau's Fermi-liquid theory was valid in the absence of a phase transition. The Mott transition is a case where the effect of interactions is most spectacular, where the system goes from metallic to insulating behaviour due to the interactions. The Mott phenomenon was first experimentally detected in NiO, where a low conductivity was measured [19]. Mott and Peierls later explained that this was due to the blocking of electrons in real space, due to the strong interaction [20].

In order to understand the Mott phenomenon, it is important to understand the nature of the duality between wave and particle in narrow-band systems. In band theory, the single-particle states are often labelled by their momentum quantum number,  $\mathbf{k}$ . Their motion is then described in reciprocal space. This is most adapted when the single-particle wave functions are delocalised in real space. In a narrow-band system, with  $3d$  or  $4f$  valence bands, the effective bands are weakly dispersive. A weak dispersion in momentum space translates into a strong localisation in real space. In a narrow-band system, the valence electrons hence spend a lot of time in the vicinity of a specific atomic site. The corresponding wave-functions are better labelled by an atomic site. It is important to keep both descriptions in mind: the delocalised, wave-like description in reciprocal space and the localised, particle-like description in real space. The real-space picture puts back the atoms at the centre of the description of materials.

The easiest model capturing this wave-particle duality is the single-band Hubbard model, derived independently by Hubbard [21, 22, 23], Kanamori [24] and Gutzwiller [25]:

$$\mathcal{H} = -t \sum_{\langle i,j \rangle \sigma} (c_{i\sigma}^\dagger c_{j\sigma} + h.c.) + U \sum_i n_{i\uparrow} n_{i\downarrow}, \quad (1.15)$$

where  $c_{i\sigma}^\dagger, c_{i\sigma}$  represent creation and annihilation operators of electrons at site  $i$  and spin  $\sigma$ , respectively.  $n_{i\sigma} = c_{i\sigma}^\dagger c_{i\sigma}$  is the density per spin  $\sigma$ .  $\mathcal{H}$  denotes a Hamiltonian. The Hubbard Hamiltonian has two parameters:  $t$  is the hopping amplitude and  $U$  is a local repulsion term. The Hubbard model is expressed on a lattice (the lattice sites  $i$  representing the atoms) and looks much simpler than a full, many-body Hamiltonian. Yet, it is the fundamental model for strong correlations. As a many-body model, it is very complicated to handle. It contains a kinetic part, parametrised by  $t$ , describing the delocalisation of quasiparticles due to hopping processes. The kinetic part roughly encodes the one-body part of the full electronic Hamiltonian (kinetic part and external potential part). The Hubbard model also contains an interaction part, parametrised by  $U$ . In Eq. (1.15), the interaction part is purely local. In a metal, this is justified by the fact that the Coulomb interaction is strongly screened, such that the resulting electron-electron interaction is not long-ranged anymore.

### 1.3. Actual materials: complex transition metal oxides

---

At half-filling (i.e., in a single-band model as in Eq. (1.15), with an average filling of one electron per lattice site), the system can undergo a metal-insulator transition, called a Mott transition. At low  $U$ , the system is in a metallic state, due to the partial band occupancy, as in a Fermi liquid. When  $U$  is increased, the cost of a double on-site occupancy becomes unfavourable (see interacting part of Eq. (1.15)) and electrons will localise. In the Mott-insulating state, each electron is blocked on a specific site; the electronic motion is prevented, in order to avoid double-occupancy. This picture of an insulator is drastically different from the picture of a band insulator. A Mott insulator, in the absence of interactions, would be a metal. Whereas a Fermi liquid corresponds to a renormalisation factor  $Z > 0$ , a Mott insulator corresponds to the extreme case  $Z \rightarrow 0$ .

The Mott transition gives another perspective on correlations, in a statistical sense. In the non-interacting case, at half-filling, the expectation value  $\langle n_{i\uparrow}n_{i\downarrow} \rangle$  becomes separable:  $\langle n_{i\uparrow}n_{i\downarrow} \rangle = \langle n_{i\uparrow} \rangle \langle n_{i\downarrow} \rangle = 1/4$ . On the insulating side, however, the local densities  $\langle n_{i\sigma} \rangle$  are the same as in the metal, but  $\langle n_{i\uparrow}n_{i\downarrow} \rangle = 0$ . The expectation value  $\langle n_{i\uparrow}n_{i\downarrow} \rangle$  is not separable in the paramagnetic Mott state.

Fig. 1.2 shows a local spectral function through a Mott transition on the Bethe lattice. According to the value of  $U$ , there are two regimes: a metallic and an insulating regime. The metallic regime is characterised by a quasiparticle peak at the Fermi energy ( $\omega = 0$ ). When  $U$  increases, two correlation satellites appear on each side of the quasiparticle peak. These satellites are called Hubbard bands. Ultimately, the quasiparticle peak disappears and all the spectral weight is transferred to the two Hubbard bands. The system is a Mott insulator: it features a gap at the Fermi energy ( $\omega = 0$ ). The two Hubbard bands are separated by an energy of  $U$ , roughly. This spectrum, with two Hubbard bands, is exactly the spectrum of an isolated atom. In the Mott-insulating state, the whole solid has turned into a sum of isolated atoms; the effect of the solid is merely encoded in the broadening of the Hubbard bands.

### 1.3 Actual materials: complex transition metal oxides

Complex oxides consisting of transition metal atoms are currently the subject of intense research and offer a vast diversity of interesting phenomena. These phenomena, that can lead to important technological applications, include metal-insulator transitions [28], high-temperature superconductivity [29, 30], multiferroicity [31, 32, 33] and colossal magnetoresistance [34, 35]. The variety of these compounds relies, among others, on the many possible lattice structures and on the fact that the transition metal ions can accommodate multiple oxidation states. Heterostructuring has opened yet a new dimension [36], with the effect of quantum confinement. This wealth of combinations has triggered a field of engineering of compounds with novel electronic properties, which can be controlled by small external perturbations. To name a few, the physical properties of transition-metal oxides can be tuned by pressure, doping, external magnetic fields or

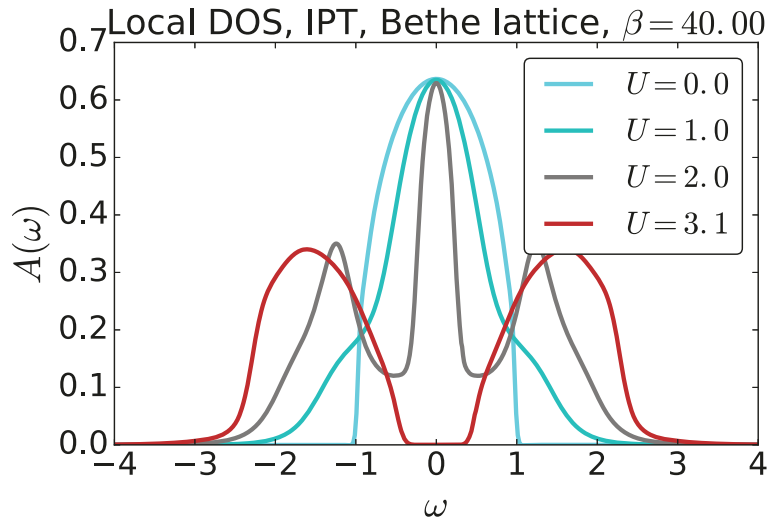


Figure 1.2: The Mott transition, on the (infinite-dimensional) Bethe lattice. The energy values are renormalised by the value of  $t = 1$ . The figure displays the local spectral function. The Mott transition occurs between  $U = 2$  and  $U = 3.1$ . The figure is obtained from an iterated perturbation theory (IPT) solver [26]. The algorithm was written using the TRIQS toolbox [27].

temperature.

In transition-metal oxides, the Fermi level lies close to, or within the transition metal  $3d$  bands. On a transition metal atom, the atomic wavefunctions of the  $3d$  shell are the only ones with an orbital quantum number  $l = 2$ . The  $3d$  orbitals are hence orthogonal to all the other occupied orbitals just because of their angular dependence. They do not need to spread away from the nucleus. Adding to the fact that the transition metal ions are separated by oxygen atoms leads to a small overlap of the  $3d$  states of neighbouring cobalt atoms. The consequence is that the  $3d$  states are intermediate between the localised and extended-wave limits. Also, because of their small effective radius, the on-site Coulomb repulsion is large in the  $3d$  shell. In terms of the Hubbard Hamiltonian, introduced in Eq. (1.15), this leads to a large interaction energy  $U$  and a small bandwidth  $W$ . Transition-metal oxides are thus typical compounds where to expect a Mott transition.

Historically, the proximity to a Mott metal-insulator transition was proposed to be exemplified on the  $d^1$  transition-metal series, reproduced in Fig. 1.3. The idea was that the ratio between the local interaction and the bandwidth,  $U/W$ , would increase along the series in Fig. 1.3, with the  $5d$  oxide  $\text{ReO}_3$  less correlated than the rest of the  $3d$  oxides (with vanadium- or titanium-based states closest to the Fermi level). Therefore, over this series, weight is transferred from the quasiparticle peak to the satellite region

### 1.3. Actual materials: complex transition metal oxides

(the Hubbard band), and one can observe this behaviour in Fig. 1.3<sup>1</sup>. From a modern perspective, however, one should note that further effects crucially enter into play in these particular compounds [37, 38].

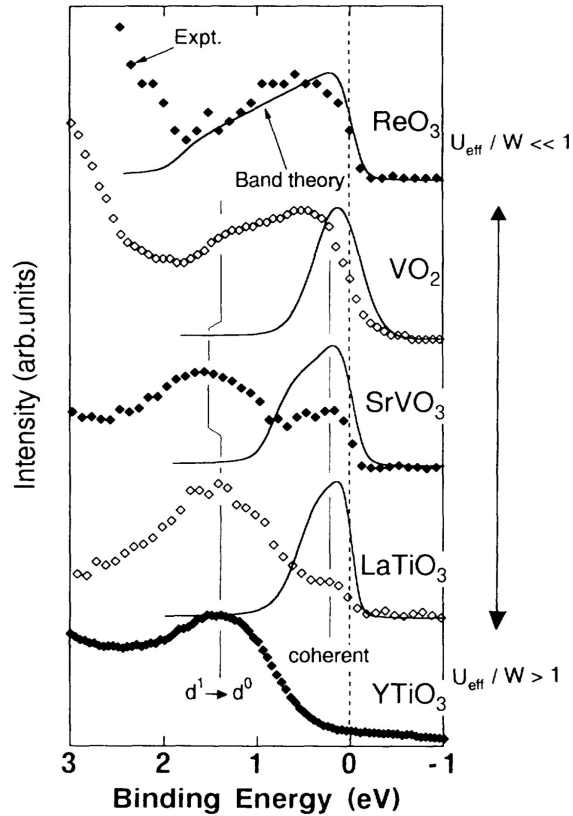


Figure 1.3: Photoemission spectra (diamond symbols) of several  $d^1$  transition metal oxides, taken from Ref. [28]. The solid lines are from Kohn-Sham DFT band structure calculations. The effect of correlations increases from  $\text{ReO}_3$  (a weakly-correlated metal) to  $\text{YTiO}_3$  (a Mott insulator). In between, spectral-weight transfers from the quasiparticle peak to the Hubbard satellite are typical of the Mott transition, as depicted in Fig. 1.2.

Indeed, it is nowadays clear that almost none of the oxides can simply be described by a Hubbard single-band model as in Eq. (1.15). Many more degrees of freedom are entering into play in the real materials. The  $d$  orbitals are 5-fold degenerate (10 when considering spins). Crystal-field effects, multi-orbital effects (on top of the presence of a local  $U$ , several additional Coulomb matrix elements need to be considered, such as an inter-orbital  $J$ ), coupling to oxygen states and structure distortions complicate the game.

In complex oxides, the transition metal ions are typically engaged in oxygen octahedra

<sup>1</sup>The photoemission experiment in Ref. [28] was performed using relatively low photon energies, such that it is surface-sensitive. Still, the trend observed in Fig. 1.3 from Ref. [28] is interesting.

or tetrahedra. The static electric field created by the oxygen atoms lifts the degeneracy between the 5-fold degenerate  $3d$  orbitals on the transition metal atoms. In  $3d$  orbitals, this crystal-field splitting is large. It leads to the splitting between twofold degenerate  $e_g$  orbitals and threefold degenerate  $t_{2g}$  orbitals. In an octahedral environment, as in the cobaltates, the  $t_{2g}$  do not point towards oxygen atoms. This minimises their electronic Coulomb repulsion and leads to the fact that they are lower in energy than the  $e_g$  orbitals, that point towards oxygen atoms. In a tetrahedral environment, the situation is opposite and the doublet is lower in energy than the triplet.

Because of small direct overlap and because they are separated by oxygen atoms, the hopping processes between two cobalt atoms often involve oxygen ligands. An important energy scale is the charge-transfer energy, which is the gap between the oxygen  $p$  states and the transition metal  $d$  states:  $\Delta = \epsilon_d - \epsilon_p$ . If  $\Delta$  is large compared to the overlap integral  $t_{pd}$ , the effective metal-to-metal hopping can be estimated as  $t_{\text{eff}} \sim t_{pd}^2/\Delta$ . In a  $d^1$  Mott-insulating compound, the ratio between the charge-transfer energy and the Hubbard  $U$  controls the nature of the low-energy bands, which lie closest to the Fermi level [39]. If  $\Delta > U$ , the low-lying band in a photoemission spectrum is the lower Hubbard band and has a predominant transition-metal character. The oxygen  $2p$  states are deeper in energy. If  $U > \Delta$ , the situation is opposite, and the low-lying band has a predominant oxygen character.

From this discussion, we can already see that the behaviour of these materials is controlled by qualitative as well as quantitative ingredients. Therefore, both simple models and *ab initio* calculations have an important role to play.

## 2 Introduction to sodium-doped cobaltates

In this chapter, we give a brief introduction to the physics of sodium cobaltates,  $\text{Na}_x\text{CoO}_2$ . We review previous experimental and theoretical findings.

### 2.1 Crystallography

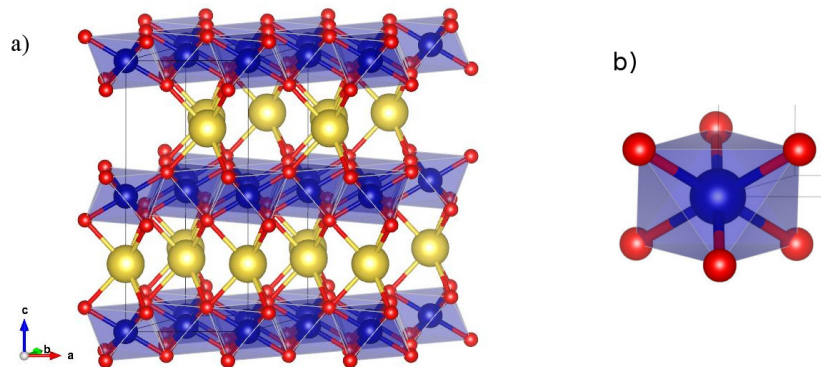


Figure 2.1: Crystalline structure of the sodium-doped cobaltates. a) The cobaltates are composed of  $\text{CoO}_2$  planes, between which sodium ions (large yellow spheres) are intercalated. Within the  $\text{CoO}_2$  planes, the cobalts (blue spheres) form a triangular lattice. The oxygen atoms (red spheres) alternate above and below cobalt triangles. The oxygen atoms are stacked in a way that successive  $\text{CoO}_2$  planes are not equivalent. We refer to this as an  $ab$ -type of stacking. b) Locally, each cobalt atom is encaged in a  $\text{CoO}_6$  octahedron. The oxygen octahedra are further compressed along the  $c$ -axis, leading to a local trigonal symmetry.

The sodium-doped cobaltates,  $\text{Na}_x\text{CoO}_2$ , are layered compounds, as depicted in Fig. 2.1. They are composed of  $\text{CoO}_2$  planes, in between which sodium atoms are intercalated. Within the  $\text{CoO}_2$  planes, the cobalt atoms form a two-dimensional triangular lattice. The

oxygen atoms alternate above and below the centres of the cobalt triangles. The oxygen atoms hence also form a triangular lattice. Locally, each cobalt atom is engaged into an oxygen octahedron, of unit formula  $\text{CoO}_6$ . These octahedra are further compressed along the  $c$  axis.

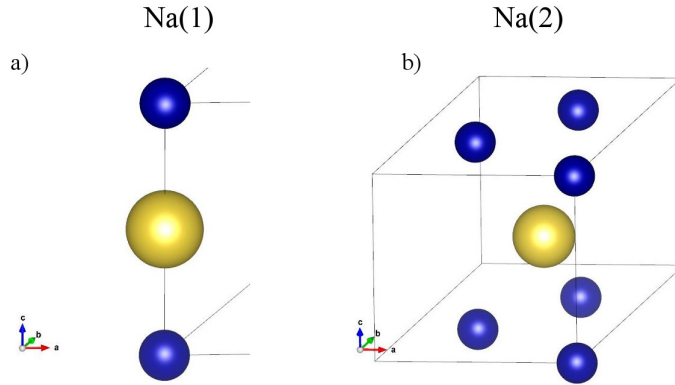


Figure 2.2: The two crystallographically inequivalent sodium positions. Large yellow spheres denote Na and blue spheres denote Co. a) The Na(1) site is above a cobalt atoms. b) The Na(2) site is above the center of a cobalt triangle (or, equivalently, above an oxygen atom). For simplicity, oxygen atoms are not displayed.

Sodium atoms are intercalated between the  $\text{CoO}_2$  sheets and act as spacers as well as electron donors. The sodium ions can occupy two inequivalent crystallographic sites, as depicted in Fig. 2.2, labeled Na(1) and Na(2) [40]. The Na(1) sites lie above a cobalt atom, while the Na(2) sites lie above the centre of a cobalt triangle.

While the in-plane lattice constant  $a = 2.8 \text{ \AA}$  (or, equivalently, the cobalt-cobalt distance within a plane) stays relatively constant in the whole experimentally accessible doping range, the interplanar distance, about  $5.5 \text{ \AA}$ , decreases with increasing sodium concentration [40]. This may be due to the electrostatic screening by the sodium ions. The large interplanar distance, compared to the in-plane lattice constant, has motivated a discussion of the cobaltates in terms of an effective two-dimensional system.

## 2.2 Local atomic states

We give a first description of the electronic structure of the cobaltates in terms of their constituting atomic configurations. The charge-neutral electronic configurations of the constituting atoms are:

- Co:  $Z = 27$ , configuration  $[\text{Ar}] 3d^7 4s^2$ ,
- O:  $Z = 8$ , configuration  $[\text{He}] 2s^2 2p^4$ ,

- Na:  $Z = 11$ , configuration  $[\text{Ne}] 3s^1$ .

In the solid, these atoms are combined and their electrons can migrate. The electrons rearrange such that the ions reach a more stable, closed-shell configuration. In this simplified view, the sodium atom wants to lose one  $3s$  electron and become  $\text{Na}^+$ . Hence, the role of sodium is to give away an electron to the  $\text{CoO}_2$  planes. The  $3s$  states, as well as the core levels of the sodium, can be considered to have energies far from the Fermi level.

The oxygen wants to fill its  $2p$  shell and become  $\text{O}^{2-}$ . As in most transition-metal oxides, the oxygen  $2p$  shell is full and lies below the Fermi level.

Once the sodium and oxygen ionic configurations are determined, a simple electron count shows that cobalt atoms have a configuration  $\text{Co}^{(4-x)+}$ :  $[\text{Ar}] 3d^{5+x}$ . The cobalt states have a fractional occupation. They lie at the Fermi level and form the valence band. In particular, for  $x = 0$ , the cobalt atoms have a formal valence of  $d^5$ , hence an odd number of electrons. A Mott insulator could be theoretically expected. However, compounds with low sodium content are difficult to synthesise and a Mott-insulating state at  $x = 0$  was never experimentally confirmed [41]. For  $x = 1$ , the cobalt atoms have a formal valence  $d^6$ , hence an even number of electrons, resulting in a completely filled level. This compound is a band insulator [42]. The particular case  $x = 2/3$  lies close to the band-insulating limit  $x = 1$ .

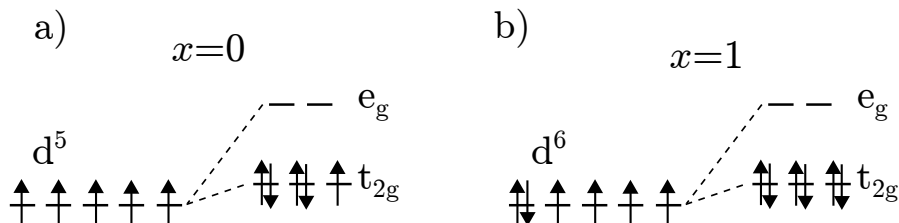


Figure 2.3: In an octahedral environment, atomic  $3d$  orbitals are split into  $t_{2g}$  (lower in energy) and  $e_g$  (higher in energy). In a trigonal environment, the  $t_{2g}$  manifold is further split into  $a_{1g}$  and  $e'_g$  (not represented here). a) For the sodium content  $x = 0$ , there are 5 electrons in the  $t_{2g}$  manifold. b) For the sodium content  $x = 1$ , there are 6 electrons in the  $t_{2g}$  manifold, yielding a band insulator.

In the solid, each cobalt atom is encaged in an oxygen octahedron. The octahedral crystal field induces a splitting within the initially 5-fold degenerate  $3d$  manifold, between the  $e_g$  manifold (twofold degenerate) and  $t_{2g}$  manifold (threefold degenerate), as represented in Fig. 2.3. The  $t_{2g}$  orbitals have a partial occupation, while the  $e_g$  orbitals have a higher energy and are empty. The  $t_{2g}$  orbitals have lobes pointing between the oxygen atoms, hence a low hybridisation of these states and oxygen is expected. The  $e_g$  have lobes pointing towards the oxygen atoms, hence a high hybridisation with oxygen is expected.

Moreover the oxygen octahedra are compressed along the  $c$  axis, reducing the symmetry of the local cobalt environment from octahedral to trigonal. This compression induces a further crystal-field splitting within the  $t_{2g}$  manifold, between a symmetric  $a_{1g}$  state and two degenerate states of symmetry  $e'_g$  (the latter not to be confused with the  $e_g$  orbitals).

### 2.3 Experimental phase diagram

The cobaltate family displays a very rich experimental phase diagram, as a function of sodium content  $x$  and temperature. This is due to the subtle interplay between structural, charge, orbital and magnetic degrees of freedom.

The structural degrees of freedom originate in the many possible arrangements for the sodium dopants. In principle, the sodium ions can create a more or less ordered structure, or even be mobile between the  $\text{CoO}_2$  planes. Several ordering patterns can appear upon varying  $x$ . Sodium ordering has been investigated experimentally. For  $x = 1/3$ , a sodium pattern appears where only the Na2 sites are occupied [43]. For  $x = 1/2$ , an equal occupation of Na1 and Na2 sites was observed [44]. For  $x = 2/3$ , a complex supercell emerges [10]. The ordering of sodium at  $x = 2/3$  will be further described later. For other sodium contents  $x$ , the situation is unclear.

The sodium arrangement in turn influences the local electrostatic background felt by the  $\text{CoO}_2$  planes. A modulating potential, created by the sodium ions, could in principle favour charge-disproportionation within the cobalt planes.

A modulation in the formal valence of the cobalt atoms (for example created by a charge-disproportionation) has consequences for magnetism, as evidenced in Fig. 2.3. Indeed, the  $\text{Co}^{3+}$  ion is non-magnetic (with a fully occupied  $t_{2g}$  manifold,  $S = 0$ ), while the  $\text{Co}^{4+}$  ion is magnetic (with one half-filled state,  $S = 1/2$ ).

Various successive experimental phase diagrams were presented. First, based on in-plane susceptibility and in-plane resistivity measurements, Foo *et al.* [45] presented the phase diagram displayed on Fig. 2.4. They distinguish a low-doping ( $x < 1/2$ ) and a high-doping ( $x > 1/2$ ) region, both metallic, separated by a charge-ordered insulator at  $x = 1/2$ .

The phase diagram by Foo *et al.* was revised by Lang *et al.* [46] via Nuclear Magnetic Resonance (NMR) measurements on both Na and Co. Sodium NMR directly probes the average cobalt planes spin susceptibilities via the Knight shift, or  $\chi_{\text{perp}}^{\text{spin}}(\mathbf{q} = 0, \omega = 0)$ . Cobalt NMR is probing the cobalt charge and spin states as  $\lim_{\omega \rightarrow 0} \sum_{\mathbf{q}} \frac{\text{Im} \chi_{\text{perp}}^{\text{spin}}(\mathbf{q}, \omega)}{\omega}$ , via the spin-lattice relaxation rate. NMR is thus a local probe. It gives access to the static spin susceptibility, either uniform or local.

The phase diagram of Lang *et al.* revisits the nature of the magnetic correlations. It highlights a characteristic doping,  $x^* \approx 0.6$ , around which the magnetic correlation

### 2.3. Experimental phase diagram

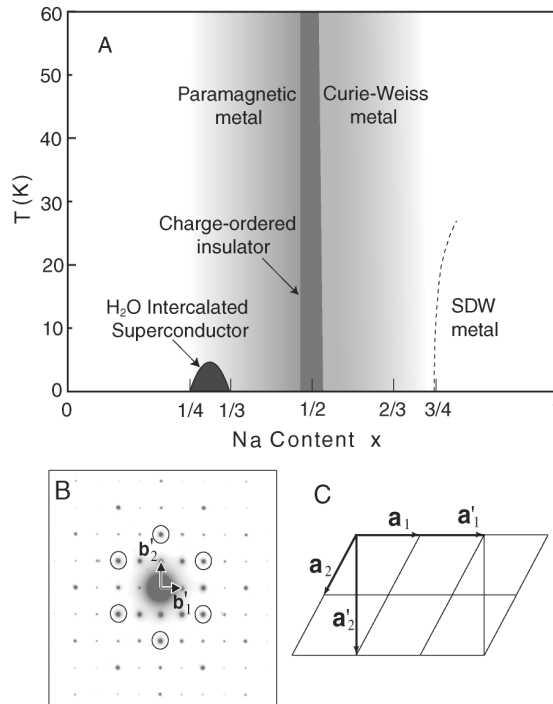


Figure 2.4: Phase diagram proposed by Foo *et al.* [45], based on in-plane susceptibility and resistivity measurements. The samples are metallic for all dopings, except for  $x = 1/2$ . The Curie-Weiss metal displays ferromagnetic in-plane correlations. b) Electron diffraction pattern and c) Na superstructure lattice for  $x = 1/2$ .  $\mathbf{a}_1$  and  $\mathbf{a}_2$  denote lattice vectors for the triangular lattice formed by the cobalt atoms.  $\mathbf{a}'_1$  and  $\mathbf{a}'_2$  denote the lattice vectors for the sodium superlattice. The Na1 and Na2 sites are found to be equally occupied for the  $x = 1/2$  composition and the sodium atoms form zig-zag stripes [44].

regime changes.

The latest phase diagram was proposed by Schulze *et al.* [47], based on specific heat measurements and muon spin resonance ( $\mu$ SR) experiments. The specific heat probes the density of states at the Fermi level, with a connection to the effective mass.  $\mu$ SR probes local spin fluctuations.

Putting these phase diagrams together allows to distinguish several phases, which we now describe separately.

**The low-doping phase ( $x < 1/2$ )** At low doping, the cobaltates are in a paramagnetic metallic state [45]. The susceptibilities are Pauli-like, although large in magnitude compared to conventional metals [45]. The charge distribution is homogeneous among the cobalt atoms [46]. This phase is often considered as less correlated, even if it is close to the commensurate  $x = 0$  limit (see also Fig. 2.3).

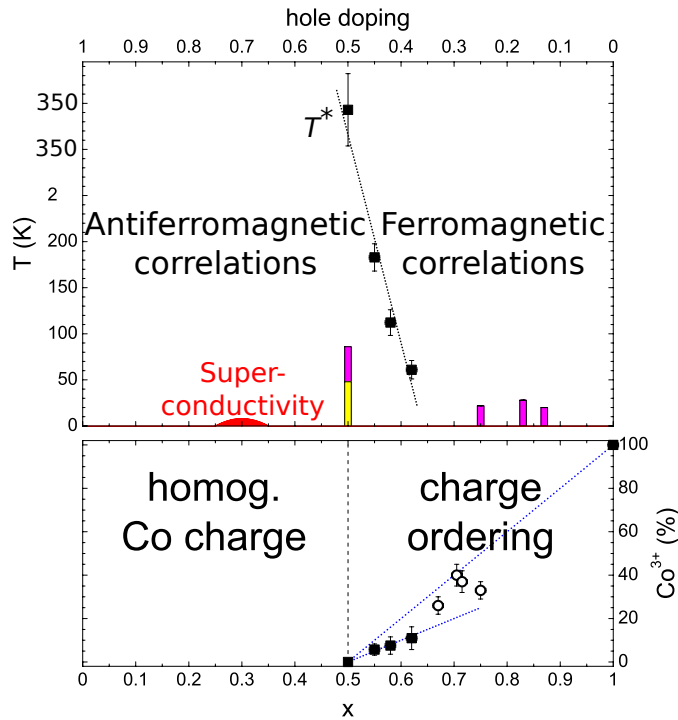


Figure 2.5: Phase diagram proposed by Lang *et al.* [46], based on sodium NMR and cobalt NMR. On the top panel, the crossover between two magnetic correlation regimes at  $x^*$  is indicated. The  $T^*$  line corresponds to a maximum in the average static spin susceptibility. The superconducting phase, as well as the known long-range-ordered phases, are indicated with their respective transition temperatures (yellow: insulator; magenta: magnetic LRO). On the bottom panel, local charge states of the cobalt atoms are indicated. For  $x > 1/2$ , a charge-disproportionation sets in, with the gradual appearance of  $\text{Co}^{3+}$  ions, the rest of the cobalt having mixed valence.

Remarkably, under hydration, the cobaltates become superconducting for  $1/4 \leq x \leq 1/3$  [3].

**Magnetic insulator at  $x = 1/2$**  At  $x = 1/2$ , the compound becomes insulating [45]. Electron diffraction detected an ordering of the sodium dopants, forming stripes, as shown in Fig. 2.4 [45]. There are two transition temperatures, observed in the susceptibility [45]: a magnetic transition occurs at  $T_N = 86$  K and a metal-insulator transition occurs at  $T_{MIT} = 51$  K. The local valence of the cobalts is unclear [48].

**Spin-fluctuating phase at  $1/2 < x < 3/4$**  The first phase of the high-doping regime is metallic. Spin correlations are present and they change regime around  $x^* \approx 0.6$  (antiferromagnetic below  $x^*$ , ferromagnetic above), as depicted in Fig. 2.5 [46]. For  $x \geq x^*$ , the correlations are of Curie-Weiss type and ferromagnetic in the plane. For  $x \leq x^*$ , the

### 2.3. Experimental phase diagram

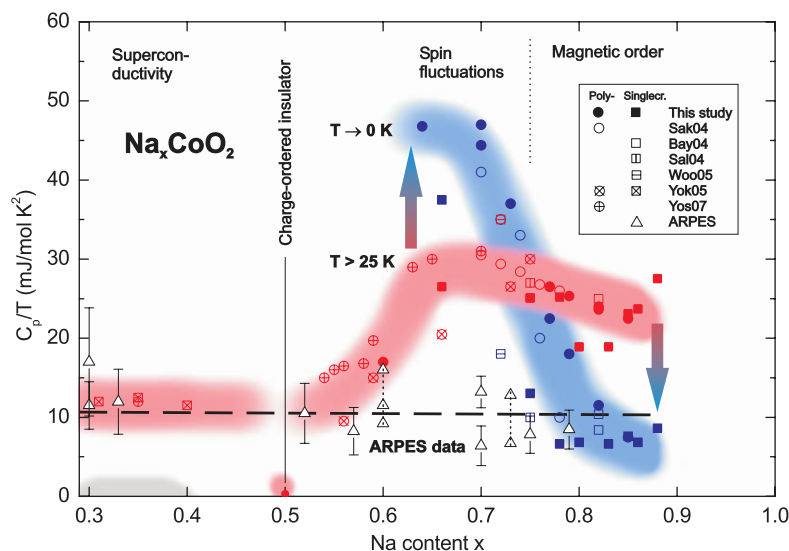


Figure 2.6: Phase diagram proposed by Schulze *et al.* [47], displaying specific heat. It contrasts a low-temperature specific heat (blue) and an intermediate-temperature specific heat (red). An ARPES specific heat, extracted from the measure of  $k_F$  and  $v_F$ , is also displayed.

correlations are believed to be antiferromagnetic (in the sense that they are maximum at a specific non-zero momentum). In the antiferromagnetic-correlation regime, the static uniform susceptibility  $\chi^{spin}(\omega = 0, \mathbf{q} = 0)$  goes through a maximum at  $T^*$  [46]. Also, the local charges on the cobalt atoms start to disproportionate, with the gradual appearance of  $\text{Co}^{3+}$  atoms [46]. The effective mass, as measured by the linear specific-heat coefficient, increases steeply from  $x = 0.6$ , as compared to the two-dimensional estimates from ARPES [47].

**Metal with magnetic long-range order for  $x \geq 3/4$**  Counterintuitively, the region closest to the band-insulating regime is the one where correlations play the major role. Magnetic long-range order develops. It is ferromagnetic in the plane and antiferromagnetic between the planes [47]. In a recent work, the ordering was proposed to be ferrimagnetic rather than ferromagnetic in the plane for the particular compound  $x = 0.82$  [49].

**The case  $x = 2/3$**  In this thesis, we are mainly interested in the  $x = 2/3$  compound. For this specific sodium content, nuclear magnetic resonance experiments by Alloul *et al.* have detected an ordering of the sodium ions, accompanied by a charge-disproportionation in the  $\text{CoO}_2$  planes [10]. The resulting supercell is displayed in Fig. 2.7. The sodium ordering hence involves both Na1 (above a cobalt atom) and Na2 (above a cobalt triangle) ions.

In the  $\text{CoO}_2$  planes, the cobalt atoms are found to segregate into Co1 and Co2 ions [10], as shown in Fig. 2.7. The Co2 ions have a partial occupation, with a formal valence of  $\text{Co}^{3.44+}$ . The Co1 ions are completely filled, with a formal valence  $\text{Co}^{3+}$ . These two kinds of ions form a lattice, following a kagomé superstructure [10]. In the kagomé structure, there are 4 atoms per supercell, 3 of which are equivalent (see Fig. 2.7).

The sodium order was later confirmed by X-ray diffraction experiments [50]. This experimental finding raises a question: Is the charge-disproportionation the cause or the consequence of the sodium-ordering? Or are these two effects intertwined?

### 2.4 Electronic structure of $\text{Na}_x\text{CoO}_2$

**Ab-initio band structures** The cobaltates have also triggered a large research effort on the theoretical side. Density-functional theory has been used to compute the band structure of the cobaltates. Singh *et al.* performed DFT with the local-density approximation (LDA) for the  $x = 1/2$  compound. In this calculation, sodium doping was simulated via the virtual-crystal approximation. The resulting band structure is depicted in Fig. 2.8. A metal is found, contrasting with low-temperature experiments at doping  $x = 1/2$  [45]. In Fig. 2.8, three well-separated sets of bands appear: the  $\text{O}(2p)$  manifold between -7 eV and -2 eV; the  $\text{Co}(t_{2g})$  between -1.5 eV and 0.2 eV; and the  $\text{Co}(e_g)$  between 1.5 eV and 3 eV. In LDA, the Fermi surface consists of a main  $\Gamma$ -centered hole pocket, and of 6 additional smaller pockets between  $\Gamma$  and  $K$ .

In Fig. 2.9, taken from Ref. [52], the LDA results are shown for various sodium contents. The band structure is zoomed in to display the  $t_{2g}$  manifold. The topology of the Fermi surface evolves with sodium content  $x$ . The main  $\Gamma$ -centered pocket is present in the whole doping range, with states with an  $a_{1g}$  character. At low doping, the 6 small hole pockets are present. They have an  $e'_g$  character. At high doping, the  $a_{1g}$  band crosses twice the Fermi level, creating an extra  $\Gamma$ -centered electron pocket. We will see later that the 6 small  $e'_g$  pockets, present at low to intermediate doping in DFT-LDA, have been the object of intense discussions.

In the experiments, the cobaltates display interesting magnetic correlations and magnetic instabilities, which have motivated spin-polarised calculations. Calculations within the local-spin-density approximations were performed [53, 54, 52] for various doping levels, all over the phase diagram. The resulting band structures are displayed in Fig. 2.9. Within spin-polarised calculations, the bands split into minority and majority-spin bands. Weak itinerant in-plane ferromagnetism is found for any doping. This is at odd with experiments, where ferromagnetism is found only in the high- $x$  part of the phase diagram. Also, the system is fully polarised, with completely filled majority bands. The  $e'_g$  electron pockets are still present at low and intermediate doping. The total area encaged by the Fermi surface is doubled compared to this of a non-spin-polarised calculation, due to an

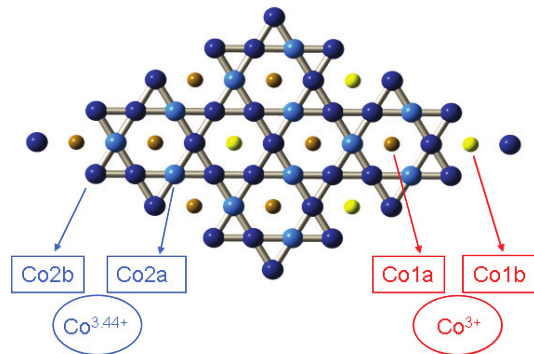
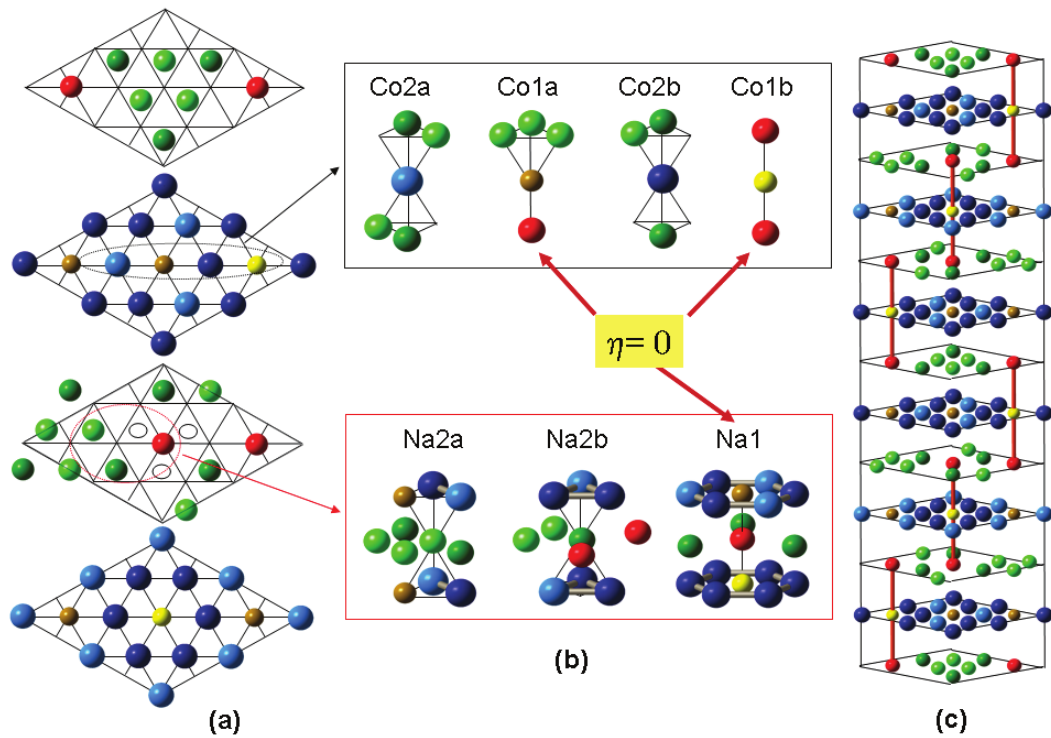


Figure 2.7: Sodium-ordering and charge-disproportionation, reproduced from Alloul *et al.* [10]. On the top panel, the three-dimensional structure of  $\text{Na}_{2/3}\text{CoO}_2$  is shown. This superstructure results from the ordering of the Na ions. The two-dimensional charge distribution on the cobalt atoms is shown on the bottom panel. Forgetting the crystallographic differences between the various atomic sites, the cobalt atoms form a two-dimensional kagomé superstructure. The  $\text{Co}^{3+}$  atoms are completely full, or blocked, while the  $\text{Co}^{3.44+}$  atoms have a fractional occupation.

effective doubling of charge carriers (for up and down spins). We will come back to the question of magnetism and spin-polarised calculations in Chap. 8.

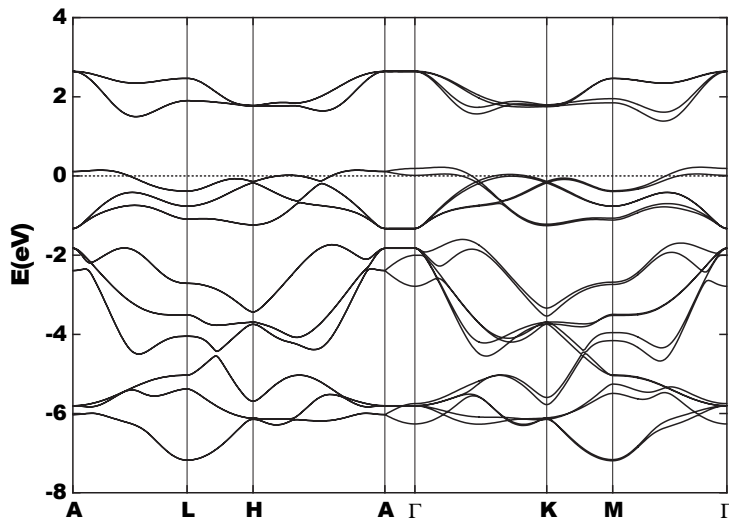


Figure 2.8: The LDA band structure for  $\text{Na}_{1/2}\text{CoO}_2$ , obtained by Singh *et al.* [51]. The band structure is zoomed on the low-energy sector.

As a first treatment to include the effect of strong correlations, LSDA+ $U$  calculations were performed, with  $U = 4$  eV [52]. The corresponding band structures and Fermi surfaces are displayed in Fig. 2.9. As in LSDA, a fully polarised itinerant ferromagnetic solution is found. We note that for the composition  $x = 1/2$ , the experimentally-observed insulator is not retrieved within LSDA+ $U$ . Upon adding the explicit local interaction parameter  $U$ , the 6 hole pockets disappear for all doping levels, and the Fermi surface loses part of its hexagonal distortion. The area of the Fermi sea corresponds again to the fact that the calculation is spin-polarised.

**Experimental band structure: ARPES** Various photoemission experiments were performed on the cobaltates, spanning over a large doping range.

The first photoemission spectrum was performed on the  $x = 0.7$  compound by Hasan *et al.* [55], and is reproduced in Fig. 2.10. It features various peaks as a function of the photon energy. The  $t_{2g}$  manifold is clearly distinguishable at low energies and gives rise to the first peak, around 0.7 eV. The  $t_{2g}$  peak is well-separated from the one originating in oxygen  $2p$  bands, between 2 eV and 6 eV. A high-energy feature, at 11 eV, was interpreted as a correlation satellite. From a comparison to a cluster model, this correlation satellite was interpreted to originate from an on-site  $U \approx 5$  eV. Because of this large value for the local Coulomb interaction  $U$ , compared to the weak  $t_{2g}$  dispersion found in LDA, the cobaltates were tagged as a strongly-correlated material.

ARPES experiments have also probed the details of the low-energy band structure and the Fermi surface of the cobaltates, for various sodium concentrations. The Fermi surface

## 2.4. Electronic structure of $\text{Na}_x\text{CoO}_2$

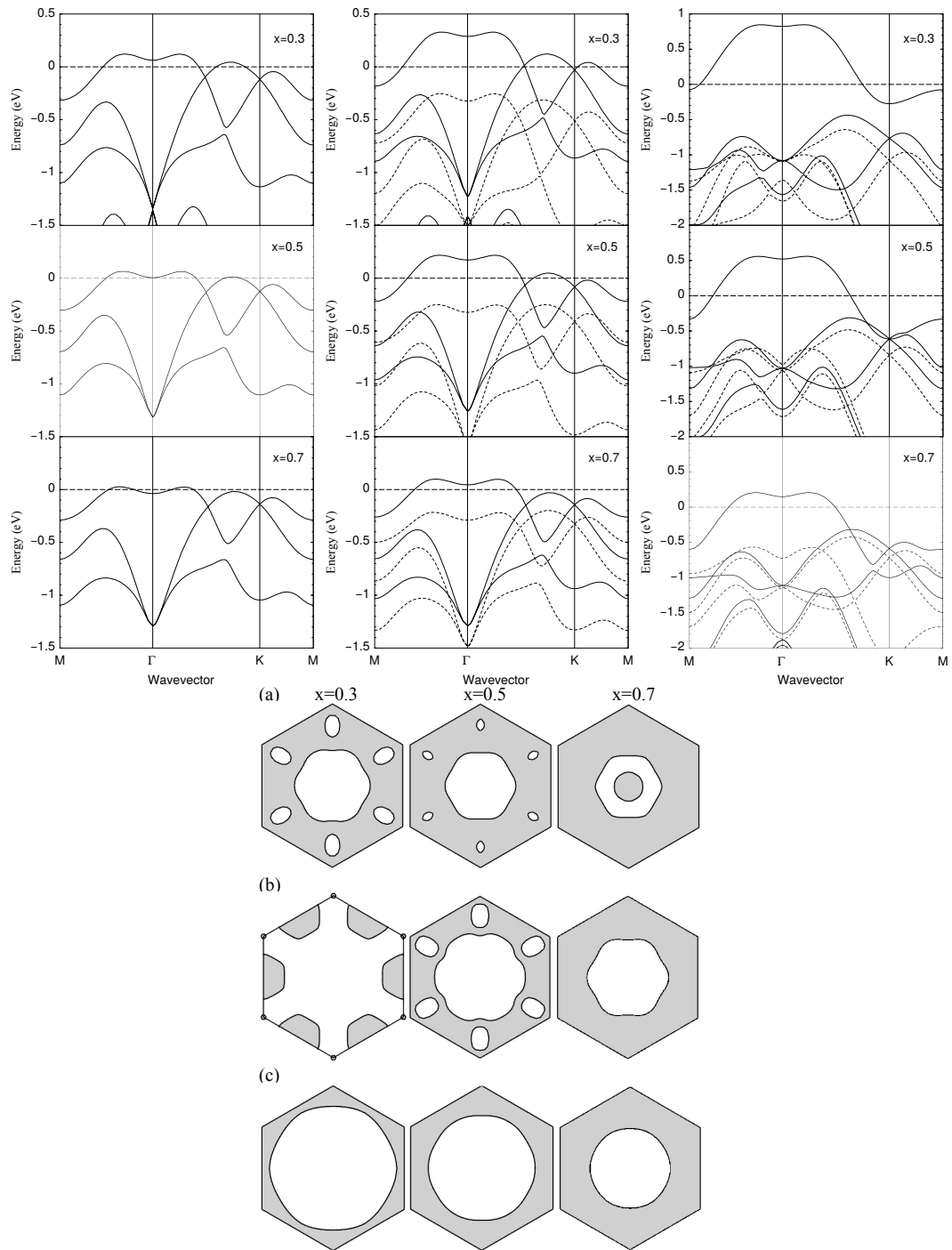


Figure 2.9: Top, from left to right: LDA, LSDA and LSDA +  $U$ , for various dopings. Bottom: The corresponding Fermi surfaces, from top to bottom. From [52]. For the spin-polarised calculations, the band for the majority spin is represented with a dashed line, and the minority spin with a full line. For LSDA+ $U$ , and value  $U = 4$  eV was used.

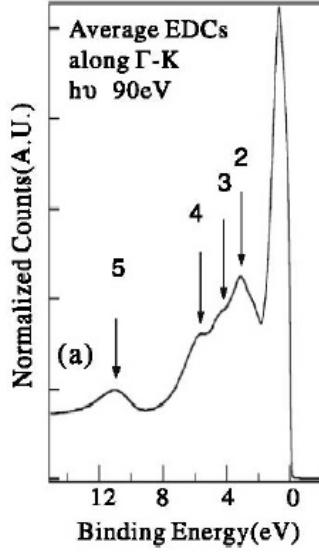


Figure 2.10: Photoemission spectrum of the  $x = 0.7$  compound. The first peak, around 0.7 eV, originates from the  $\text{Co}(t_{2g})$  manifold. The peaks labelled 2, 3, 4 originate from  $\text{O}(2p)$  states. Peak 5 is interpreted as a correlation satellite, originating from a Hubbard  $U \approx 5$  eV. From [55].

for the sodium concentrations  $x = 0.3, 0.48$  and  $0.72$  is represented in Fig. 2.11, from experiments performed by Yang *et al.* [56]. For these dopings, ARPES finds that the Fermi surface consists of a single hole pocket, centered around the  $\Gamma$  point. Due to the crystal structure, the Fermi surface is non-isotropic, with a weak hexagonal distortion. This Fermi surface topology has been later found to hold in ARPES for all experimentally-accessible sodium concentrations:  $x = 0.7$  [55],  $x = 0.73$  [57],  $x = 0.33, 0.57, 0.8$  [58],  $x = 0.35, 0.48, 0.75$  [59],  $x = 0.6$  [60],  $x = 0.30, 0.48, 0.60, 0.72$  [56]. This fact contrasts with theoretical band structures from LDA, which always detect 6 extra  $e'_g$  hole pockets for sodium concentrations  $x \leq 0.67$ , as depicted in Fig. 2.9.

Moreover, in ARPES, this absence of the  $e'_g$  hole pockets is consistent with the Luttinger theorem [56]. The Luttinger theorem states that the volume enclosed by a Fermi surface is directly proportional to the particle density. Small apparent deviations from the Luttinger theorem can actually be accounted for by considering the  $k_z$ -dispersion of the bands. Indeed, the Fermi surface is often represented by its  $k_z = 0$  two-dimensional cut. However, the actual compound is three-dimensional, and the area enclosed by the Fermi surface varies with  $k_z$ .

As a further indication that strong correlations are at play in the cobaltates, ARPES sees a strong renormalisation of the bandwidth and of the Fermi velocity as compared to LDA [55, 60, 56, 58]. In Fig. 2.12, the low-energy dispersion of the  $a_{1g}$ -derived band is shown. From the single-particle removal spectra, the bandwidth seems to be less than

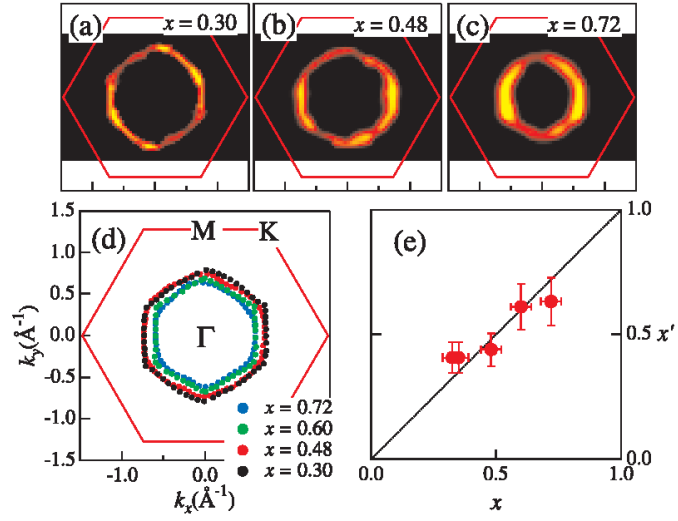


Figure 2.11: Experimental Fermi surface for various doping levels, represented in the first Brillouin zone of the triangular lattice. The Fermi surface area grows with doping, as expected from the Luttinger theorem. On (e) an effective Na concentration extracted from the experimental Fermi surface areas, is plotted against the chemical Na concentration. From [56].

200 meV. This contrasts with LDA calculations where the bandwidth in the  $t_{2g}$  manifold is around 1.2 eV (see Fig. 2.9).

The dispersion of the  $e'_g$  bands, responsible for the hole pockets in DFT, could be monitored in ARPES [56, 59]. The full  $t_{2g}$  dispersion is shown in Fig. 2.13. There, only one band, with  $a_{1g}$  character, crosses the Fermi level. The  $e'_g$  bands are visible and are found below the Fermi level in the whole doping range. This motivated the term “sinking pockets”.

So far, the discussion of the ARPES results has been done considering that the dispersion is effectively two-dimensional, with a weak interplanar coupling. Most quantities have been presented in the  $(k_x, k_y)$  plane and averaged or sliced in the  $k_z$  direction. More recent ARPES experiments, by Arakane *et al.* [61, 62], focus on the whole three-dimensional low-energy dispersion. Their results are reproduced in Fig. 2.14. A sizable dispersion along  $k_z$  is detected in the high-doping region, allowing to revisit the experimental Fermi surface. In particular, the  $a_{1g}$  band appears to cross the Fermi surface close to the  $\Gamma$  point, such that the latter is occupied at high doping. In any case the band dispersion in the vicinity of the  $\Gamma$  point is flat. This has important consequences in terms of Fermi surface nesting. This result was interpreted to be in line with specific-heat measurements, where a high effective mass was measured for large sodium concentrations [47].

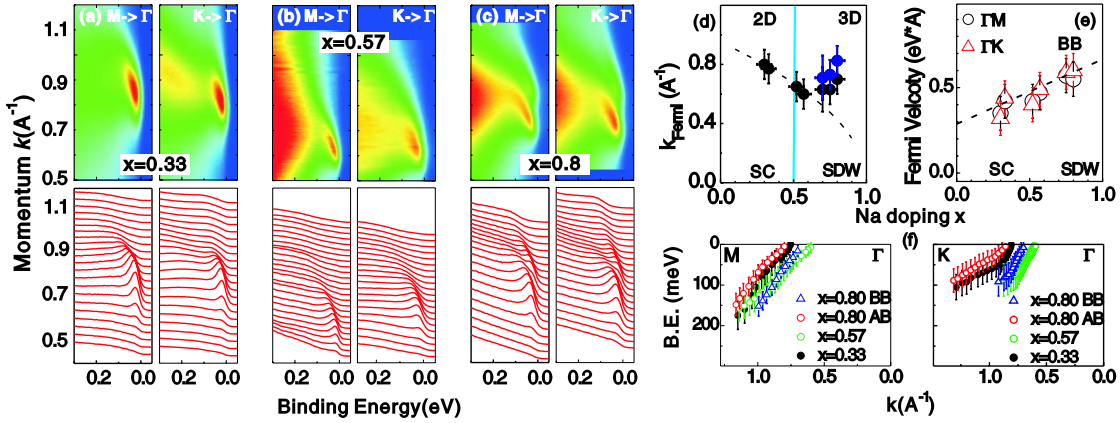


Figure 2.12: The low-lying states from ARPES measurements by Qian *et al.* [58]. On the left panel (a, b, c), the low-energy dispersion of the valence band is depicted, for various doping levels, along the  $\Gamma M$  and the  $\Gamma K$  lines. At low and intermediate doping ( $x = 0.33$  and  $0.57$ ), there is only one band crossing the Fermi surface. At high-doping ( $x = 0.8$ ), two bands appear to cross the Fermi surface. This is the result of a more marked dispersion along  $k_z$  at high doping and indicates a two-dimensional (at low and intermediate doping) to three-dimensional (at high doping) crossover. At high-doping, the two bands are resolved in a bonding (BB) and an anti-bonding (AB) band. The evolution of the Fermi surface size, as measured from an average Fermi momentum  $k_F$  and as a function of doping, is shown in (d). The averaged Fermi velocity as a function of doping is shown in (e). Finally, the dispersion plots along the  $M\Gamma$  and  $K\Gamma$  lines is shown in (f).

**Effect of strong correlations** Many studies have attempted to put correlations at the centre of the description of the cobaltates. They mostly address the discrepancy between the DFT and the ARPES Fermi surfaces. They also compute additional physical observables that were previously measured experimentally.

The discovery of exotic phenomena in the high-doping region of the phase diagram (near the band-insulating limit), such as thermoelectricity, was a puzzle. This motivated Motrunich and Lee [63] to introduce nearest-neighbour Coulomb repulsions between cobalt ions. These non-local interactions would explain why a compound close to the band-insulating limit could appear strongly correlated. They also discuss additional properties and predict a possible charge-disproportionation.

The discrepancy between LDA and ARPES Fermi surfaces, led to a vast literature. Calculations based on a LDA-derived tight-binding model with the Gutzwiller approximation (amounting to  $U = \infty$ ) were performed by Zhou *et al.* [64]. They found a sinking of the  $e'_g$  pockets at various dopings, including in the low-sodium content sector. A LDA + DMFT calculation with  $J \neq 0$  by Ishida *et al.* [65] found the opposite trend: when reinstalling explicit finite  $U$  local interactions, the  $e'_g$  pockets are actually stabilised.

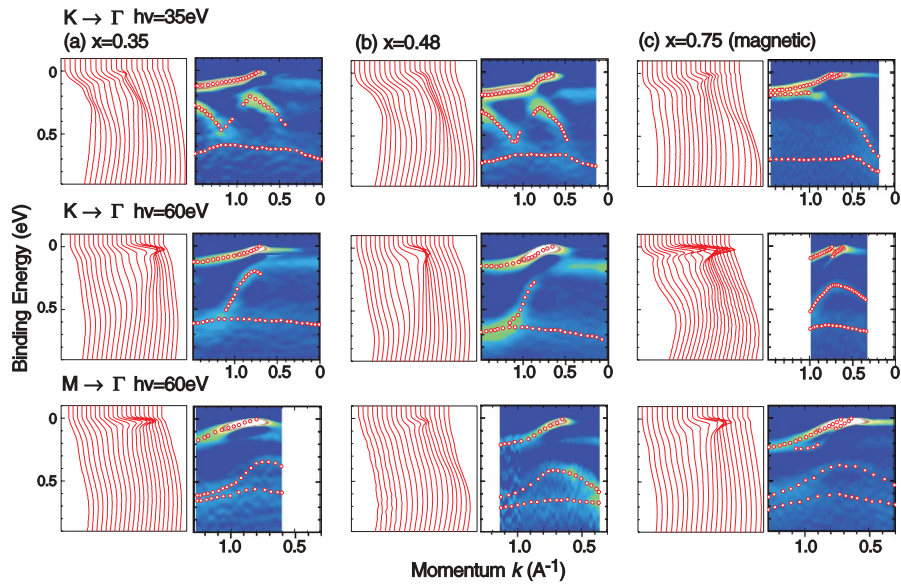


Figure 2.13: ARPES spectra showing the full  $t_{2g}$  dispersion, for various doping levels, along the  $\Gamma M$  and the  $\Gamma K$  lines, from Qian *et al.* [59]. In particular, only one band appears to cross the Fermi level, supposedly with  $a_{1g}$  character. The  $e'_g$  bands, that form 6 hole pockets in LDA, are visible *under* the Fermi level.

Marianetti *et al.* discussed the role of orbitals such as the cobalt  $e_g$  and the oxygen  $2p$  [66]. They found that these seemingly high-energy orbitals played an important role in terms of dressing the  $t_{2g}$  particles. Substantial charge-redistribution effects could be observed between these orbitals upon doping. The effect of the details of the low-energy Hamiltonian on the correlations was later studied, with an emphasis on the sodium arrangement [67] and on the intra- $t_{2g}$  crystal-field splitting [68]. It was found that, taking the crystal-field splitting as an adjustable parameter, and including local interactions  $U$ , the topology of the Fermi surface could be varied, and the  $e'_g$  pockets could fall below the Fermi level [68].

Later on, Liebsch and Ishida [69] carried a systematic study of the material, allowing for values for  $U$  and the crystal-field splitting that they considered most realistic. The result was that for the probed range of parameters, the  $e'_g$  pockets were always present.

In the meanwhile, several low-energy multiorbital tight-binding models were derived, and possible instabilities were investigated [70, 71, 72].

As an alternative starting point to a model study, quantum chemistry methods were applied to determine the parameters of the low-energy Hamiltonian. This approach was considered as a way to avoid to deal with the problem of the extra pockets of DFT. Landron and Lepetit studied small clusters of cobalt and oxygen (consisting of one and two octahedra) [73, 74]. They derived values for the interaction parameters and the

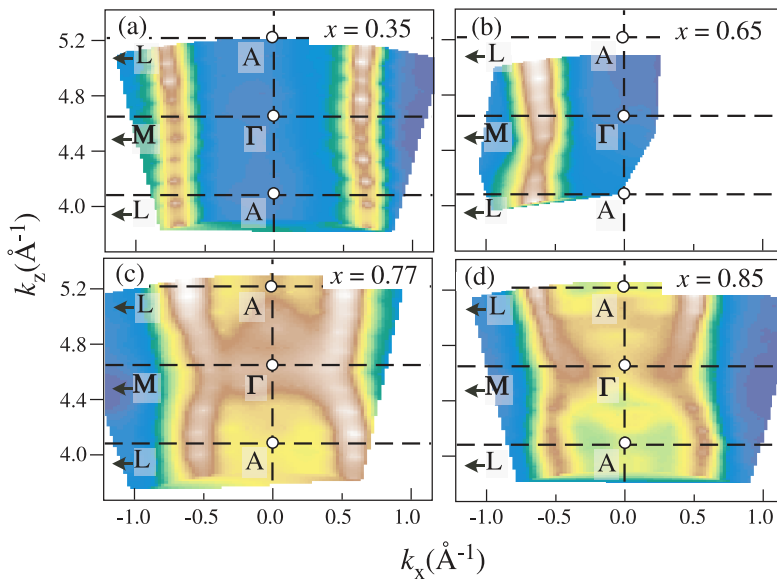


Figure 2.14: ARPES intensity at the Fermi level, as a function of  $k_z$  and  $k_x$ , for various doping levels, from Arakane *et al.* [62]. At low doping ( $x = 0.35$  and  $0.65$ ), the dispersion along  $k_z$  merely induces a weak modulation in the Fermi surface along  $k_z$ . At high doping (here, starting from  $x = 0.77$ ), there is a significant dispersion along the  $k_z$ -axis. In particular, it leads to a change in the topology of the Fermi surface, since the  $\Gamma$ -point is occupied at high doping.

$a_{1g}$ - $e'_g$  crystal-field splitting. These parameters were later used on a lattice Hamiltonian by Bourgeois *et al.* Their results, using dynamical mean-field theory, are in qualitative agreement with photoemission spectra and experimental Fermi surfaces [75, 76].

Peil *et al.* focused on the specific case  $x = 2/3$  and studied the effect of charge-ordering. They computed ARPES spectra and transport properties assuming a charge-ordering pattern on the cobalt sites, from cluster DMFT. The results were found in good agreement with experiments [77]. Magnetic correlations and magnetic instabilities have also been explored. Using a rotationally-invariant slave boson method on a three-site cluster, Lechermann was able to capture the transition from antiferromagnetic to ferromagnetic correlations around  $x = 2/3$  [78]. Whereas the ferromagnetic correlations originate in the itinerant character of the charge carriers, antiferromagnetic correlations can be assigned to short-range super-exchange processes. Momentum-dependent charge and spin susceptibilities have been computed, with the inclusion of vertex corrections by Boehnke *et al.* [79] The doping-dependence of these susceptibilities shows that various ordering patterns could be favoured. These last results were wrapped up in [80]. In this work, spectral functions obtained from multiorbital charge-self-consistent DFT + DMFT show  $e'_g$  pockets sinking below the Fermi level. Finally, a spin-polaron branch was predicted using dual fermions [81]: this branch corresponds to a spin coupled to a ferromagnetic background.

# 3 Theoretical methods for electronic structure

In the previous two chapters, we have given a qualitative description of the phenomenology of correlated metals and more specifically of the cobaltates. In this chapter, we describe quantitative, numerical approaches to treat correlated electronic systems. We give a broad overview on some methods for the many-body problem. These methods are designed to treat electronic exchange and correlation, each at its particular level of refinement.

In first quantisation and keeping the positions of the atoms fixed, the electronic many-body Hamiltonian reads<sup>1</sup>:

$$\mathcal{H} = \sum_{i=1}^N \frac{p_i^2}{2m_e} + \sum_{i=1}^N v(\mathbf{r}_i) + \frac{1}{2} \frac{1}{4\pi\epsilon_0} \sum_{i=1}^N \sum_{j \neq i}^N \frac{e^2}{|\mathbf{r}_i - \mathbf{r}_j|}, \quad (3.1)$$

where

$$T = \sum_{i=1}^N \frac{\mathbf{p}_i^2}{2m_e} \quad (3.2)$$

is the kinetic energy of the electrons;

$$V = \sum_{i=1}^N v(\mathbf{r}_i) \quad (3.3)$$

is the external-potential energy, typically due to electron-nucleus attraction;

$$V_{ee} = \frac{1}{2} \frac{1}{4\pi\epsilon_0} \sum_{i=1}^N \sum_{j \neq i}^N \frac{e^2}{|\mathbf{r}_i - \mathbf{r}_j|} \quad (3.4)$$

is the electron-electron Coulomb repulsion. The first two terms of Eq. (3.1) are one-body terms. The last term of Eq. (3.1), however, is an interacting term. Without it, the

---

<sup>1</sup>Here for clarity we have displayed the units. In the rest of this thesis, we will use atomic units, where  $\hbar = m_e = e^2 = 4\pi\epsilon_0 = 1$ .

many-body wave-functions would simply be Slater determinants. The presence of this interacting term leads to complicated correlation effects, beyond the one-electron picture.

The many-body wave-function is a linear combination of Slater determinants. It is a complex object of  $3N$  arguments:  $\Psi(\mathbf{x}_1, \dots, \mathbf{x}_N)$ , where  $\mathbf{x}$  refers to  $(\mathbf{r}, \sigma)$ . In principle, the many-body wave function gives access to all the observables of the system. However, this object is too big to be stored and is not tractable. Some more compact quantities give a useful and aggregated view on the physical system.

In this chapter we first present some useful aggregated quantities for the many-body problem. Then we present the general framework of auxiliary systems. We finish by describing in more detail two effective theories which will be used later in this thesis: the Density-Functional Theory (DFT) and the Extended Dynamical Mean-Field Theory (EDMFT).

### 3.1 Introduction to some physical observables

The many-body wave-function is a complex object. In order to extract useful and tractable information about the system, one is often led to consider contracted quantities, that contain aggregate information. These quantities can be directly connected to physical observables, as measured in experiments. In this section we describe three of these quantities, to which we will refer intensively in the remaining chapters: the electronic density, the one-body Green's function and the charge susceptibility.

In this thesis we will use both model-based and *ab initio* approaches. Hence, we will be dealing with different kinds of systems that use different conventions. We introduce our physical quantities in the framework of these two different systems.

#### 3.1.1 *Ab initio* approaches

*Ab initio* approaches deal with systems in a continuum, subject to an external potential (in our case, this potential will also be periodic). Also, our *ab initio* calculations will be performed at zero-temperature. The electronic density at point  $\mathbf{r}$  and spin  $\sigma$  is defined as:

$$n_\sigma(\mathbf{r}) = \langle \Psi_0 | \hat{c}_\sigma^\dagger(\mathbf{r}, t) \hat{c}_\sigma(\mathbf{r}, t) | \Psi_0 \rangle, \quad (3.5)$$

where  $\Psi_0$  is the many-body ground state and  $\hat{c}_\sigma^\dagger(\mathbf{r}, t), \hat{c}_\sigma(\mathbf{r}, t)$  are second-quantised creation and annihilation operators in the Heisenberg representation, respectively. Since the system is not subject to an external time-dependent potential, the density does not depend on the time variable,  $t$ .

### 3.1. Introduction to some physical observables

The propagation of a quasiparticle (quasielectron or quasihole) is described by the one-body Green's function. The zero-temperature, time-ordered one-body Green's function is defined as

$$G(\mathbf{x}_1, t_1; \mathbf{x}_2, t_2) = -i \langle \Psi_0 | \mathcal{T} \hat{c}(\mathbf{x}_1, t_1) \hat{c}^\dagger(\mathbf{x}_2, t_2) | \Psi_0 \rangle, \quad (3.6)$$

where  $\mathbf{x} = (\mathbf{r}, \sigma)$  combines the position and spin,  $\mathcal{T}$  is the fermionic time-ordering operator:

$$\mathcal{T} \hat{c}(\mathbf{x}_1, t_1) \hat{c}^\dagger(\mathbf{x}_2, t_2) = \theta(t_1 - t_2) \hat{c}(\mathbf{x}_1, t_1) \hat{c}^\dagger(\mathbf{x}_2, t_2) - \theta(t_2 - t_1) \hat{c}^\dagger(\mathbf{x}_2, t_2) \hat{c}(\mathbf{x}_1, t_1), \quad (3.7)$$

and  $\theta$  is the Heaviside function. Since our systems will be invariant with respect to a time translation, the Green's function will depend only on the difference  $t_1 - t_2$ . The one-body Green's function is very useful because it gives a direct access to any expectation value of a one-body operator and to the total energy.

The charge susceptibility is given, according to the Kubo formula for the linear response regime, by the charge-charge correlator:

$$\chi(\mathbf{r}_1, t_1; \mathbf{r}_2, t_2) = +i\theta(t_1 - t_2) \langle \Psi_0 | [\hat{n}(\mathbf{r}_1, t_1), \hat{n}(\mathbf{r}_2, t_2)] | \Psi_0 \rangle. \quad (3.8)$$

Here,  $n(\mathbf{r}_1, t_1) = n_\uparrow(\mathbf{r}_1, t_1) + n_\downarrow(\mathbf{r}_1, t_1)$  is the total electronic density. The notation  $[, ]$  refers to a commutator. Note the sign in front of the definition of the susceptibility. The sign convention here is different from what is often considered in the *ab initio* literature, but the same as the sign convention in the usual DMFT literature.

#### 3.1.2 Lattice model approaches

Methods for strong correlations typically deal with lattice models at finite temperature in the grand-canonical ensemble. The electronic density at site  $i$  and spin  $\sigma$  is expressed via a thermal average:

$$n_{i\sigma} = \langle c_{i\sigma}^\dagger c_{i\sigma} \rangle = \frac{\text{Tr} \left[ e^{-\beta H'} c_{i\sigma}^\dagger c_{i\sigma} \right]}{\text{Tr} e^{-\beta H'}}, \quad (3.9)$$

where  $c_{i\sigma}^\dagger, c_{i\sigma}$  denote creation and annihilation operators at site  $i$  and spin  $\sigma$ , respectively,  $\text{Tr}$  is the trace operator,  $\beta$  is the inverse temperature and  $H' = H - \mu$  is the many-body Hamiltonian shifted by the chemical potential. In the following, we will use the grand-canonical partition function:  $\text{Tr} e^{-\beta H'} = Z$ .

The time-ordered one-body Green's function is also expressed as a thermal average:

$$G_{ij}(\tau) = - \langle \mathcal{T}_\tau c_i(\tau) c_j^\dagger(0) \rangle = - \frac{\text{Tr} \left[ e^{-\beta H'} \mathcal{T}_\tau c_i(\tau) c_j^\dagger(0) \right]}{Z}, \quad (3.10)$$

where  $\tau$  is the imaginary-time variable,  $\mathcal{T}_\tau$  is the time-ordering operator in imaginary-time and  $c_i(\tau), c_j^\dagger(0)$  are Heisenberg operators in imaginary-time. As a specific case, we will later be using the local part of the Green's function, defined as  $G_{\text{loc}}(\tau) = G_{ii}(\tau)$ , which will play a central part in DMFT-based approaches.

Finally, the charge susceptibility is defined in imaginary time as

$$\chi_{ij}(\tau) = \langle \mathcal{T}_\tau n_i(\tau) n_j(0) \rangle - \langle n_i \rangle^2, \quad (3.11)$$

where  $\langle n_i \rangle$  is the average electronic density on site  $i$ . In our study, the density will always be considered as homogeneous and denoted  $\langle n \rangle$ . Within our sign convention, the charge susceptibility is positive in imaginary-frequency.

## 3.2 Auxiliary systems

In this section, we give an overview on mean-field theories through the perspective of auxiliary systems. A reference treating auxiliary systems from the construction of functionals is part 3 of [13]. A general strategy to deal with the full many-body problem, Eq. (3.1), is not to try to directly compute the full many-body wave function,  $\Psi$ . An efficient approach is to leave the many-body wave-function altogether and to focus only on a given physical quantity of choice. The aim is to design a theories that compute only these aggregated quantities. These quantities are sufficient to describe the observables we are interested in.

The strategy is then to represent these quantities, or observables, on an easier and tractable system. In this auxiliary system, the chosen observable takes the same values as in the original, physical system. Other quantities, instead, will take different values from the real system. The construction of various effective theories of interest is summarised in the table and follows from the following steps:

	Kohn-Sham DFT	DMFT	EDMFT
Physical observable	$n(\mathbf{r})$	$G_{\text{loc}}(\omega)$	$G_{\text{loc}}(\omega), W_{\text{loc}}(\omega)$
Effective potential	$v_{\text{eff}}(\mathbf{r})$	$\mathcal{G}_0^{-1}(\omega)$	$\mathcal{G}_0^{-1}(\omega), \mathcal{U}^{-1}(\omega)$
Auxiliary system	Kohn-Sham electrons	Anderson impurity model (AIM)	AIM with dynamical interactions

**1) The physical observable** What physical observable should be reproduced by the theory? In Density-Functional Theory (DFT) [6, 7], the physical observable is the electronic density,  $n(\mathbf{r})$ . In Dynamical Mean-Field Theory (DMFT) [9], the physical observable is the local, thermal one-body Green's function,  $G_{\text{loc}}(\omega)$ . In extended DMFT

(EDMFT) [82, 83, 84, 85, 86], one wants to reproduce both the thermal one-body local Green's function and the local screened Coulomb interaction,  $W_{\text{loc}}(\omega)$ .

**2) The effective potential** Once the observable is chosen, the next question to answer is: What is the effective, conjugate potential to this observable? The effective potential should be adjusted in such a way, as to represent the observable. For the case of DFT, the conjugate potential is a local effective potential  $v_{\text{eff}}(\mathbf{r})$ . For DMFT, it is the non-interacting impurity Green's function, or dynamical mean-field  $\mathcal{G}_0(\omega)$ . For EDMFT, there are two dynamical mean-fields: the impurity non-interacting Green's function and a dynamical Coulomb interaction  $\mathcal{U}(\omega)$ . In each case, the physical observable and the conjugate potential have the same level of complexity. For a static, space-dependent observable, the potential to be adjusted is static and space-dependent. For a local, dynamical variable, the conjugate potential is local and dynamical.

**3) The auxiliary system** The auxiliary system, on which the full, physical system is to be represented, is a system that one can solve, or at least for which the observable should be accessible. In DFT within the Kohn-Sham scheme (KS-DFT), the auxiliary system is a system of non-interacting electrons. The Kohn-Sham system is numerically solvable through a one-body Schrödinger equation. The connection between the physical system and the Kohn-Sham system is that the density,  $n(\mathbf{r})$ , should be the same in the two systems. In DMFT, the auxiliary system is an Anderson impurity model. The Anderson impurity model is characterised by its dynamical mean-field  $\mathcal{G}_0^{-1}(\omega)$  and a Coulomb interaction  $U$ . While in KS-DFT, the auxiliary system is non-interacting, in DMFT the Anderson impurity model (AIM) retains the interaction. The AIM is easier to solve than the full problem in the sense that it is local, or, equivalently, single-site (although there exist cluster extensions to DMFT [87, 88]). It requires the use of an impurity solver. In EDMFT, the auxiliary system is an AIM with dynamical interactions. The auxiliary system is again interacting, but with frequency-dependent interactions.

In principle, schemes relying on an auxiliary system raise questions. Is there a one-to-one correspondence between the physical observable and the effective potential of the auxiliary system? Is there always an effective potential that can reproduce the physical observable? Is it unique?

Moreover, all these methods require a way to determine the effective potential. This potential depends on the system of interest and computing it involves a self-consistency loop. In order to close this loop, an approximation is needed. Details on the approximations for each method are provided in the next two sections.

### 3.3 Ground-state properties: Density functional theory (DFT)

Density-functional theory is widely used in many fields of science. A lot of pedagogical textbooks and review articles have been written on the topic, see for example [89]. DFT was originally designed for electrons in a continuum. It aims at avoiding to solve the many-body Schrödinger equation by working with the charge density instead of the full many-body wave-function. The ions are often kept fixed and they produce an external potential, which is periodic in crystals.

DFT relies on two founding theorems. The first Hohenberg-Kohn theorem states that: *In an electronic system (interacting or not), there is a one-to-one correspondence between the electronic density and the external potential* [6]. The second theorem is based on the variational principle and states that the density which minimises the total energy,  $E^{\text{tot}}$ , is the exact ground-state density [6]. A practical implementation of DFT came with the Kohn-Sham scheme [7], where the Hohenberg-Kohn theorems are applied to both a physical, interacting system and an auxiliary, non-interacting system. This supposes that any physical system can be represented by an auxiliary non-interacting system. Hence, the construction of the auxiliary system is exact in principle.

Solving the Kohn-Sham system is relatively easy, because it amounts to solving a single-particle Schrödinger equation:

$$\left(-\frac{1}{2}\nabla^2 + v_{KS}(\mathbf{r})\right)\phi_i(\mathbf{r}) = \epsilon_i\phi_i(\mathbf{r}), \quad (3.12)$$

where the Kohn-Sham potential is

$$v_{KS}(\mathbf{r}) = v_{\text{ext}}(\mathbf{r}) + v_H(\mathbf{r}) + v_{xc}(\mathbf{r}), \quad (3.13)$$

where  $v_{\text{ext}}(\mathbf{r})$  is the external (ionic) potential;  $v_H(\mathbf{r})$  is the Hartree potential;  $v_{xc}(\mathbf{r})$  is the exchange and correlation potential.

The external potential  $v_{\text{ext}}(\mathbf{r})$  is given by the problem at hand and  $v_H(\mathbf{r})$  is immediately accessible via the electronic density. Instead, the exchange and correlation potential,  $v_{xc}(\mathbf{r})$ , is a complicated, in general non-explicit functional of the density. In practice, the exchange and correlation potential needs to be approximated. The most popular functionals are the so-called local or semi-local functionals: the Local-Density Approximation (LDA [7, 90, 91]) and the Generalised-Gradient Approximation (GGA [92]). In these functionals, the exchange and correlation potential is at each point a functional of the density or its gradients at this same point.

DFT is a functional of the density: it gives direct access to ground-state properties, such that the total energy. In principle, any observable of the system is a unique functional of the density. However, some byproducts of the Kohn-Sham construction are often

### 3.4. Accessing spectroscopy: Dynamical mean-field theory (DMFT)

---

employed without a rigorous justification. For example, the single-particle excitation energies of the Kohn-Sham system are often directly interpreted as excitations of the physical system. This is in principle not exact. However, this gives a useful estimate of the electronic structure of many compounds. One should however keep in mind that a band theory (an approach yielding effective independent-particle energy levels), even with the most accurate functional, cannot reproduce a true interacting spectral function, and in particular the Mott phenomenon in principle.

There are several extensions of DFT. One of them is time-dependent density-functional theory (TD-DFT [93]). In TD-DFT the central quantity is the time-dependent density, which can be described by an auxiliary system with a time-dependent effective potential, that is a functional of the density at all points in space and at all past times. Therefore, it gives access for example to the linear density-density response function, the poles of which are the energies of neutral excitations. One can also go beyond linear response, and TD-DFT is routinely used nowadays to compute the time evolution of molecules under a laser pulse, for example [94].

## 3.4 Accessing spectroscopy: Dynamical mean-field theory (DMFT)

### 3.4.1 DMFT

In order to access one-body excitations and spectral functions, DMFT introduces frequency-dependence. DMFT does not directly deal with the full, many-body Schrödinger equation (3.1). Instead, it gives insight on the simpler, yet challenging Hubbard model (1.15). For a review on how DMFT can be applied to realistic electronic-structure calculations, see [95]. A short introduction to DMFT is given by [96], while a detailed review is [9]. Many DMFT equations, as well as expressions for the Anderson impurity model, are expressed in the path-integral formalism. This formalism is explained in detail in [97].

Hence, DMFT aims at giving an approximate solution to a lattice problem, whose action is:

$$S[c^*, c] = \sum_{i,j,\sigma} \int_0^\beta d\tau c_{i\sigma}^*(\tau) [t_{ij} + (\partial_\tau - \mu)\delta_{ij}] c_{j\sigma}(\tau) + U \sum_i \int_0^\beta d\tau n_{i\uparrow}(\tau)n_{i\downarrow}(\tau), \quad (3.14)$$

where  $c_{i\sigma}^*, c_{i\sigma}$  are Grassmann variables corresponding to the fermionic creation and annihilation operators  $c_{i\sigma}^\dagger, c_{i\sigma}$ , respectively;  $\beta$  is the inverse temperature;  $t_{ij}$  is the hopping integral from site  $i$  to site  $j$ ;  $\partial_\tau$  is the partial differentiation operator in imaginary time;  $\mu$  is the chemical potential.

The steps that historically led to the invention of DMFT are described in [9]. Metzner

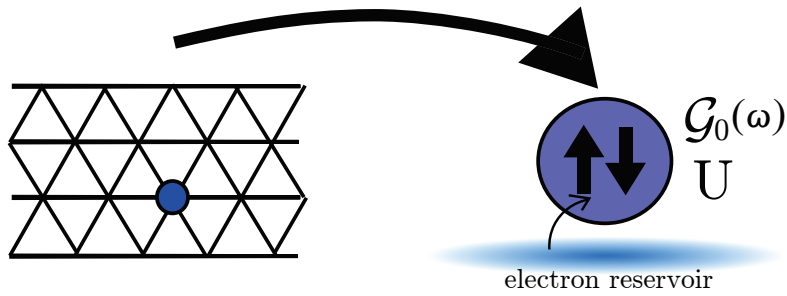


Figure 3.1: The DMFT maps a lattice problem onto an Anderson impurity model. The AIM retains the on-site interaction  $U$  as in the lattice. It is characterised by a *dynamical* mean-field,  $\mathcal{G}_0(\omega)$ .

and Vollhardt proved that *in the limit of infinite dimensions, the self-energy becomes local* [98]. This remark is the essence of the DMFT approximation. Next, Georges and Kotliar proposed a practical implementation scheme, where the lattice problem is mapped onto an Anderson impurity model [26]. Pretty much as the Kohn-Sham scheme is a practical implementation of DFT, the mapping on an AIM is the practical implementation of DMFT. This map is illustrated in Fig. 3.1.

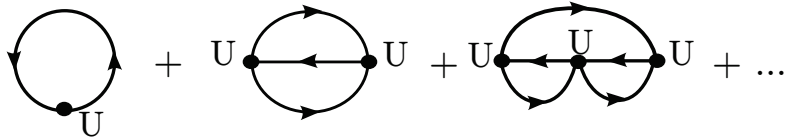


Figure 3.2: Lowest orders of self-energy diagrams. The full oriented lines represent fermionic propagators. The (four-point) vertices correspond to the local interaction  $U$ . In DMFT, only local diagrams, with local propagators, are considered. DMFT is non-perturbative and hence the sum of diagrams extends to all orders.

The approximation used by DMFT is the following: the self-energy of the lattice is local and given by the impurity. This implies, in particular, that the self-energy is the sum of all local diagrams. This last point makes the DMFT a non-perturbative theory: on the AIM, the diagrams are in principle evaluated to all orders. The diagrammatic expansion corresponding to the DMFT self-energy is represented in Fig. 3.2. The DMFT approximation can be expressed as a functional dependence of the DMFT self-energy:

$$\Sigma_{ij}(i\omega_n) = \delta_{ij} \Sigma_{\text{imp}}[G_{\text{imp}}, U](i\omega_n), \quad (3.15)$$

where  $i, j$  denote site indices and  $\omega_n$  denotes fermionic Matsubara frequencies. The assumption of a local self-energy translates into a vanishing  $\mathbf{k}$ -dependence of the same quantity. Local quantum fluctuations on the single-particle level are treated to all orders, resulting in the frequency-dependence of the self-energy [96].

### 3.4. Accessing spectroscopy: Dynamical mean-field theory (DMFT)

On the lattice, the self-energy and the Green's function are connected via the Dyson equation:

$$G_{ij}(i\omega_n) = G_{ij}^0(i\omega_n) + \sum_k G_{ik}^0(i\omega_n) \Sigma_{\text{imp}}[G_{\text{imp}}, U](i\omega_n) G_{kj}(i\omega_n), \quad (3.16)$$

where  $G^0$  is the non-interacting lattice Green's function and  $i, j, k$  denote site indices.

The DMFT self-consistency loop is summarised on the left-hand side of Fig. 3.3. In Fig. 3.3, the DMFT approximation amounts to take  $\Sigma(\mathbf{k}, i\omega_n) = \Sigma_{\text{imp}}(i\omega_n)$ . A crucial step in this loop is to compute the physical quantity  $G_{\text{imp}}$  of the AIM. This step involves an impurity solver.

The self-energy  $\Sigma_{\text{imp}}$  and the impurity Green's function,  $G_{\text{imp}}$ , are computed by solving a self-consistently determined Anderson impurity model:

$$S_{\text{imp}}^{\text{DMFT}}[c^*, c] = - \sum_{\sigma} \iint_0^{\beta} d\tau d\tau' c_{\sigma}^*(\tau) \mathcal{G}_0^{-1}(\tau - \tau') c_{\sigma}(\tau') + U \int_0^{\beta} d\tau n_{\uparrow}(\tau) n_{\downarrow}(\tau). \quad (3.17)$$

More specifically, the impurity Green's function is given by  $G_{\text{imp}} = - \langle \mathcal{T}_{\tau} c(\tau) c^{\dagger}(0) \rangle = - \frac{1}{Z} \int \mathcal{D}[c^*, c] c(\tau) c^*(0) e^{-S}$ . The impurity self-energy is obtained by inverting a single-site Dyson equation, on the impurity.

When self-consistency is reached, the local Green's function on the lattice and the impurity Green's function coincide:  $G_{\text{loc}}(i\omega_n) = G_{\text{imp}}(i\omega_n)$ .

#### 3.4.2 Extended dynamical mean-field theory

An extension of DMFT, called extended DMFT (EDMFT), aims at treating systems with non-local Coulomb interaction terms. In the absence of non-local interactions, EDMFT reduces to DMFT. A pedagogical introduction to EDMFT can be found in [99]. The prototypical Hamiltonian for this is the extended Hubbard Hamiltonian:

$$\mathcal{H} = \sum_{i,j,\sigma} t_{ij} c_{i\sigma}^{\dagger} c_{j\sigma} + \frac{1}{2} \sum_{i,j} v_{ij} n_i n_j \quad (3.18)$$

$$= \sum_{i,j,\sigma} t_{ij} c_{i\sigma}^{\dagger} c_{j\sigma} + \frac{1}{2} \sum_{i \neq j} v_{ij} n_i n_j + U \sum_i n_{i\uparrow} n_{i\downarrow} + \frac{U}{2} \sum_i n_i, \quad (3.19)$$

where  $v_{ij}$  is a non-local Coulomb interaction term. To make contact with the previous paragraph, we denote  $v_{ii} = U$ . The normal-ordered extended Hubbard Hamiltonian, Eq. (3.19), can be expressed in a path-integral formalism:

$$S[c^*, c] = \sum_{i,j,\sigma} \int_0^{\beta} d\tau c_{i\sigma}^*(\tau) \left[ t_{ij} + (\partial_{\tau} - \mu + \frac{U}{2}) \delta_{ij} \right] c_{j\sigma}(\tau) + \frac{1}{2} \sum_{i,j} \int_0^{\beta} d\tau v_{ij} n_i(\tau) n_j(\tau).$$

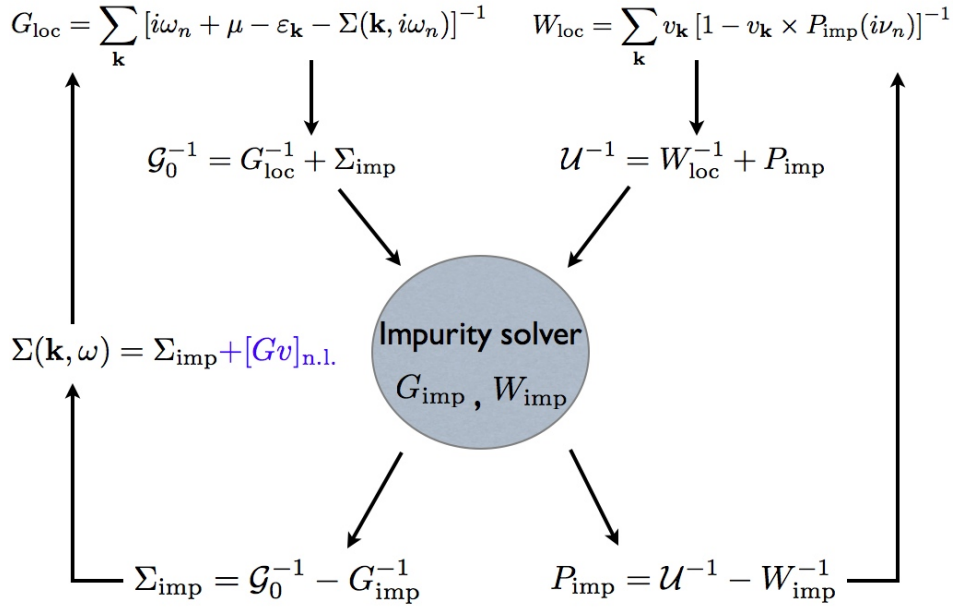


Figure 3.3: The (Fock +) extended dynamical mean-field self-consistent loop. A non-local Fock term (blue) is optionally included in the self-energy, leading to the Fock + EDMFT scheme. The left part of the scheme (without the Fock term) reduces to the DMFT self-consistency loop.

(3.20)

The quadratic term in the action (3.20) can be decoupled via a Hubbard-Stratonovitch transformation. This transformation amounts to introducing an auxiliary bosonic field,  $\phi$ , that mediates the Coulomb interaction. The Hubbard-Stratonovitch transformation [100] relies on the Gaussian identity:

$$\begin{aligned} & \exp\left(\frac{1}{2} \int_0^\beta d\tau b_i(\tau) A_{ij} b_j(\tau)\right) \\ &= \int \frac{\mathcal{D}[x_1(\tau), \dots, x_N(\tau)]}{\sqrt{(2\pi)^N \det A}} \times \exp\left(\int_0^\beta d\tau \left[-\frac{1}{2} x_i(\tau) [A^{-1}]_{ij} x_j(\tau) \mp x_i(\tau) b_i(\tau)\right]\right), \end{aligned} \quad (3.21)$$

where  $A$  is a symmetric positive-definite matrix;  $b_i(\tau)$  is a periodic (i.e., bosonic) field;  $x_i(\tau)$  is a real periodic field; summation over repeated indices is assumed. Applying the

### 3.4. Accessing spectroscopy: Dynamical mean-field theory (DMFT)

Hubbard-Stratonovitch transformation to the lattice action (3.20) yields:

$$S[e^*, c, \phi] = \int_0^\beta d\tau \left[ - \sum_{ij\sigma} c_{i\sigma}^* [(G_0)^{-1}]_{ij} c_{j\sigma}(\tau) \right] + \int_0^\beta d\tau \left[ \frac{1}{2} \sum_{ij} \phi_i(\tau) [v^{-1}]_{ij} \phi_j(\tau) + i \sum_i \phi_i(\tau) n_i(\tau) \right], \quad (3.22)$$

where the fermion lattice non-interacting Green's function is  $[(G_0)^{-1}]_{ij} = (-\partial_\tau + \mu - \frac{U}{2})\delta_{ij} - t_{ij}$ . On the lattice, the fermionic and bosonic Green's functions are the propagators:

$$G_{ij}(\tau - \tau') = - \langle \mathcal{T}_\tau c_i(\tau) c_j^*(\tau') \rangle \quad (3.23a)$$

$$W_{ij}(\tau - \tau') = \langle \mathcal{T} \phi_i(\tau) \phi_j(\tau') \rangle. \quad (3.23b)$$

On the lattice, the fermionic and bosonic propagators obey each a Dyson equation:

$$G^{-1}(\mathbf{k}, \omega) = G_0^{-1}(\mathbf{k}, \omega) - \Sigma(\mathbf{k}, \omega) \quad (3.24a)$$

$$W^{-1}(\mathbf{q}, \omega) = v^{-1}(\mathbf{q}) - P(\mathbf{q}, \omega), \quad (3.24b)$$

where  $P$ , the polarisation (also called irreducible polarisability in other contexts), is the bosonic self-energy. Alternatively,  $W$  obeys another Dyson equation, involving the charge susceptibility:

$$W(\mathbf{q}, \omega) = v(\mathbf{q}) - v(\mathbf{q})\chi(\mathbf{q}, \omega)v(\mathbf{q}), \quad (3.25)$$

where the charge susceptibility takes the expression  $\chi_{ij}(\tau) = \langle \mathcal{T}_\tau n_i(\tau) n_j(0) \rangle - \langle n \rangle^2$ .

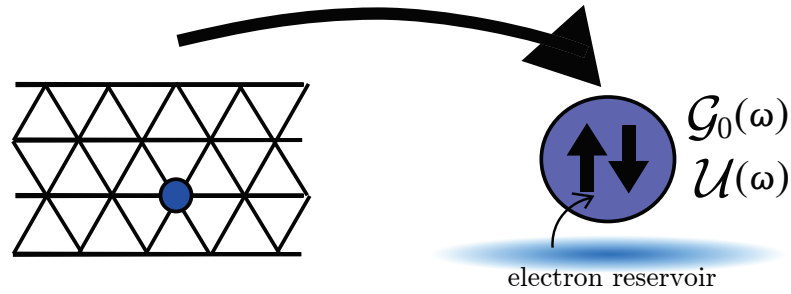


Figure 3.4: The EDMFT maps a lattice problem onto an Anderson impurity model with dynamical interactions. It is characterised by two *dynamical* mean-fields,  $\mathcal{G}_0(\omega)$  and  $\mathcal{U}(\omega)$ .

In EDMFT, the lattice problem, Eq. (3.22), is mapped onto an impurity problem with dynamical interactions, as depicted in Fig. 3.4. While in DMFT, the interaction on the AIM is parametrised by  $U$  as on the lattice, in EDMFT it is dynamical. EDMFT

treats non-local interactions,  $v_{ij}$ , by transforming them into a frequency-dependent local interaction,  $\mathcal{U}(\omega)$  [101].

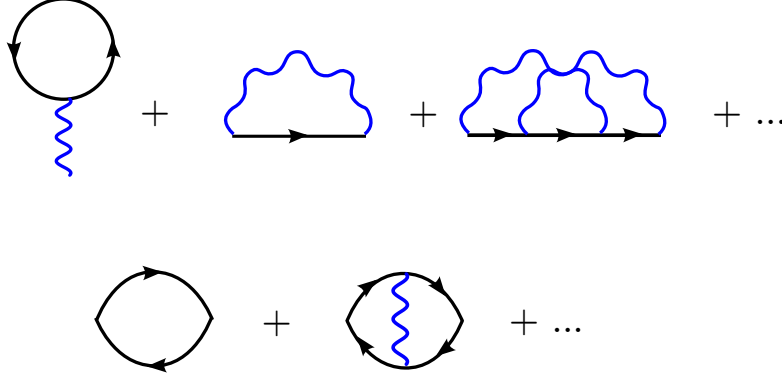


Figure 3.5: Top: lowest orders of self-energy diagrams. Bottom: First orders of polarisation diagrams. The full oriented lines represent fermionic propagators. The wavy lines correspond to bosonic propagators. In EDMFT, only local diagrams, with local propagators, are considered. EDMFT is non-perturbative and hence the sum of diagrams extends to all orders.

The approximation used by EDMFT is similar in spirit to the one of DMFT. In EDMFT, both the fermionic and bosonic self-energies ( $\Sigma$  and  $P$ ) are local, and given by the impurity. This means that they are both the sum of all local diagrams, as depicted in Fig. 3.5. As for DMFT, EDMFT is a non-perturbative theory. This is expressed by the functional dependence of the EDMFT self-energy and polarisation:

$$\Sigma_{ij}(i\omega_n) = \delta_{ij} \Sigma_{\text{imp}}[G_{\text{imp}}, W_{\text{imp}}](i\omega_n), \quad (3.26a)$$

$$P_{ij}(i\nu_n) = \delta_{ij} P_{\text{imp}}[G_{\text{imp}}, W_{\text{imp}}](i\nu_n). \quad (3.26b)$$

$\omega_n$  and  $\nu_n$  denote respectively fermionic and bosonic Matsubara frequencies.

On the lattice, the self-energy and the Green's function, and the polarisation and the screened Coulomb interaction, are connected via the two Dyson equations:

$$G_{ij}(i\omega_n) = G_{ij}^0(i\omega_n) + \sum_k G_{ik}^0(i\omega_n) \Sigma_{\text{imp}}[G_{\text{imp}}, G_{\text{imp}}](i\omega_n) G_{kj}(i\omega_n), \quad (3.27a)$$

$$W_{ij}(i\nu_n) = v_{ij}^0 + \sum_k v_{ik} P_{\text{imp}}[G_{\text{imp}}, W_{\text{imp}}](i\nu_n) W_{kj}(i\nu_n), \quad (3.27b)$$

where  $G^0$  is the non-interacting lattice Green's function and  $i, j, k$  denote site indices.

Again, the self-energy, impurity the Green's function, the polarisation  $P_{\text{imp}}$ , and the impurity screening  $W_{\text{imp}}$ , are computed self-consistently by solving an impurity model,

### 3.4. Accessing spectroscopy: Dynamical mean-field theory (DMFT)

featuring a self-consistently determined dynamical local interaction,  $\mathcal{U}(i\nu_n)$ :

$$\begin{aligned} S_{\text{imp}}^{\text{EDMFT}}[c^*, c] = & - \sum_{\sigma} \iint_0^{\beta} d\tau d\tau' c_{\sigma}^*(\tau) \mathcal{G}_0^{-1}(\tau - \tau') c_{\sigma}(\tau') \\ & + \frac{1}{2} \iint_0^{\beta} d\tau d\tau' \mathcal{U}(\tau - \tau') n(\tau) n(\tau'). \end{aligned} \quad (3.28)$$

The EDMFT self-consistency loop is summarised in Fig. 3.3, without including the Fock term (blue). At self-consistency, the following equalities hold:  $G_{\text{loc}} = G_{\text{imp}}$  and  $W_{\text{loc}} = W_{\text{imp}}$ .

#### 3.4.3 Fock + EDMFT

On top of the purely local self-energy diagrams treated by EDMFT, a non-local Fock term is optionally added. This non-local Fock term is induced by the non-local interaction. Indeed, let us have a look at the first perturbative self-energy diagrams of the extended Hubbard Hamiltonian, Eq. (3.19). Let us assume for simplicity that the non-local term is produced by nearest-neighbour interactions only:  $v_{ij} = U\delta_{ij} + V\delta_{\langle ij \rangle}$ . The Hartree and Fock self-energies are, respectively:

$$\Sigma_{ij,\sigma}^H(i\omega) = \Sigma_{ii,\sigma}^H \delta_{ij} = \left( U n_{i,\bar{\sigma}} + V \sum_{\langle i,l \rangle} n_l \right) \delta_{ij}, \quad (3.29)$$

$$\Sigma_{ij,\sigma}^F(i\omega) = -\delta_{\langle ij \rangle} V G_{ij,\sigma}(\tau = 0^+), \quad (3.30)$$

The Hartree terms are local and static, so they can be absorbed in a redefinition of the chemical potential,  $\tilde{\mu} = \mu - \frac{U}{2} n_i - V \sum_{\langle i,l \rangle} n_l$ , provided that the charge density is homogeneous. The Fock term, however, is static but non-local, and, by definition, is not included in the EDMFT scheme.

The Fock term contributes to a static, non-local, real part to the self-energy. Thus, at self-consistency, it can be viewed as a modification to the bare dispersion,  $\epsilon_{\mathbf{k}}$ . The non-local exchange term induces more delocalisation of the charge carriers. In practice, it leads to a stretching of the effective non-interacting band, as is depicted in Fig. 4.1 of Part II. To this renormalised effective non-interacting band, it is possible to ascribe a density of states. At the Fermi level, the renormalised density of states is lower than the bare density of states. This point will be essential to interpret some results of Part II.

Hence, the usual EDMFT scheme does not include all the first-order diagrams in  $V$ . In the Fock + EDMFT scheme, we make sure that the Hartree-Fock diagrams are at least present, on top of the local EDMFT diagrams. Fock + EDMFT can be viewed as a poor-man's  $GW$  + EDMFT. However it does not suffer from the same problems as Hartree-Fock, because some screening processes are included via the local polarisation terms. Contrary to DMFT, EDMFT, (self-consistent)  $GW$  or  $GW$  + EDMFT, Fock+EDMFT does not

derive from a functional.

### 3.4.4 $GW + \text{EDMFT}$

EDMFT only uses local diagrams to evaluate the self-energy and the polarisation. Hence, the EDMFT self-energy and polarisation are momentum-independent. They capture only purely local correlation processes. It is possible to introduce some non-local exchange and correlation processes by considering the first-order self-energy and polarisation diagrams:

$$\Sigma_{ij}^{GW}(\tau) = -G_{ij}(\tau)W_{ij}(\tau), \quad (3.31a)$$

$$P_{ij}^{GW}(\tau) = 2G_{ij}(\tau)G_{ji}(-\tau). \quad (3.31b)$$

These first-order non-local diagrams follow directly from the Hedin equations, where the three-leg vertex is set to 1 [102]. The self-energy and the polarisation of the combined,  $GW + \text{EDMFT}$  scheme correspond to the addition:

$$\Sigma^{GW+\text{EDMFT}}(\mathbf{k}, i\omega_n) = \Sigma_{\text{imp}}(i\omega_n) + \Sigma^{GW}(\mathbf{k}, i\omega_n) - \left[ \Sigma^{GW} \right]_{\text{loc}}(i\omega_n), \quad (3.32a)$$

$$P^{GW+\text{EDMFT}}(\mathbf{q}, i\nu_n) = P_{\text{imp}}(i\nu_n) + P^{GW}(\mathbf{k}, i\nu_n) - \left[ P^{GW} \right]_{\text{loc}}(i\nu_n). \quad (3.32b)$$

In order to avoid double-counting in the corresponding diagrammatic summation, the local, first-order diagrams are subtracted. The approach was first proposed by Biermann *et al* [103]. It has since then been applied to various systems [104, 99, 105], from lattice models to ad-atoms on surfaces.

**Extended Dynamical Mean-Field Theory for the Extended  
Hubbard Model on a Triangular  
Lattice at High Doping** **Part II**



## 4 A model for the cobaltates

As mentioned in Chap. 2, the cobaltates are complex materials, and their intriguing physical properties can be ascribed to the interplay between many degrees of freedom. In this thesis, we want to focus on electronic correlation effects. These are expected to be important, as evidenced by photoemission spectroscopy, with a strongly reduced low-energy dispersion, as compared to LDA calculations<sup>1</sup> [55, 53]. Treating electronic correlations requires the use of advanced, non-perturbative many-body techniques. Furthermore, one of our motivations being charge disproportionation, we want to monitor charge fluctuations. To describe both charge fluctuations and strong correlations, the extended dynamical mean-field theory (EDMFT) is a method of choice.

Dynamical mean-field-based approaches do not treat directly the whole electronic system. Instead, a first step is to define an effective, low-energy (possibly incorporating the effects of high-energy bands) lattice Hamiltonian. In this part, we use the extended Hubbard model:

$$\mathcal{H} = \sum_{i,j,\sigma} t_{ij} c_{i\sigma}^\dagger c_{j\sigma} + U \sum_i n_{i\uparrow} n_{i\downarrow} + V \sum_{\langle i,j \rangle} n_i n_j, \quad (4.1)$$

where  $c_{i\sigma}^\dagger, c_{i\sigma}$  are electronic creation and annihilation operators, respectively, for site  $i$  and spin  $\sigma$ ;  $n_i = n_{i\uparrow} + n_{i\downarrow} = c_{i\uparrow}^\dagger c_{i\uparrow} + c_{i\downarrow}^\dagger c_{i\downarrow}$  is the total density on site  $i$ . The sum  $\sum_i$  runs on all lattice sites, while  $\sum_{\langle i,j \rangle}$  runs on all lattice bonds, or equivalently on all nearest-neighbour doublets. In the extended Hubbard model, on top of the usual parameters of the Hubbard model, a non-local Coulomb repulsion term,  $V$ , is considered.

This chapter deals with the issue of designing an effective lattice Hamiltonian. Even though such a Hamiltonian constitutes a simplification over the whole many-body problem, the low-energy model can be chosen in a realistic way [106, 107]. This allows for quantitatively predictive simulations, that can be compared to experimental findings.

---

<sup>1</sup>Of course, one has to be careful. In particular, LDA contains self-interaction because it approximates the exchange contribution. This may have an effect on the dispersion but it is not a correlation effect.

We first describe the charge-fluctuation mechanisms created by a non-local Coulomb repulsion term. Second, we explain how to obtain the kinetic parameters of the model from *ab initio* calculations. Third, we show how to estimate the interaction parameters of the model.

### 4.1 Capturing charge fluctuations from non-local Coulomb interactions

In Chapter 2, we described the experimental phase diagram of the cobaltates. This phase diagram displays many instabilities, among which charge disproportionation between cobalt atoms in the high-doping region [46, 10].

Non-local Coulomb interactions have been known to give rise to such interesting charge-ordering patterns. On the square lattice, where the extended Hubbard model has been studied at half- [108, 99] and quarter-filling [109], a transition is found between a homogeneous metallic phase and a charge-ordered phase (with possibly an intermediate ordered metallic phase) upon increasing the nearest-neighbour interaction  $V$ . In both cases, the ordering pattern was commensurate to the square lattice, with a  $2 \times 0$  pattern for half-filling, and a  $1 \times 0$  pattern for quarter-filling.

The triangular lattice, however, can display geometrical frustration upon the inclusion of a nearest-neighbour interaction  $V$  on top of a local  $U$  (as in the half-filled triangular plaquette). In particular, several studies on the extended Hubbard model on the triangular lattice show that the interplay between quantum hopping, local and non-local Coulomb interactions can give rise to exotic quantum-mechanical ground states with complex superstructures. These studies were pioneered by Hotta *et al.*, who analysed spinless fermions, forming a pinball liquid at specific incommensurate dopings [110, 111, 112]. The pinball liquid is an exotic phase combining charge order and metallicity. These two properties could *a priori* be believed to be mutually exclusive. Indeed, a metal assumes the existence of extended states, while charge-ordering assumes the localisation of electrons. In a pinball liquid however, charge carriers get segregated, into localised particles forming a superstructure, and itinerant ones extending over the solid. A similar behaviour, with particle segregation, was later found for hard-core bosons, with a supersolid transition at intermediate doping [113, 114, 115, 116]. More recent studies performed a systematic analysis of the fermionic single-band extended Hubbard model on a triangular lattice as a function of doping, and unraveled a complex phase diagram [117, 118, 119, 120]. A variety of superstructures may appear, minimising the interaction energy. As a function of doping, these states may be insulating, with all electrons localised around specific atoms, or metallic, with the existence of extended states, as in a pinball liquid. Even if the triangular lattice is most famous for displaying spin frustration at half-filling, with the well-known picture of antiferromagnetically-coupled Ising spins, charge-ordering is a key physical phenomenon at incommensurate filling.

In this thesis, we describe observables in the homogeneous phase, close to the transition, where we expect charge-fluctuations to become important. We compute both one-particle Green's functions, and charge susceptibilities, via EDMFT, on the extended Hubbard model.

## 4.2 A realistic model

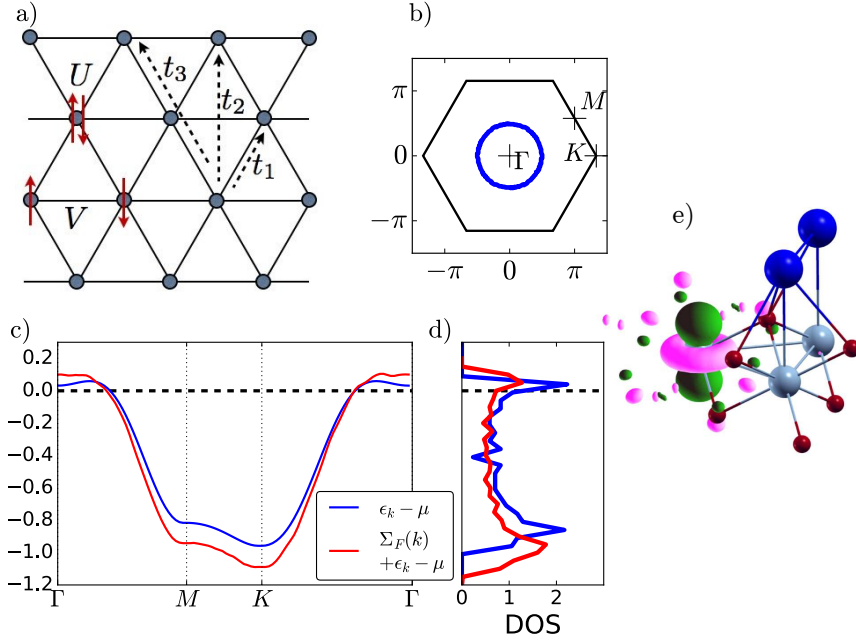


Figure 4.1: The non-interacting model, as extracted from the study of Piefke *et al.* [121]. a) The effective two-dimensional model on a triangular lattice, with the hopping and interaction parameters. The hopping is parametrised up to the third nearest neighbour (parameters taken from Piefke *et al.* [121]), and the interaction is parametrised up to the nearest neighbour. b) The Wigner-Seitz cell of the triangular lattice, with high-symmetry points. Blue: the non-interacting Fermi surface is composed of one circular sheet, centered around the  $\Gamma$  point. c) The bare dispersion, together with the dispersion modified by the Fock self-energy. The chemical potential lies close to the band edge, such that the filling is  $\langle n_\sigma \rangle = 0.83$  (1.67 electrons per site). d) Corresponding densities of states. Note the two van Hove singularities, corresponding to a flattening in the band dispersion. e) Localised Wannier function, from Piefke *et al.* [121]. The Wannier function is centered around a cobalt atom (grey sphere). It is slightly hybridised with oxygen atoms (red spheres). Blue spheres mark sodium ions.

We perform simulations on a realistic model, that accounts reliably for physical observables in a given low-energy window. The cobaltates are composed of a stacking of  $\text{CoO}_2$  planes, with a weak dispersion along  $k_z$ , which justifies a two-dimensional model. Furthermore, the low-energy bands, namely the  $t_{2g}$  manifold, have essentially cobalt character. It

thus appears natural to consider an effective two-dimensional triangular lattice model, describing quantum hopping from one cobalt site to another.

There are in principle three  $t_{2g}$  orbitals to account for, per cobalt atom. However, in ARPES experiments, only the  $a_{1g}$  symmetric band is found to cross the Fermi level [55, 60, 56, 58]. The other two bands have a different character. This justifies the use of a one-band model.

The non-interacting parameters of the extended Hubbard model need to be adjusted to best represent a certain mean-field description of the cobaltates. Typically, the non-interacting parameters,  $t_{ij}$ , are chosen to reproduce a low-energy DFT band structure. This is the basis of the LDA+DMFT method [122, 123, 124, 106]. In this thesis, we follow a parametrisation by Piefke et al [121], illustrated in Fig. 4.1. The non-interacting band, derived from  $a_{1g}$ , was expressed in a Wannier-like basis, using the maximally-localised procedure [125, 126]. The obtained Wannier orbital is centered around a cobalt atom, with a weak oxygen hybridisation.

Let us give more details about the parametrised  $a_{1g}$ -like non-interacting band. In the Hamiltonian given by Eq. (4.1), the hopping parameters  $t_{ij}$  are the Fourier transform of  $\varepsilon_{\mathbf{k}}$ , represented in Fig. 4.1. More specifically,  $\varepsilon_{\mathbf{k}}$  is parametrised up to the third nearest neighbour via the dispersion relation on the triangular lattice:

$$\begin{aligned} \varepsilon_{\mathbf{k}} = & 2t_1 \left( \cos(k_x) + 2 \cos(k_x/2) \cos(k_y \sqrt{3}/2) \right) \\ & + 2t_2 \left( \cos(\sqrt{3}k_y) + 2 \cos(3k_x/2) \cos(k_y \sqrt{3}/2) \right) \\ & + 2t_3 \left( \cos(2k_x) + 2 \cos(k_x) \cos(\sqrt{3}k_y) \right), \end{aligned} \quad (4.2)$$

where

$$t_1 = -0.134 \text{ eV}, \quad t_2 = +0.028 \text{ eV}, \quad t_3 = +0.024 \text{ eV}. \quad (4.3)$$

We note that the one-band parametrisation leads to a negative effective nearest-neighbour hopping,  $t_1 < 0$ . The hopping parameters  $t_{ij}$  are in the range of 100 meV, but due to the high connectivity of the triangular lattice, the non-interacting bandwidth is approximately 1.1 eV, as can be seen in the non-interacting density of states in Fig. 4.1. Two van Hove singularities appear at energies  $-0.8$  eV and  $0.05$  eV, due to a flattening of the band dispersion at the  $M$  point and at the  $\Gamma$  point. The non-interacting Fermi surface is composed of one sheet, with a hole pocket centered around the  $\Gamma$  point.

We want to study the cobaltates in their strongly-doped regime, namely  $x = 2/3$ . In our one-band model, this translates in an average filling  $\langle n_{\sigma} \rangle = 0.83$  per spin. As shown in Fig. 4.1, with the Fermi level close to the band edge, we are close to the band-insulating limit. This means there are few charge carriers, namely few holes, in the system.

### 4.3 Choice of interaction parameters

Over a long time, the determination of interaction parameters has been considered a major drawback of DMFT-based approaches to compute real-material properties. However, this situation is changing, with the advent of the constrained random-phase approximation (cRPA) [127, 128, 129]. It is in principle possible to compute the interaction parameters,  $U$  and  $V$ , from *ab initio* methods. We will come back to the *ab initio* determination of  $U$  and  $V$  in Chap. 9.

For now, we rely on photoemission measurements at doping  $x = 0.7$  to obtain an estimate for the value of  $U$  [55]. In these experiments, a high-energy correlation satellite is interpreted as resulting from a local  $U \approx 5$  eV. This value has to be compared to our non-interacting bandwidth  $W = 1.1$  eV (Fig. 4.1). We are in a case where  $W < U$ , and the large interaction strength justifies the use of methods for strong correlations.

With the inclusion of both a local and a nearest-neighbour interaction term, the Fourier transform of  $v_{ij}$  can be expressed as follows in reciprocal space:

$$v_{\mathbf{k}} = U + 2V \left( \cos(k_x) + 2 \cos\left(\frac{k_x}{2}\right) \cos\left(\frac{\sqrt{3}k_y}{2}\right) \right). \quad (4.4)$$

To summarise, we want to simulate a one-band extended Hubbard Hamiltonian on a triangular lattice, that takes the form:

$$\mathcal{H} = \sum_{\mathbf{k}, \sigma} \epsilon_{\mathbf{k}} c_{\mathbf{k}\sigma}^\dagger c_{\mathbf{k}\sigma} + \frac{1}{2} \sum_{\mathbf{q}} v_{\mathbf{q}} n_{\mathbf{q}} n_{-\mathbf{q}}. \quad (4.5)$$

The kinetic parameters,  $\epsilon_{\mathbf{k}}$ , are taken from a parametrisation of *ab initio* results from Piefke *et al.* [121]. The interaction parameters are estimated from photoemission experiments [55].



# 5 Extended Dynamical Mean-Field Theory in Practice

In this chapter, we present our implementation of the extended dynamical mean-field theory (EDMFT). We describe how to run the algorithm step by step. We also present how to control the qualitative behaviour of all the self-consistent quantities.

The EDMFT implementation used in this work was written by Thomas Ayrál, using the TRIQS toolbox [27]. More details about the implementation can be found in [130]. The algorithm is written in two main steps, using two different objects: the implementation of the self-consistency condition and the impurity solver. These two objects, with their inputs and outputs, are represented in Fig. 5.1.

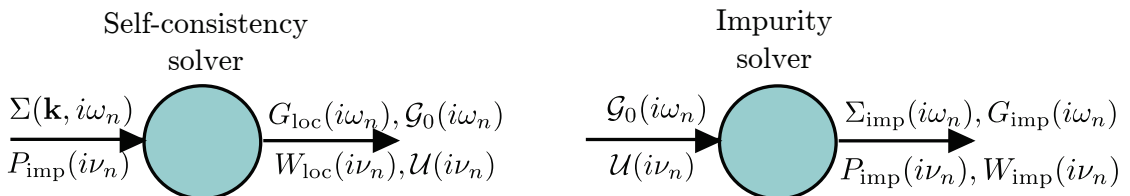


Figure 5.1: The two main objects, with their inputs and outputs. Left: the self-consistency object takes a self-energy and a polarisation as input; it outputs lattice local observables, and Weiss fields. The impurity solver takes Weiss fields as input, and outputs an impurity self-energy and polarisation, as well as impurity observables.

## 5.1 Implementation of the self-consistency condition

The object implementing self-consistency performs Dyson equations on the lattice. It takes a lattice self-energy and polarisation as input, and outputs a lattice local Green's function and local screened interaction, as represented on the left-hand side of Fig. 5.1.

On the lattice, all quantities are functions of  $\mathbf{k}$  and  $\omega$ . Computing a quantity which

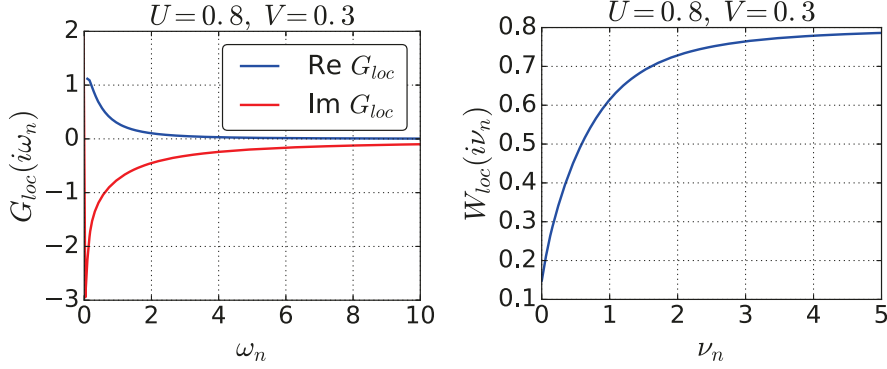


Figure 5.2: Lattice local quantities, computed when implementing self-consistency, using Eqs. 5.1. On the left, the local Green's function is represented. On the right the local screened Coulomb interaction is represented.

is local on the lattice amounts to perform a  $\mathbf{k}$ -summation. The self-consistency object computes the lattice local quantities by inverting Dyson equations on the lattice in frequency space:

$$G_{loc}(i\omega_n) = \sum_{\mathbf{k}} G(\mathbf{k}, i\omega_n) = \sum_{\mathbf{k}} \frac{1}{i\omega_n - \epsilon_{\mathbf{k}} + \mu - \Sigma(\mathbf{k}, i\omega_n)}, \quad (5.1a)$$

$$W_{loc}(i\nu_n) = \sum_{\mathbf{q}} W(\mathbf{q}, i\nu_n) = \sum_{\mathbf{q}} \frac{v_{\mathbf{q}}}{1 - v_{\mathbf{q}} P_{imp}(i\nu_n)}, \quad (5.1b)$$

where  $\Sigma(\mathbf{k}, i\omega_n)$  and  $P_{imp}(i\nu_n)$  are given as inputs to the self-consistency object. The (lattice) self-energy is defined as:

$$\Sigma(\mathbf{k}, i\omega_n) = \Sigma_{imp}(i\omega_n) \quad \text{for EDMFT}, \quad (5.2a)$$

$$\Sigma(\mathbf{k}, i\omega_n) = \Sigma_{imp}(i\omega_n) + \Sigma_{n.l.}(\mathbf{k}, i\omega_n) \quad \text{for Fock + EDMFT}, \quad (5.2b)$$

where  $\Sigma_{n.l.,i,j}(i\omega_n) = \delta_{(i,j)} V G_{i,j}(\tau = 0^+)$  is the non-local Fock term. In Eq. (5.1a),  $\mu$  is the chemical potential. In our case, the chemical potential is adjusted iteratively by the self-consistency object in order to reach the desired filling. The lattice quantities are computed in the first Brillouin zone, on a discretised  $32 \times 32$   $\mathbf{k}$ -point grid. Typical local lattice quantities are represented in Fig. 5.2. The Green's function is a fermionic propagator; it hence has both a real and an imaginary part. It goes to zero at high frequencies as  $G_{loc}(i\omega_n) \sim 1/(i\omega_n)$ . The screened Coulomb interaction corresponds to a bosonic propagator (see Eq. (3.23b)) and hence it is purely real on the imaginary-frequency axis. At high-frequency, the screened Coulomb interaction goes to the bare, unscreened value  $U$ . The static, fully screened value  $W_{loc}(i\nu_n = 0) = U_0 < U$  is reduced due to the presence of non-local interaction terms.

Once the lattice Dyson equations are inverted (Eq. (5.1)), computing the effective Weiss

## 5.1. Implementation of the self-consistency condition

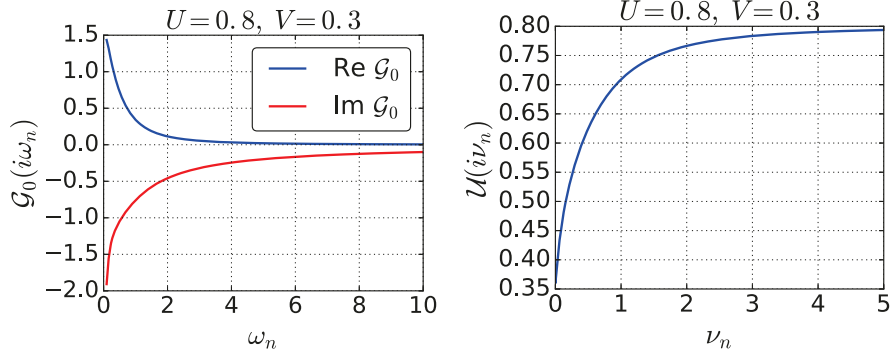


Figure 5.3: The fermionic (left) and bosonic (right) Weiss fields. The fermionic Weiss field defines the chemical potential on the AIM and the hybridisation function. The tail of the bosonic Weiss field defines the asymptotic interaction, in principle equal to  $U$ .

fields,  $\mathcal{G}_0$  and  $\mathcal{U}$ , is simply a matter of inverting two single-site Dyson equations in frequency-space:

$$\mathcal{G}_0^{-1}(i\omega_n) = G_{\text{loc}}^{-1}(i\omega_n) + \Sigma_{\text{imp}}(i\omega_n), \quad (5.3a)$$

$$\mathcal{U}^{-1}(i\nu_n) = W_{\text{loc}}^{-1}(i\nu_n) + P_{\text{imp}}(i\nu_n). \quad (5.3b)$$

Then, the high-energy tails of the Weiss fields are fitted. The Weiss fields are represented in Fig. 5.3. The tail of the fermionic Weiss field,  $\mathcal{G}_0$ , provides the chemical potential on the impurity. Expanding the fermionic Weiss field:

$$\mathcal{G}_0(i\omega_n) = \frac{1}{i\omega_n} - \frac{a_0}{(i\omega_n)^2} + \dots, \quad (5.4)$$

one can define the hybridisation function,  $\Delta(i\omega_n)$ , as:

$$\Delta(i\omega_n) = i\omega_n + a_0 - \mathcal{G}_0^{-1}. \quad (5.5)$$

Hence, the hybridisation function has no first- and zeroth-order moment. The hybridisation function is the quantity that is expanded upon in the CT-HYB algorithm (see next section). The chemical potential on the impurity is defined as the zeroth-order moment in the inverse effective bare propagator  $\mathcal{G}_0^{-1}(i\omega_n)$ , such that  $\mu_{\text{AIM}} = a_0$ .

The tail of the bosonic Weiss field,  $\mathcal{U}(i\nu_n)$ , provides an asymptotic value for the interaction (in principle equal to  $U$ ). In Fig. 5.3, the bosonic Weiss field indeed goes to  $U = 0.8$  at high frequency.

## 5.2 The impurity solver

The impurity solver solves the Anderson impurity problem with dynamical interactions (see also Eq. 3.28):

$$\begin{aligned}
 S_{\text{imp}}^{\text{EDMFT}}[c^*, c] = & - \sum_{\sigma} \iint_0^{\beta} d\tau d\tau' c_{\sigma}^*(\tau) \mathcal{G}_0^{-1}(\tau - \tau') c_{\sigma}(\tau') \\
 & + \frac{1}{2} \iint_0^{\beta} d\tau d\tau' \mathcal{U}(\tau - \tau') n(\tau) n(\tau').
 \end{aligned}
 \tag{5.6}$$

The path-integral action, Eq. (5.6) is expressed in imaginary time  $\tau$ , and  $\beta$  is the inverse temperature. The Grassmann variables  $c^*, c$  correspond to the fermionic operators  $c^{\dagger}, c$  respectively. We denoted  $n = \sum_{\sigma=\uparrow, \downarrow} c_{\sigma}^* c_{\sigma}$ , which is a bosonic variable. Hence, the impurity solver takes the Weiss fields,  $\mathcal{G}_0$  and  $\mathcal{U}$ , as input, and computes the impurity self-energy and the impurity polarisation. The impurity problem, Eq. (5.6), is solved with a continuous-time quantum Monte-Carlo solver (CTQMC [131]), using a hybridisation expansion [132] in the segment picture, with frequency-dependent interactions  $\mathcal{U}(i\nu_n)$  [133]. The impurity observables, among which the Green's function  $G_{\text{imp}}(\tau)$  and the charge susceptibility  $\chi_{\text{imp}}(\tau)$ , are computed in imaginary-time. Their Fourier-transform is computed at the end of the calculation. The fermionic self-energy,  $\Sigma_{\text{imp}}(i\omega)$ , is computed using improved estimators [134] and the polarisation is computed from the charge susceptibility:

$$\chi_{\text{imp}}(\tau) = \langle \mathcal{T}_{\tau} n(\tau) n(0) \rangle - \langle n \rangle^2
 \tag{5.7}$$

using the expression:

$$P_{\text{imp}}(i\nu_n) = - \frac{\chi_{\text{imp}}(i\nu_n)}{1 - \mathcal{U}(i\nu_n) \chi_{\text{imp}}(i\nu_n)}.
 \tag{5.8}$$

At the end of the impurity solver, the high-frequency tail of the self-energy is fitted, in order to smooth-out the Monte-Carlo noise. However, this step is not crucial when using the improved estimators, that already reduce significantly the Monte-Carlo noise.

Typical impurity observables are represented in Fig. 5.4. The impurity Green's function is computed in imaginary-time and is represented on the segment  $[0, \beta]$ . The fact that it is asymmetric comes from the fact that the system is away from half-filling. For an insulator,  $G(\beta/2) = 0$ . A finite value for  $G_{\text{imp}}(\beta/2)$  as in Fig. 5.4 hence indicates a metallic character. The impurity susceptibility is represented in imaginary-frequency in Fig. 5.4. In principle, within EDMFT, the impurity susceptibility does not correspond to the local susceptibility on the lattice; yet it can yield interesting information, as will be discussed in Chap. 6.

The self-energy, as computed by the impurity solver, is presented in Fig 5.5. The

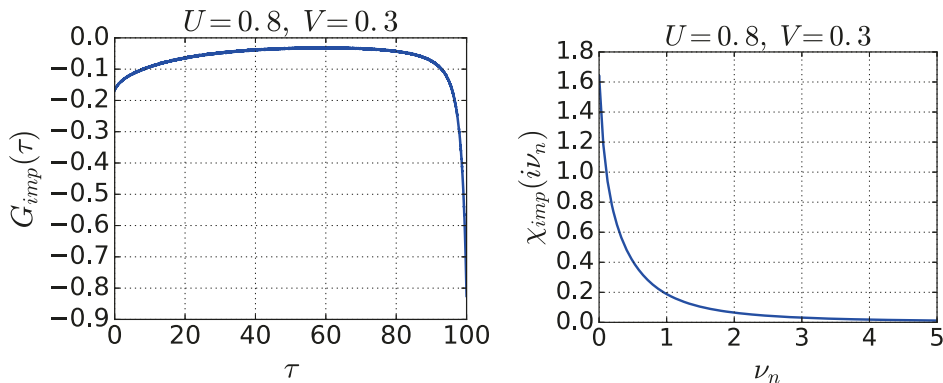


Figure 5.4: Impurity observables. On the left-hand side, the impurity Green's function is represented in imaginary-time  $\tau$ . When convergence is reached, this quantity is used to compute the local spectral function via analytical continuation.

high-frequency tail of the self-energy can be expanded as:

$$\Sigma(i\omega_n) = s_0 + \frac{s_1}{i\omega_n} + \dots \quad (5.9)$$

For a purely local interaction  $U$ , one has  $s_0 = U \langle n_\sigma \rangle$ , where  $\langle n_\sigma \rangle$  is the density per spin. This is simply the Hartree-Fock self-energy. The presence of non-local interactions introduces an effective polaron problem, where the electrons are dressed by bosonic excitations. An introduction and more details to the polaron problem are given in [135]. This adds up another term in the zeroth-moment:  $s_0 = U \langle n_\sigma \rangle - 2K'(\tau=0) \times 2 \langle n_\sigma \rangle$ , where  $K$  is a function such that  $K''(\tau) = \mathcal{U}(\tau)$ . The zeroth-moment of the self-energy,  $s_0$ , can be absorbed as a shift in the chemical potential from the beginning of the self-consistent loop, speeding up convergence. This is why, in Fig. 5.5, the self-energy goes to zero at high frequency.

In the self-consistency cycle a mixing of 50% (on the self-energy and the polarisation) is used when including the Fock term. Indeed, the Hartree-Fock approximation is non-local, and is well-known to yield many local minima.

Since the impurity solver uses CTQMC, the whole EDMFT algorithm is performed in imaginary-time and imaginary-frequency. As a post-processing, analytical continuations are carried out using the Maximum Entropy algorithm in Bryan's implementation [136]. The analytical continuations transform imaginary-times observables into their corresponding spectra on the real axis.

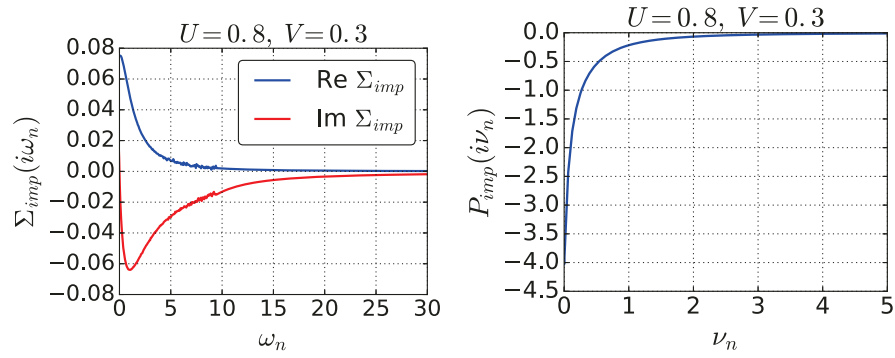


Figure 5.5: Impurities quantities. On the left-hand side, the impurity self-energy is to be used as the lattice self-energy. The real part of the self-energy is manually set to zero. It is computed via improved estimators [134]. On the right-hand side, the impurity polarisation is also to be used on the lattice. It is computed from Eq. (5.8).

# 6 Results in the high-doping regime

In Chapter 4, we have presented a realistic model for the cobaltates. In this chapter, we present the corresponding results and correlation effects in the high-doping regime. The extended Hubbard model was simulated using EDMFT, with and without the non-local Fock term. We performed low, but finite-temperature calculations, with an inverse temperature  $\beta = 100 \text{ eV}^{-1}$  (corresponding to a temperature of  $T = 116 \text{ K}$ ). In the high-doping regime, the band is almost completely filled:  $\langle n_\sigma \rangle = 0.83$ . In Chapter 4, we argued that  $U$  could be estimated to 5 eV. Here, we scan over several values of  $U$  and  $V$ , with  $U$  up to 4 eV, and  $V$  up to 0.7 eV. We do not probe higher values of  $U$  because we will show that the energy window up to 4 eV gives already a sufficient idea about the general trends of the physical observables. In this chapter, all energies are given in eV.

We perform single-site (homogeneous) paramagnetic calculations. This does not allow for symmetry breaking, either in real space or in spin space.

We first present the computed phase diagram, as a function of the local and non-local Coulomb interactions. The phase diagram displays a charge-ordering transition, due to the presence of the non-local interaction  $V$ . We then describe separately one- and two-particle observables in the homogeneous phase. We clarify the role of correlation on these two types of observables, and we argue that they can be understood as consequences of strong doping.

## 6.1 Computed phase diagram

We first present the computed phase diagram (see Fig. 6.1) of the triangular lattice, for which we describe each phase separately. Calculations are performed in EDMFT, with and without the non-local Fock term. Whether or not the Fock term is included does not qualitatively change the phase diagram, but rather shifts the boundaries between the phases.

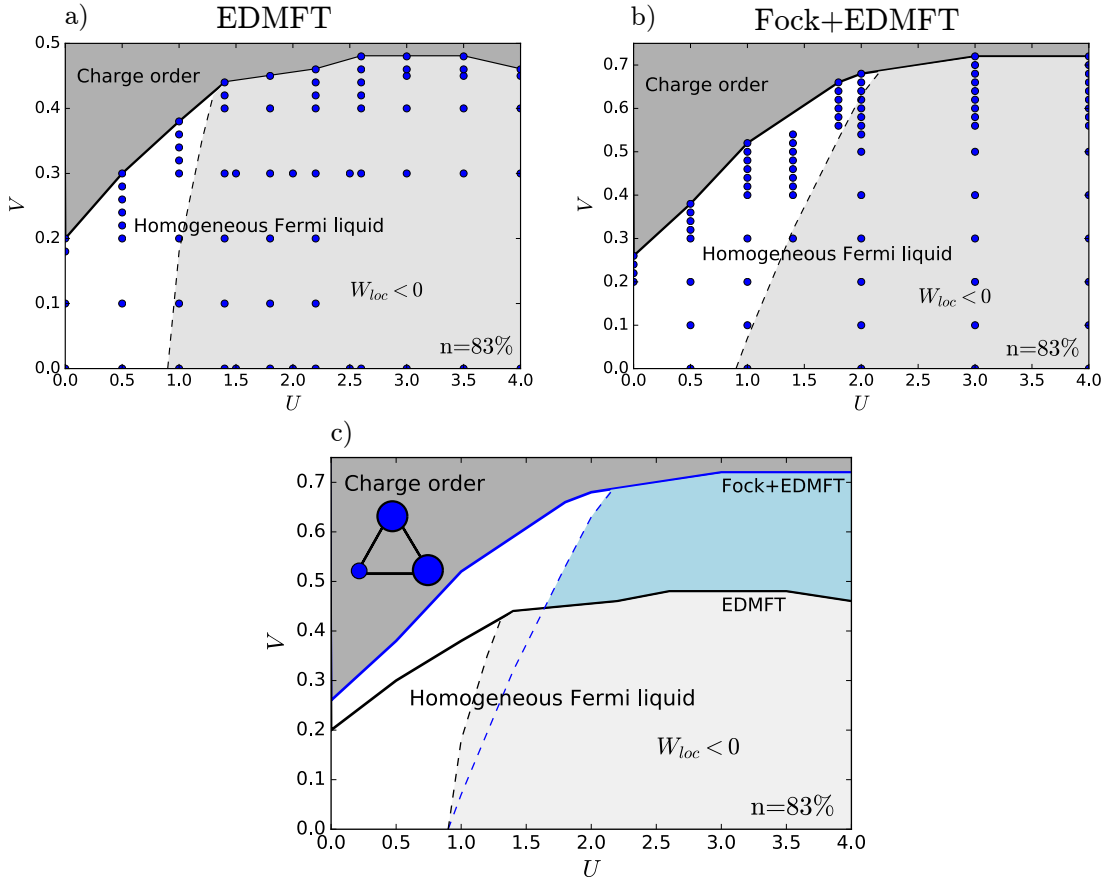


Figure 6.1: The computed phase diagram of the extended Hubbard model on a triangular lattice, at filling  $\langle n_\sigma \rangle = 0.83$ , and inverse temperature  $\beta = 100$  for the paramagnetic case, assuming a homogeneous solution. a) EDMFT phase diagram. Blue dots are computed points. b) EDMFT with the non-local Fock term. c) Comparison between the two previous phase diagrams, a) and b). These phase diagrams are qualitatively similar as they display the same phases. They display a phase transition, between an homogeneous Fermi-liquid phase (at low  $V$ ) and a charge-order phase (at high  $V$ , dark grey). The speculated charge-ordering pattern is depicted in the inset of c). The blue spheres represent cobalt atoms, and their local charges (either 1 or 2) are symbolised by the sizes of the spheres. The homogeneous Fermi-liquid phase is further divided into a positive static screening region (at low  $U$ , white), and a negative static screening region (at high  $U$ , light grey / blue).

This phase diagram displays two phases: a metallic homogeneous phase at low intersite interaction  $V$ , and a charge-ordered phase at high  $V$ .

#### *The homogeneous metallic phase*

At small intersite interaction  $V$ , the system is in a homogeneous Fermi-liquid phase.

Quasi-particles are well-defined and show itinerant behaviour. The Fermi-liquid behaviour will be checked in the next section, upon analysis of the self-energies. The high filling value prevents a Mott metal-insulator transition up to large values of  $U$ . Indeed, there are very few charge carriers in the system (in this case, few holes). This highly limits the possibility for particles to scatter against each other, and to lose coherence. Phrased differently, within this dilute regime, two holes have a very low probability to sit on the same lattice site.

This Fermi-liquid phase is further divided into two sub-regions, depending on the value of the computed local static screened interaction,  $W_{\text{loc}}(\omega = 0)$  (see dotted line and shaded region in Fig. 6.1). For low values of  $U$ , the local static screening is found to be positive:  $W_{\text{loc}}(\omega = 0) > 0$ . However, for higher values of  $U$ , the local static screening is found to be negative:  $W_{\text{loc}}(\omega = 0) < 0$ . The fact that the screened interaction can become negative is surprising at first sight. This means that the effective interaction between two classical particles is attractive. More details about two-particle quantities will be provided in Sec. 6.3.

### *The second-order transition line*

The Fermi-liquid phase is separated from a charge-ordered phase, for high values of the intersite interaction  $V$ . In this region of parameter space, calculations within homogeneous (Fock +) EDMFT could not be converged. The separation line in Fig. 6.1 corresponds to the set of last-converged points. More specifically, the separation line between the two phases can be monitored by the static lattice susceptibility  $\chi(\mathbf{q}, \omega = 0)$ . When increasing  $V$ , the static lattice susceptibility starts diverging at some ordering vector, meaning that the transition is of second-order. The lattice susceptibility is linked to the bosonic propagator on the lattice:  $W(\mathbf{q}, \omega) = v_{\mathbf{q}} - v_{\mathbf{q}}\chi(\mathbf{q}, \omega)W(\mathbf{q}, \omega)$ . Inserting the Dyson equation for the bosonic propagator, the EDMFT lattice susceptibility is given by:

$$\chi(\mathbf{q}, \omega) = -\frac{P_{\text{imp}}(\omega)}{1 - v_{\mathbf{q}}P_{\text{imp}}(\omega)}. \quad (6.1)$$

By definition of EDMFT, the polarisation is a purely local quantity, and the  $\mathbf{q}$ -dependence on the right-hand side of Eq. (6.1) is only present in the Fourier-transform of the interaction,  $v_{\mathbf{q}}$ , as given by Eq. (4.4). In particular, within our model, the divergence of the static susceptibility  $\chi(\mathbf{q}, \omega = 0)$ , which is equivalent to  $1 - v_{\mathbf{q}}P_{\text{imp}}(\omega = 0) = 0$ , always sets in at the ordering vector  $\mathbf{q} = K$  (see Fig. 4.1 and Fig. 6.2). In Fig. 6.2, we show the behaviour of  $1 - v_{\mathbf{q}}P_{\text{imp}}(\omega = 0)$  in the vicinity of the transition line. In physical terms,  $1 - v_{\mathbf{q}}P_{\text{imp}}(\omega = 0)$  corresponds to the static dielectric function of the system.

The divergence condition for the susceptibility, Eq. (6.1) is equivalent to  $1 - v_{\mathbf{q}}P_{\text{imp}}(i\omega) = 0$ , i.e., the static dielectric function goes to 0. This line is of similar nature as the so-called Wigner-Mott transition, previously studied on the square lattice [109, 137, 138]. The

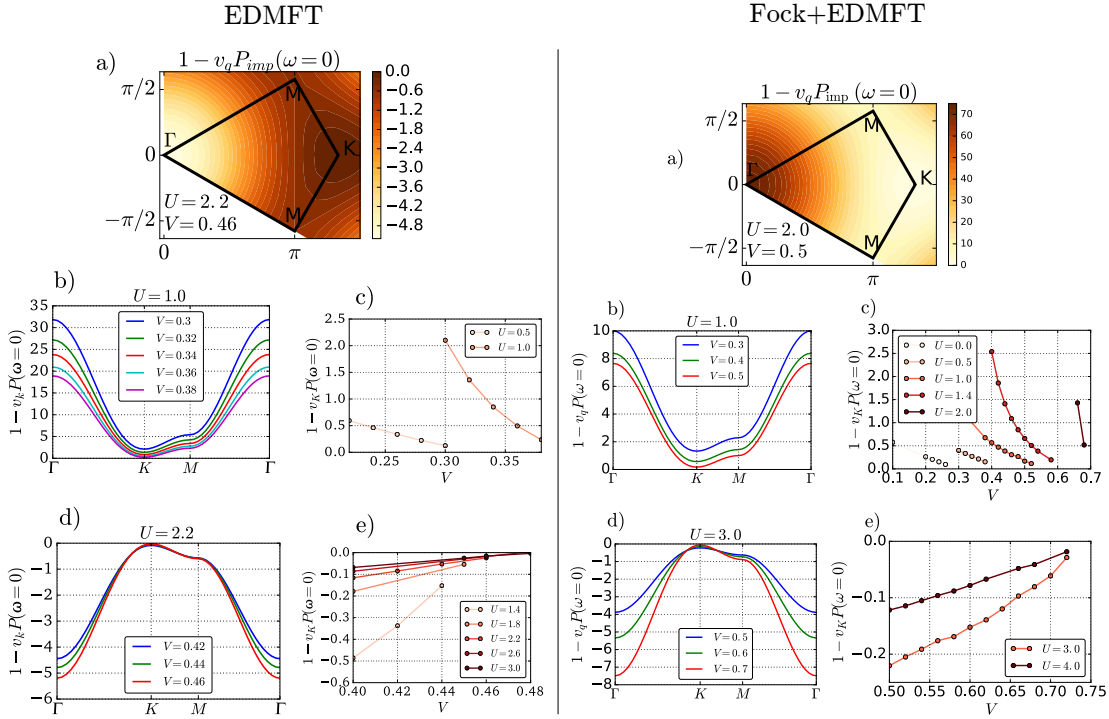


Figure 6.2: Analysis of the transition line. Left side: EDMFT result. Right side: Fock + EDMFT. a) The static value of the dielectric function,  $\epsilon(\mathbf{q}, \omega = 0) = 1 - v_q P_{\text{imp}}(\omega = 0)$  in the irreducible Brillouin zone of the triangular lattice, for  $U = 2.2$  eV,  $V = 0.46$  eV,  $\beta = 100$  eV $^{-1}$ . The high-symmetry points  $\Gamma$ ,  $K$  and  $M$  are represented. The  $\mathbf{q}$ -point where  $1 - v_q P_{\text{imp}}(\omega = 0)$  goes to 0 is the point where the divergence of the static susceptibility,  $\chi(\mathbf{q}, \omega = 0)$ , sets in. For our specific model, the divergence always sets in for  $\mathbf{q} = K$ . b) and d) The static value of the dielectric function  $1 - v_k P_{\text{imp}}$  on a  $q$ -point path. Note the sign change of the dielectric function with respect to  $U$ . The sign of the dielectric function is directly connected to the sign of  $W_{\text{loc}}$ , as shown in the phase diagram in Fig. 6.1. c) and e) The value of the static dielectric function at the ordering vector  $\mathbf{q} = K$ , for various values of  $U$ .

static dielectric function is monitored in Fig. 6.2 in the vicinity of the charge-ordering transition. In particular, on top of going to zero at the phase transition, the static dielectric function changes sign depending on the region of the phase diagram (see shaded region in Fig. 6.1, denoting negative static local screening).

### Nature of the ordered phase

The ordered phase, at larger  $V$ , cannot be accessed via homogeneous single-site EDMFT, because of the symmetry breaking. However, at the specific filling  $0.833 = \frac{1}{2} + \frac{1}{3}$ , we expect a  $\sqrt{3} \times \sqrt{3}$  superstructure, commensurate to the filling level, with 3 atoms per supercell: 2 atoms are completely filled, and one atom retains one electron (see Fig. 6.1). The electrons rearrange in order to minimise the nearest-neighbour repulsion. This is in

line with previous studies, that find a static ordering at commensurate fillings [118].

### *Difference between EDMFT and Fock+EDMFT*

Upon addition of the Fock term, the charge-order transition line is pushed up in  $V$ . This is linked to a decrease in  $\chi(\omega = 0)$ , connected to a decrease in the renormalised density of states at the Fermi level,  $N(\epsilon_F)$ , as will be explained in section 6.3.

In the rest of this study, we analyse the homogeneous Fermi-liquid phase. We give a description of correlation effects by analysing single-particle observables in section 6.2 and two-particle observables in section 6.3.

## 6.2 One-particle observables

In this section, we describe the single-particle observables within (Fock +) EDMFT, in the Fermi-liquid phase. We argue that they are typical of a (moderately) correlated system, as they feature a lower Hubbard correlation band.

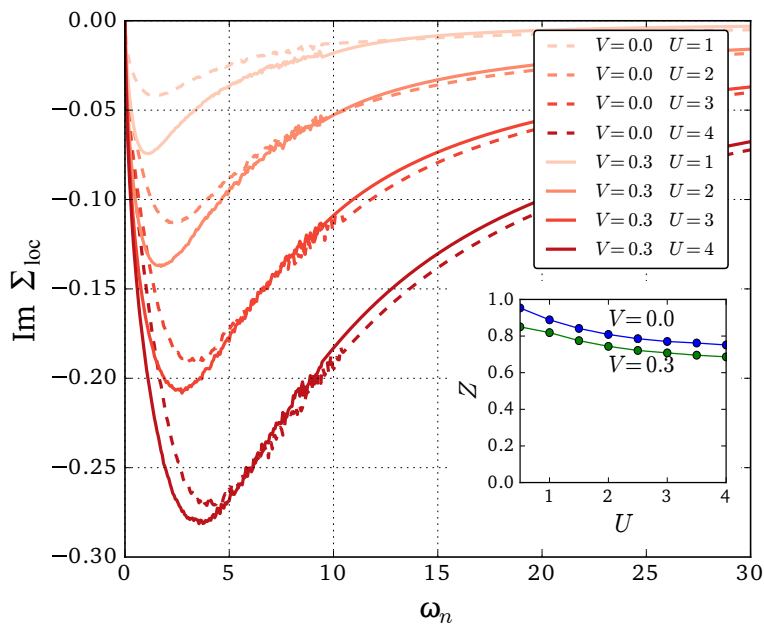


Figure 6.3: The imaginary part of the local self-energy on the Matsubara axis,  $\text{Im } \Sigma(i\omega_n)$ , and the corresponding quasi-particle renormalisation factors,  $Z$ . The numerical values are typically those of a moderately correlated system. Correlations increase when either  $U$ , the on-site interaction, or  $V$ , the nearest-neighbour interaction, increases.

The self-energies on the Matsubara axis are depicted in Fig. 6.3, for various values of  $U$  and  $V$ . These self-energies are all metallic. The imaginary part of the self-energy goes linearly to zero at  $\omega = 0$ , following a Fermi-liquid behaviour, even for high values of

the Hubbard interaction  $U$ . A Mott metal-insulator transition is thus prevented by the strong doping. Correlations increase when either  $U$  or  $V$  increases, as can be seen from the quasi-particle renormalisation factors in Fig. 6.3. The quasi-particle renormalisation factor  $Z$  is defined as:

$$Z = \frac{1}{1 - \left. \frac{\partial \Sigma(i\omega)}{\partial(i\omega)} \right|_{\omega=0}}. \quad (6.2)$$

The values of the renormalisation factor are typical of (weakly) correlated regimes, even at strong local interaction  $U$ . The quasi-particle renormalisation factor describes how much spectral weight is removed from the quasi-particle peak, towards high-energy tails, due to electronic correlations. For a non-interacting system, the quasi-particle renormalisation factor is  $Z = 1$ . It is worth noting that correlations increase when the nearest-neighbour interaction  $V$  increases. This trend contrasts with what was observed for the half-filled extended Hubbard model on a square lattice, where correlations decrease when  $V$  increase [99]. It was argued that the intersite interaction  $V$  effectively reduces the on-site interaction  $U$  to the screened value  $U_{\text{eff}} = \mathcal{U}(i\nu_n = 0)$ . In our case, the effect of  $V$  is to enhance correlation by introducing more interaction channels, thus suppressing certain hopping paths.

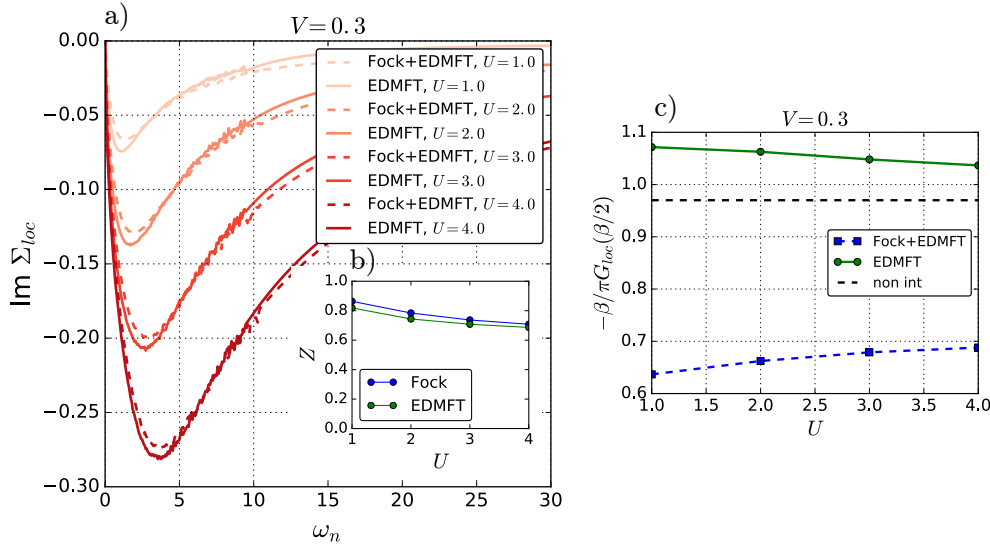


Figure 6.4: One-particle quantities with Fock+EDMFT, compared to EDMFT. a) Imaginary part of the self-energy on the Matsubara axis. b) Renormalisation factors. c) Density of states at the Fermi level, computed as  $N(\epsilon_F) = -\frac{\beta}{\pi} G_{\text{loc}}(\frac{\beta}{2})$ .

Fig. 6.4 shows the effect of the non-local Fock term on several single-particle quantities. One observes that for self-energies and renormalisation factors, adding a Fock non-local term does not change the result significantly. The densities of states (DOS) at the Fermi level, estimated as  $N(\epsilon_F) \approx -\beta/\pi G_{\text{loc}}(\beta/2)$ , are different, however. This is an effect of

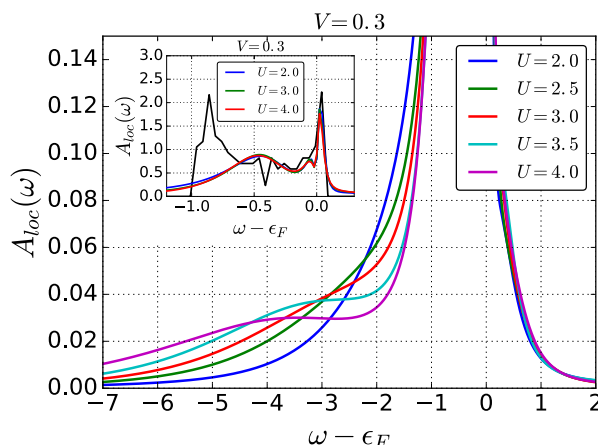


Figure 6.5: Analytically-continued local spectral functions in EDMFT, displayed in different scales. In the inset, the black curve corresponds to the non-interacting density of states, as already displayed in Fig. 4.1 d). The corresponding non-interacting bandwidth is thus about 1.1 eV. The renormalisation of the quasi-particle is visible on the quasi-particle width, and on the position of one of the van Hove peaks, displaced from approximately -0.8 eV to approximately -0.5 eV. The main panel shows again the quasi-particle peak (about 1 eV wide), together with a broad lower Hubbard band at high  $U$ .

the reduction of the effective non-interaction density of states when going from EDMFT to Fock + EDMFT (see Fig. 4.1 and the stretching of the effective non-interacting band).

Fig. 6.5 shows local spectral functions, in EDMFT, defined as  $A_{loc}(\omega) = -\frac{1}{\pi} \text{Im} G_{loc}(\omega)$ , and obtained via analytical continuation to the real-frequency axis using the maximum-entropy algorithm. In the inset, the spectra are represented on top of the non-interacting density of states. The quasi-particle peak is visible, with the two van Hove singularities in the DOS. As can be expected from the values of  $Z$ , and since the self-energy is local, the interacting bandwidth is reduced. On the main figure, the same spectra are zoomed in, to highlight a lower Hubbard band for high values of  $U$ . There is no upper Hubbard band. We interpret this asymmetry in the spectral function as a consequence of the strong doping level. Indeed, if one imagines a finite but large system, completely filled except for one hole, then the photoemission spectrum is going to be very asymmetric. On the one hand, hole-removal (or, equivalently, electron-addition) energies exactly correspond to the non-interacting ones, hence the absence of upper Hubbard band. On the other hand, hole-addition (or, equivalently, electron-removal) energies have to take into account the interaction between two holes, hence creating a lower Hubbard band.

In this section, we have shown that the system remains metallic, even for high values of  $U$ . In EDMFT, a lower Hubbard band develops as a signature of correlations. The spectral function is asymmetric between removal and addition sectors, as a consequence of strong doping.

### 6.3 Two-particle observables

In this section, we describe two-particle quantities, that account for neutral charge excitations, in the homogeneous Fermi-liquid phase of the phase diagram 6.1. We do not account for spin excitations, with a Hubbard-Stratonovitch decoupling acting only on the charge degrees of freedom. We argue that the two-particle observables are typical of a dilute system, with few charge carriers. They appear uncorrelated, as they do not retain traces of the Hubbard satellite present in the single-particle quantities. We first describe the impurity susceptibility, and then we focus on the other two-particle quantities.

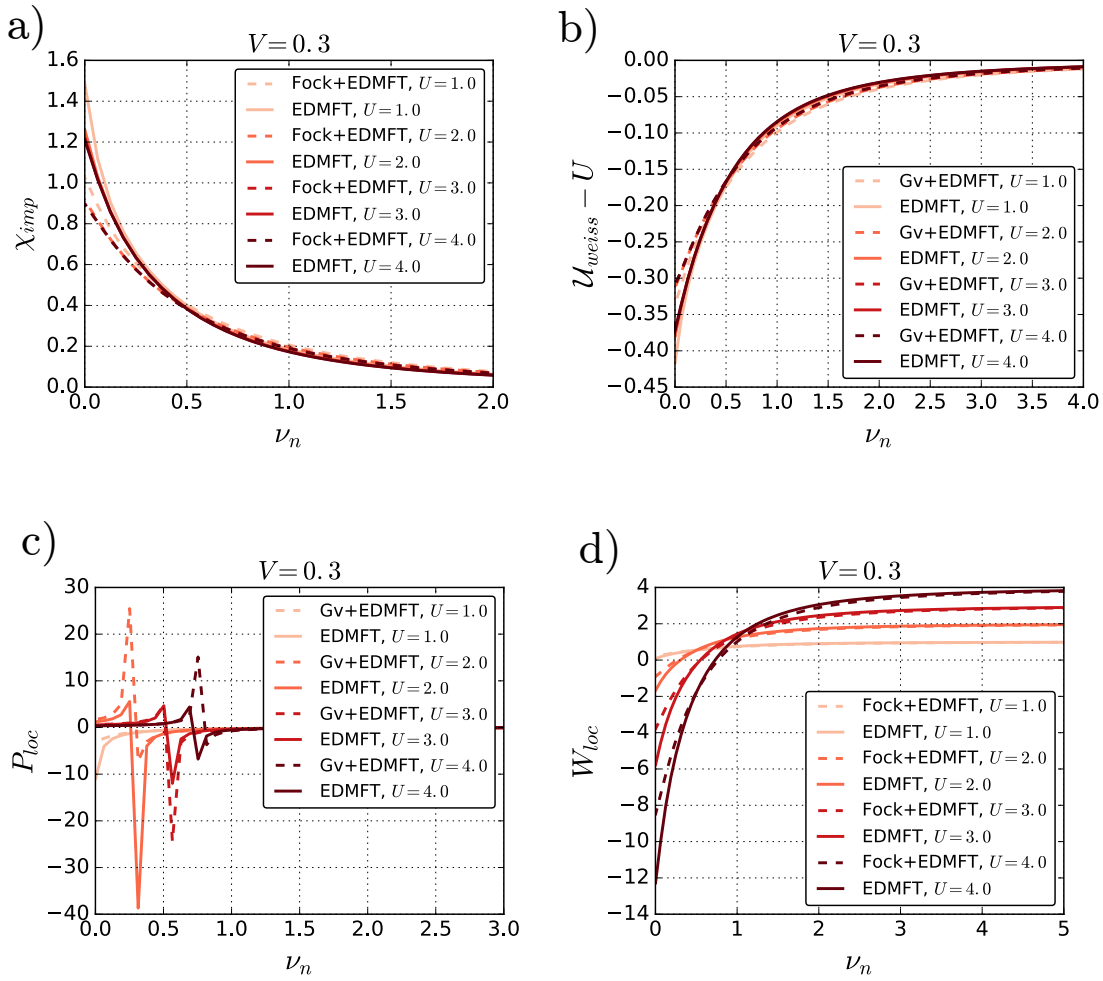


Figure 6.6: Two-particle single-site dynamical quantities within Fock+EDMFT, compared to EDMFT, on the Matsubara axis. a) The impurity susceptibility. b) The dynamical interaction. c) The impurity polarisation. d) The local screened interaction. From EDMFT to Fock + EDMFT, the most significant difference concerns the impurity susceptibility.

### 6.3.1 The impurity susceptibility

In this subsection, we describe the susceptibility as computed by solving the Anderson impurity model. Another, different choice can be to describe the local part of the lattice susceptibility. We choose to study the impurity susceptibility because it is a directly accessible quantity, since it is computed by the CTQMC solver, without resorting to approximations [139]. The impurity susceptibility is a single-site, dynamical quantity, and it is computed in imaginary time as  $\chi_{\text{imp}}(\tau) = \langle \mathcal{T}n(\tau)n(0) \rangle - \langle n \rangle^2$ . In particular, the impurity susceptibility is positive in Matsubara frequencies. The impurity susceptibility, represented in Fig. 6.6, is only moderately renormalised by correlations. This is particularly true at high values of  $U$ , where all the susceptibility curves fall on top of each other. This weak renormalisation by correlations can be traced back by analysing

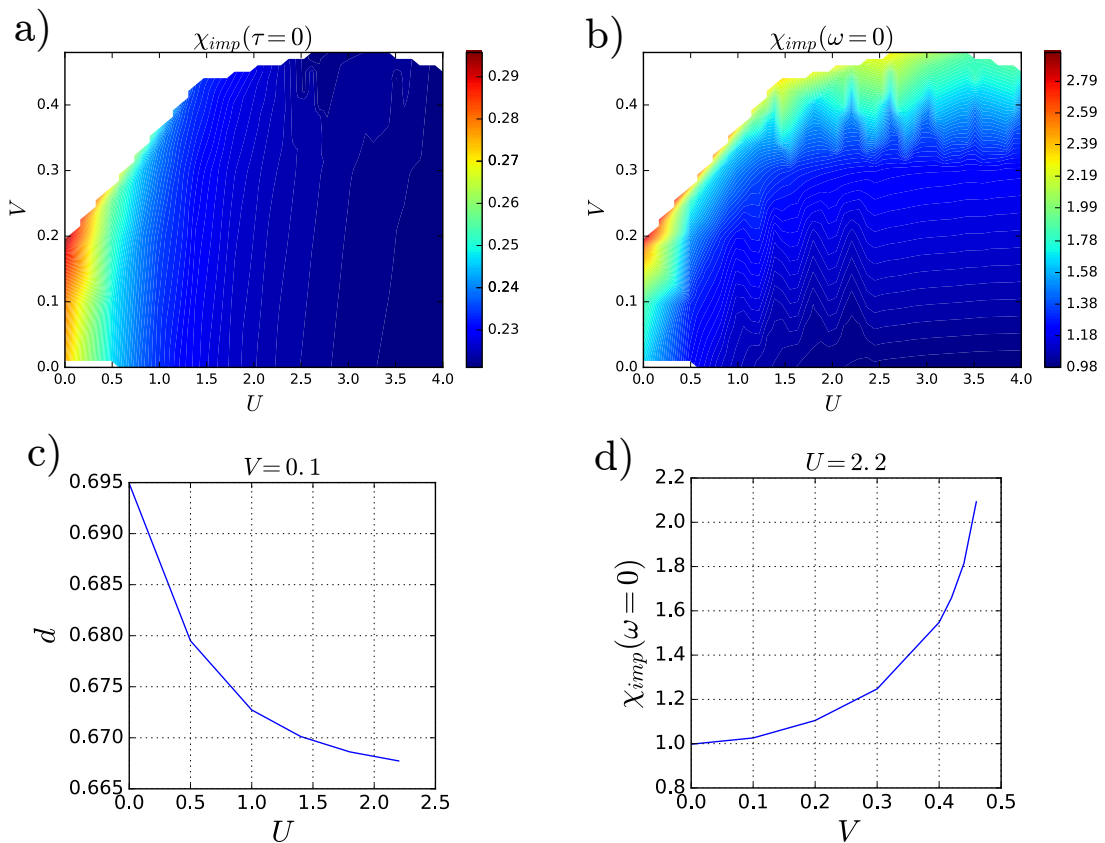


Figure 6.7: Analysis of  $\chi_{\text{imp}}$  in EDMFT. a)  $\chi_{\text{imp}}(\tau = 0)$  is directly connected to the double-occupancy. As can be expected, the double-occupancy decreases when  $U$  increases. b)  $\chi_{\text{imp}}(\omega = 0)$  signals a second-order instability at the phase boundary. c) Double-occupancy as a function of  $U$ . d)  $\chi_{\text{imp}}(\omega = 0)$  as a function of  $V$ .

two components of the susceptibility: the frequency-integrated value  $\chi_{\text{imp}}(\tau = 0)$ , and the static value  $\chi_{\text{imp}}(\omega = 0)$ , both represented in Fig. 6.7, spanning various parameter

sets throughout the phase diagram.  $\chi(\tau = 0)$  (the area under the curve  $\chi(i\omega)$ ) is linked to the double-occupancy on the impurity,  $d$ , via:

$$d = \frac{1}{2} \left( \chi_{\text{imp}}(\tau = 0) + \langle n_{\uparrow} + n_{\downarrow} \rangle^2 - \langle n_{\uparrow} + n_{\downarrow} \rangle \right). \quad (6.3)$$

The double-occupancy goes from a non-interacting value (0.83\*0.83) at low  $U$  (the equivalent of 0.25 at half-filling), to an interacting value  $1*(1.667-1)$  at high  $U$  (the equivalent of 0 at half-filling). However, due to the filling constraint, these two values are numerically close.  $\chi(\omega = 0)$  is also represented. It becomes maximum at the charge-ordering transition line, indicating a second-order instability.

The impurity susceptibility is thus weakly renormalised by the local interaction  $U$ . In fact, in EDMFT, the susceptibility is close to its non-interacting counterpart. Let us define the local non-interacting lattice susceptibility,  $\chi_{ii}^0(\tau) = 2G_{ii}^0(\tau)G_{ii}^0(\beta - \tau)$ , where  $G_{ii}^0$  is the local lattice non-interacting Green's function. More specifically, the non-interacting lattice susceptibility is computed in reciprocal space via the Lindhard formula:

$$\chi^0(\mathbf{q}, z) = \frac{1}{N} \sum_{\mathbf{k}} \frac{n_F(\epsilon_{\mathbf{k}+\mathbf{q}}) - n_F(\epsilon_{\mathbf{k}})}{z - (\epsilon_{\mathbf{k}+\mathbf{q}} - \epsilon_{\mathbf{k}})}, \quad (6.4)$$

where  $n_F$  is the Fermi-Dirac distribution function. On the real axis, one takes  $z = \omega + i\eta$ ,  $\eta = 0^+$ ; on the imaginary axis  $z = i\nu_n$ . The RPA susceptibility is also computed, via the formula:

$$\chi^{\text{RPA}}(\mathbf{q}, z) = \frac{\chi^0(\mathbf{q}, z)}{1 - v_{\mathbf{q}}\chi^0(\mathbf{q}, z)}. \quad (6.5)$$

One can measure the level of renormalisation by correlations by comparing, in Fig. 6.8: the interacting impurity susceptibility, the local non-interacting lattice susceptibility  $\chi^0$ , and the RPA susceptibility  $\chi_{\text{RPA}}$ . Both the impurity susceptibility and the non-interacting susceptibility are numerically close to each other. A comparison is also presented with a bubble composed of interacting Green's functions,  $2G_{\text{imp}}G_{\text{imp}}$ , and at the impurity level with  $2\mathcal{G}_0\mathcal{G}_0$ . All these quantities are numerically close. This contrasts with the RPA susceptibility, which is much renormalised by interactions.

This observation for  $\chi_{\text{imp}}$  can be interpreted in light of the time-dependent density-functional theory (TDDFT) [140, 93]. Let us introduce a TDDFT-like Dyson formula for the impurity susceptibility:

$$\chi(\omega) = \chi_0(\omega) - \chi_0(\omega)(\mathcal{U}(\omega) + \tilde{f}_{xc}(\omega))\chi(\omega), \quad (6.6)$$

where  $\tilde{f}_{xc}$  is equivalent to an exchange-correlation kernel. The Dyson equation, Eq. 6.6, is in principle exact, and can be seen as a definition of the exchange-correlation kernel. The exchange-correlation kernel contains self-interaction corrections. In the random-phase approximation (RPA), each quasi-particle interacts with a mean field (i.e., including

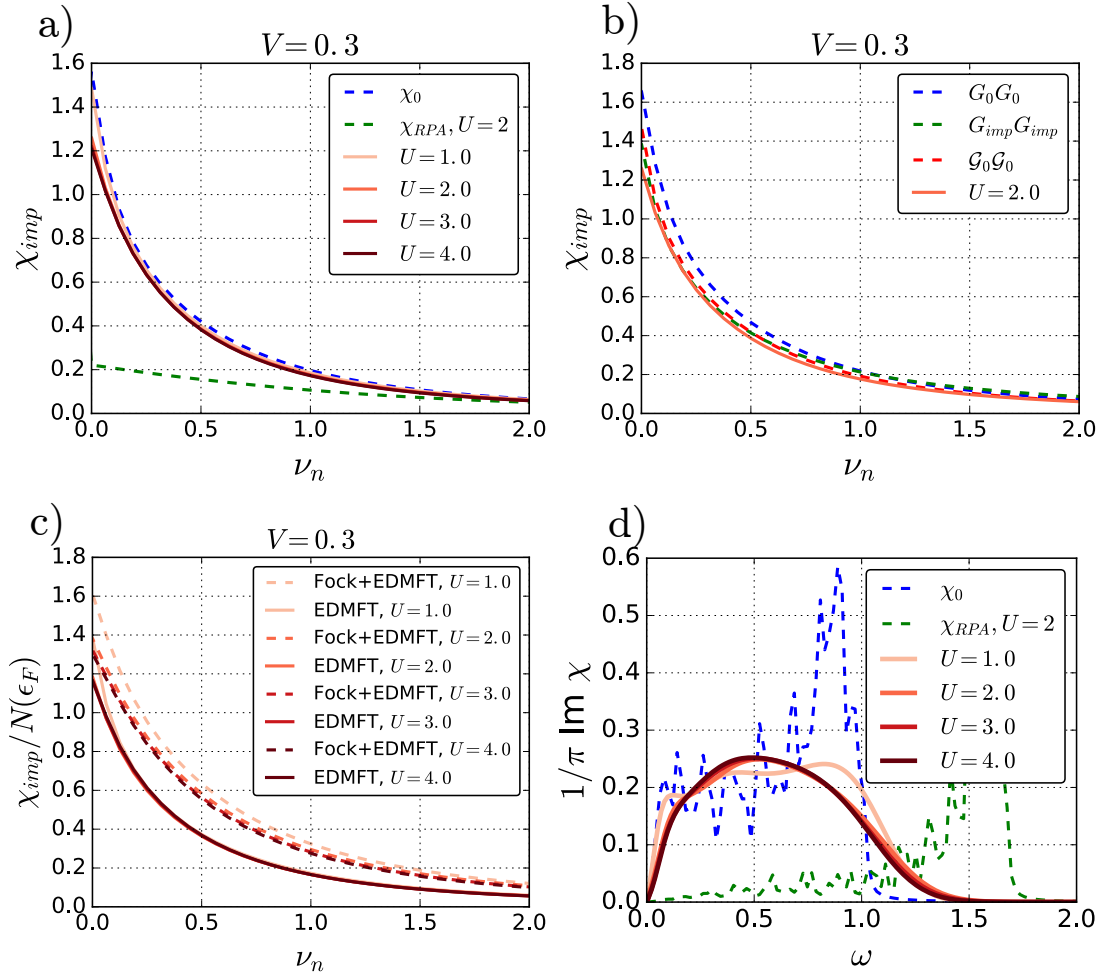


Figure 6.8: Analysis of  $\chi_{\text{imp}}$ . a) EDMFT impurity susceptibilities, compared to local parts of the lattice non-interacting susceptibility,  $\chi_0$ , and the RPA susceptibility,  $\chi_{\text{RPA}}$ . The computed impurity susceptibility is close to its non-interacting counterpart,  $\chi_0$ . b) EDMFT impurity susceptibilities compared to various bubble terms. c) Comparison between Fock and EDMFT, both renormalised by an effective DOS at the Fermi level,  $N(\epsilon_F)$ . d) Analytical continuation of the EDMFT susceptibility, compared to  $\chi_0$  and  $\chi_{\text{RPA}}$ , both directly computed on the real axis.  $\chi_{\text{imp}}$  has no trace of the Hubbard satellite present in the Green's function, and is again close to its non-interacting counterpart,  $\chi_0$ .  $\chi_{\text{RPA}}$  is strongly renormalised at low energies; it features a satellite at higher energies.

the quasi-particle itself), and self-interaction corrections are neglected, such that the exchange-correlation kernel is set to zero:  $\tilde{f}_{xc} = 0$ . The RPA is generally believed to be a suitable approximation for weakly-correlated systems. In EDMFT, however, we find that  $\tilde{f}_{xc} \approx -U$ , such that  $\chi \approx \chi_0$ , and self-interaction corrections exactly compensate the effect of interactions. The susceptibility is weakly renormalised by correlations. A priori, this result could be an artefact of the EDMFT approximation. However, in TDDFT, the

equality  $f_{xc} = -v(\mathbf{q})$  is exact in a finite system with exactly one particle [8]. Indeed, in a system with exactly one charge carrier, the energies for neutral excitations (excitations where the particle number does not change) exactly correspond to the non-interacting energies. Hence, the equality  $\chi = \chi^0$  is a signature of a dilute system, with very few charge carriers.

The effect of the Fock term on the susceptibilities can be seen in Fig. 6.6. The Fock+EDMFT susceptibilities are significantly smaller than the EDMFT ones. Indeed, we saw that the non-local Fock self-energy effectively stretches the non-interacting band. This means, in particular, that  $N(\epsilon_F)$  decreases, which leads to a decrease in  $\chi$ . In Fig. 6.8,  $\chi/N(\epsilon_F)$  is represented, for both EDMFT and Fock+EDMFT.  $N(\epsilon_F)$  is estimated from the formula  $-\beta/\pi G_{\text{loc}}(\beta/2)$ , as in Fig. 6.4. Hence, the renormalisation of the susceptibility upon addition of the Fock term can be traced back to the diminishing of the density of states at the Fermi level. This is not true any more in systems where correlations play a more significant role on two-particle observables, such as the half-filled extended Hubbard model on a square lattice [141]. In Fock + EDMFT, the impurity susceptibility is thus lower than the EDMFT one, and thus more significantly different from the local non-interacting lattice susceptibility. With the addition of the non-local Fock self-energy, the result is further away from the limit  $\chi \approx \chi_0$ , where  $\chi_0$  is the bare (non-interacting) susceptibility. It is an open question whether the inclusion of the non-local Fock self-energy improves the computation of two-particle observables in the highly-doped limit.

Finally, we show analytical continuations of the EDMFT impurity susceptibility. The spectra retain the shape expected from the non-interacting density of states. There is no sign of the Hubbard satellite, which was present in the single-particle spectra. This is in line with the fact that in a dilute system, neutral excitations (with fixed particle number) correspond to non-interacting excitations. Thus, in a dilute system, no correlation satellite is expected.

Thus, the physical observable,  $\chi_{\text{imp}}$ , which is a charge-charge correlator, can be understood as being weakly renormalised by correlations, consistent with the strong doping level. On the lattice, there are also few charge carriers (one hole per 3 lattice sites), such that this qualitative behaviour is expected to hold as well.

### **6.3.2 Auxiliary quantities: polarisation, screened Coulomb interaction and dynamical bare interaction**

We turn to the analysis of auxiliary quantities of the (Fock+) EDMFT scheme. In the previous section, we saw that the impurity susceptibility is weakly renormalised by correlations. We hence make the simplifying assumption that  $\chi_{\text{imp}}$  is constant through the whole phase diagram, and that  $\chi_{\text{imp}} = \chi^0$ . We will show that the qualitative behaviour

of all auxiliary quantities can be well understood in terms of this simplifying assumption.

The frequency-dependent interaction,  $\mathcal{U}(i\nu_n)$ , is represented in Fig. 6.6. The frequency-dependent interaction is a partially screened interaction. It effectively mimics the non-local interaction  $v_{\mathbf{k}}$  through frequency-dependence. Here, we show that this partial screening is induced by the non-local interaction  $V$ , and does not depend on the local  $U$ . At high imaginary frequencies,  $\mathcal{U}(i\nu_n)$  goes to  $U$ : the effective interaction goes to its unscreened value  $U$ , because screening processes occur only on a finite energy range. At zero-frequency,  $\mathcal{U}(i\nu_n = 0) = U_{\text{eff}} < U$  goes to a fully screened static value. Now, let us decompose the effects of  $U$  and  $V$  on screening, and define  $\tilde{\mathcal{U}}(i\nu_n) = \mathcal{U}(i\nu_n) - U$ . Fig. 6.6 shows that  $\tilde{\mathcal{U}}$  is clearly independent of  $U$ :  $\tilde{\mathcal{U}} = \tilde{\mathcal{U}}[V, \chi_0]$ . Thus, the screening depends only on  $V$  and on the band structure, but not on the local interaction  $U$ .

In particular, this dependency for  $\tilde{\mathcal{U}}(\omega)$  has an implication on the (Fock +) EDMFT lattice susceptibility. Indeed, let us further decompose  $v_{\mathbf{k}} = U + \Delta v_{\mathbf{k}}$ , such that  $\Delta v_{\mathbf{k}}$  depends only on the intersite interaction  $V$ . Assuming that  $\chi_{\text{imp}} = \chi_0$ , the EDMFT susceptibility, Eq. 6.1, can be re-expressed as:

$$\chi^{\text{EDMFT}}(\mathbf{k}, \omega) = \frac{\chi_0}{1 - \tilde{\mathcal{U}}\chi_0 + \Delta v_{\mathbf{k}}\chi_0}, \quad (6.7)$$

i.e., the EDMFT susceptibility is independent of  $U$ .

Finally, we comment on the region characterised by a negative static screened interaction. As already mentioned in section 6.1, in the phase diagram, Fig. 6.1, the Fermi-liquid phase is divided into a region where the static local screening is positive,  $W_{\text{loc}}(\omega = 0) > 0$  at small  $U$ 's, and a region where the static local screening is negative,  $W_{\text{loc}}(\omega = 0) < 0$  at large  $U$ 's. The qualitative frequency-dependence of  $P_{\text{imp}}$  and  $W_{\text{imp}}$  is a direct consequence of the equality  $\chi = \chi_0$ . Indeed, assuming that  $\chi_{\text{imp}}(\omega) = \chi_0(\omega)$ ,  $P_{\text{loc}}$  and  $W_{\text{loc}}$  can be re-expressed as:

$$P_{\text{loc}} = -\frac{\chi_0}{1 - \mathcal{U}\chi_0} \quad (6.8)$$

$$W_{\text{loc}} = \sum_{\mathbf{k}} \frac{v_{\mathbf{k}}}{1 - v_{\mathbf{k}}P_{\text{imp}}} = (1 - \mathcal{U}\chi_0) \sum_{\mathbf{k}} \frac{v_{\mathbf{k}}}{1 + v_{\mathbf{k}}\chi_0}. \quad (6.9)$$

Eqs. 6.8 and 6.9 show that, depending on the value of  $1 - \mathcal{U}\chi_0$ , there is a possibility for both a pole in  $P_{\text{loc}}$  and a sign-change in  $W_{\text{loc}}$ . These quantities are represented in Fig. 6.6. For  $V = 0.3$  and  $U = 2, 3, 4$ ,  $P_{\text{loc}}$  displays a pole at finite frequency, while  $W_{\text{loc}}$  changes sign. In particular, at zero-frequency,  $W_{\text{loc}}$  takes a negative value. In principle, a negative screened interaction is either an artifact of the EDMFT approximation, or an actual feature of the system. The possibility that the local static screening is negative is not an artifact of the (Fock +) EDMFT approximation. It is a feature of any system where the susceptibility is big compared to the inverse interaction:  $\chi V > 1$  (for a specific example, see appendix C). To conclude, we have proved that both quantities,  $P_{\text{loc}}$  and

$W_{\text{loc}}$ , self-consistently adjust in such a way that the equality  $\chi_{\text{imp}} = \chi_0$  is preserved. This may create a pole in the impurity polarisation on the Matsubara axis. Importantly, this may cause the the value of the static screening to become negative, and effectively attractive.

### 6.4 Discussion

The high doping regime, with a filling close to the band edge, leads to very specific correlation effects. On the one-particle side, the local spectral function is asymmetric and displays a lower Hubbard band. On the two-particle side, however, correlation effects lead to more unusual features. The impurity susceptibility is weakly renormalised by correlations, and stays close to its non-interacting counterpart in the whole metallic phase. This weak renormalisation in turn affects the other two-particle quantities. The static screened interaction becomes negative at high  $U$ , while the polarisation displays a pole on the Matsubara axis.

We hence found a whole region of the phase diagram, characterised by a negative value of the local static screened interaction. The meaning of a negative screened interaction is not yet understood. However, it is not an artifact of the EDMFT approximation, and is a signature of high-doping coupled to strong local interactions  $U$ . Even if single-site EDMFT calculations are well-converged within this region, it could still hide a charge-ordering transition, not detectable by single-site EDMFT. This charge-ordering transition may be related to the Wigner transition of the homogeneous electron gas [142], with which it shares common ingredients: low carrier density, and high interaction strength.

This study also raises the question of how to compute  $\chi(\mathbf{q}, \omega)$  beyond EDMFT. In EDMFT, the  $\mathbf{q}$ -dependence of the lattice susceptibility is dictated by  $v_{\mathbf{q}}$ . Alternative methods to derive the  $\mathbf{q}$ -dependence of the susceptibility from a strongly-correlated perspective include computing a non-local polarisation as in  $GW + \text{DMFT}$  [103, 99], or explicitly computing a vertex as in  $\text{D}\Gamma\text{A}$  [143] or Trilex [144, 145]. It could be instructive to benchmark our computed phase diagram against these methods.

However, from a cobaltate perspective, our computed phase diagram does not display a transition towards the experimentally-observed charge-disproportionation. In principle, this can be either a matter of the model, or a matter of the approximation used to simulate this model. In the next part, we will focus more on the details of the material, to understand better the ingredients of our model.

*Ab-initio* study of strongly-doped **Part III**  
cobaltates



# 7 Electronic structure of doped CoO<sub>2</sub> planes

In Part II, we analysed an extended Hubbard model on a triangular lattice, specifically tailored to reproduce a static mean-field description of the cobaltates. The model, as well as the non-interacting parameters, were extracted from a study by Piefke *et al.* [121]. In this part, we want to take a step back, and obtain our own first-principle results for the cobaltates. This helps us understand how to build an effective low-energy model. Most importantly, this helps us understand the physical content behind a band structure. We analyse some microscopic details of the material, such as hopping processes and hybridisation with oxygen.

In Chapter 7, we analyse the band structure of CoO<sub>2</sub> planes as obtained within the Density Functional Theory. In Chapter 8, we check some physical trends: we analyse how sodium doping, crystal structure or magnetism affect the band structure. In Chapter 9, we compute susceptibilities from first principles, making connection to the results of Part II.

Our first-principles study is based on calculations using density-functional theory (DFT). DFT is in principle a ground-state theory. It can account in particular for densities and total energies. We go beyond this strict usage and use DFT results to understand the key microscopic processes at play in the cobaltates. Calculations are performed using the VASP package [146, 147]. The electronic wave functions are expressed using the projector augmented wave method (PAW, see [148, 149]). Unless stated otherwise, the DFT functional we use is the PBE (named after its inventors, Perdew, Burke and Ernzerhof) [92, 150], which is a generalised-gradient-approximation functional (GGA). We use a plane-wave energy cutoff of 600 eV. Since we are computing a metallic band structure, a smearing function is used, corresponding to a Fermi-Dirac distribution, with the smearing parameter  $\sigma = 0.01$  eV.

The structure of the cobaltates consist of a stacking of CoO<sub>2</sub> planes, between which sodium ions are intercalated. Even though for  $x = 2/3$ , experiments evidence sodium ordering, the experimental unit cell is large, which would make calculations very heavy

and the interpretation of its band structure too complicated. In Chapter 2, we argued that the sodium ions can be considered as electron donors, as well as spacers. This means that they merely give one electron to the cobalt planes, and do not participate to the most important electronic processes. This is why, in this chapter, we forget about the actual sodium ions. We use a simplified view, and describe a stacking of doped  $\text{CoO}_2$  planes.

The goal of this chapter is to obtain a physically reliable band structure for the doped  $\text{CoO}_2$  planes. This band structure gives us access to the important microscopic processes within the planes.

### 7.1 Presentation of the $\text{CoO}_2$ planes

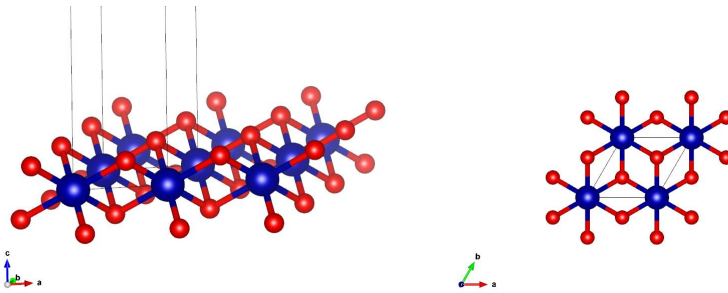


Figure 7.1: Crystal structure of the quasi-two-dimensional  $\text{CoO}_2$  planes. Left: Side view. The cobalt atoms (blue) form a triangular lattice. The oxygen atoms (red) alternate above and below the centres of cobalt triangles. Right: Top view of  $\text{CoO}_2$  planes.

As said in Part I, the  $\text{CoO}_2$  planes are the two-dimensional building blocks of the cobaltates. Their structure is illustrated in Fig. 7.1. In the plane, the cobalt atoms form a triangular lattice. Oxygen atoms are above and below the centres of the cobalt triangles. The unit cell is very simple with a unit formula  $\text{CoO}_2$ , consisting of 3 atoms. This cell will be called a minimal cell later on. To be exact, in the actual cobaltates, successive  $\text{CoO}_2$  planes are not equivalent, because of the oxygen positions. However, unless stated otherwise, we consider minimal cells in the  $aa$  stacking, with equivalent successive  $\text{CoO}_2$  planes. Calculations were performed using 32 bands per minimal cell, on a  $18 \times 18 \times 9$   $k$ -point grid.

In principle, it is possible to perform an ionic relaxation within DFT, in order to obtain atomic positions from first-principles. However, the  $\text{CoO}_2$  planes are not a true physical material, and the absence of sodium ions may render ionic relaxation problematic. Instead, the atomic positions are extracted from powder X-ray diffraction experiments by Platova *et al.*, performed at the specific doping  $x = 2/3$  [50]. These experiments give access to all the atomic positions, including the oxygen heights.

## 7.2 Effect of doping on the band structure: a rigid band shift?

In the cobaltates, the doping level of the  $\text{CoO}_2$  planes is controlled by the sodium content. In principle, accounting properly for the doping would imply to compute the entire experimental supercell, including the ordered sodium atoms. However, in this chapter, we resort to other effective techniques to compute the band structure of the doped  $\text{CoO}_2$  planes. There are several methods to compute such a doped band structure. The most naive one is to perform a calculation for the parent undoped system, and then to shift the Fermi level, in order to obtain the desired electron count. This amounts to rigidly shift the entire band structure. However, this method does not account for the electronic potential changes that come with doping. An alternative method consists of performing a DFT calculation by adding more electrons to the system and recalculating the band structure self-consistently. At each self-consistency step, the Kohn-Sham orbitals are filled up to the desired electron count. This method will be called electron-doping. The self-consistency ensures that the potential changes induced by doping are included. This electron-doping method effectively assumes a compensating uniform positive background.

The first question we want to answer is: Does electron-doping induce a significant band structure distortion, as compared to an undoped calculation?

The undoped band structure for  $\text{CoO}_2$  planes is presented on Fig. 7.2. It is possible to assign a label to each group of bands, with the labels corresponding to atomic orbitals, even though hybridisation occurs (see Fig. 7.2). The oxygen  $2s$  and  $2p$  bands are fully occupied. The cobalt  $3d$  bands are split due to the crystal field, into  $t_{2g}$  and  $e_g$  manifolds. The Fermi level is located within the  $t_{2g}$  manifold. There are 21 electrons per minimal unit cell in this undoped structure.

Now that the undoped band structure is clarified, let us superimpose it to an electron-doped one (Fig. 7.2). Electron-doping is performed by adding  $2/3$  electrons to the minimal cell, resulting in 21.6667 electrons per cell. The various band groups get shifted in a non-trivial way. Since we are predominantly interested in the low-energy bands, let us look closer at the  $p$  and  $d$  bands. Let us also shift the Fermi level of the undoped structure by  $-0.2049$  eV, in order to align the  $a_{1g}(\Gamma)$  levels of the two structures.

The  $\text{O}(2p)$  manifold is roughly located between  $-7$  eV and  $-1.5$  eV. The  $t_{2g}$  manifold lies between  $-1.3$  eV and  $0.2$  eV. The  $e_g$  manifold is above the Fermi level, between  $1.5$  and  $2.5$  eV. As a first remark, a gap opens up between the  $\text{Co}(3d)$  bands and the  $\text{O}(2p)$  bands as a result of electron-doping, marked as  $\Delta$  in Fig. 7.2. This gap can be interpreted as originating from an electrostatic repulsion occurring locally on the cobalt atoms, as such created by a local Hubbard  $U$ . An important part of this gap can be assigned to the variation of the Hartree potential induced by doping. Indeed, let us estimate the local

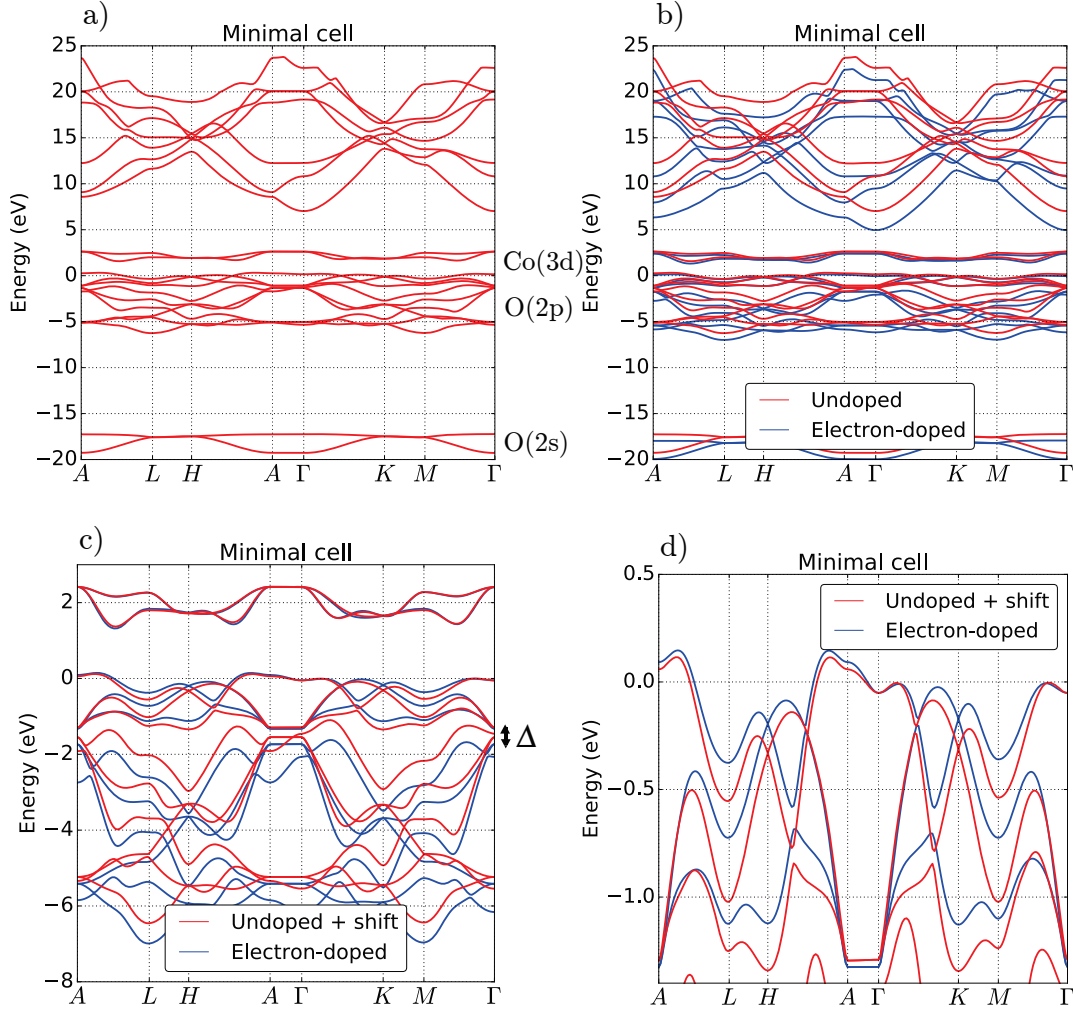


Figure 7.2: Band structures for a  $\text{CoO}_2$  plane, for different doping techniques, minimal cell. a) Undoped band structure. The various band groups can be labelled according to their main atomic character. b) Comparison between the undoped structure as in a), and an electron-doped structure.  $2/3$  electrons per minimal cell are added to the doped calculation. c) and d) A rigid shift of  $-0.2049$  eV is applied to the undoped band structure, to simulate doping. c) Comparison on an expanded scale to show the O( $2p$ ) and the Co( $3d$ ) manifolds. d) Comparison on an expanded scale to show the weakly dispersive  $t_{2g}$  manifold.

Hartree potential, created by a local  $U$ , on the cobalt states:

$$\Sigma_{\text{Co}(3d)}^H = \frac{U}{2} \langle n_{\text{Co}(3d)} \rangle. \quad (7.1)$$

This static Hartree self-energy shifts the entire Co( $3d$ ) manifold. When the filling of the

Co(3d) manifold,  $\langle n_{\text{Co}(3d)} \rangle$ , varies from 5 to 5.6667 electrons per atom upon doping, then the Hartree potential  $\Sigma_{\text{Co}(3d)}^H$  varies by  $\frac{U}{2} \times 5.6667 - \frac{U}{2} \times 5 = \frac{U}{3}$  upon doping. Of course, here we have forgotten the rearrangement of the electrons upon doping. We have also forgotten the other, non-local matrix elements, and all exchange and correlation effects. However, the opening of a gap between the oxygen and the cobalt states reminds us that there exist a sizable interaction energy arising locally on the cobalt atoms.

The second remark is that the cobalt  $t_{2g}$  bands get slightly distorted upon electron-doping. The effect of doping on the  $t_{2g}$  bands is twofold. The  $a_{1g}$  bandwidth is reduced with electron-doping, while the  $e'_g$  bandwidth is augmented.

Hence, doping induces a significant band distortion. In the next paragraph, we describe electron-doped bands.

## 7.3 Band structure of doped CoO<sub>2</sub>

### 7.3.1 The electron-doped band structure

The band structure of the electron-doped CoO<sub>2</sub> planes is presented on Fig. 7.3. It will be used as a reference for many comparisons later in this thesis.

Exactly as for the undoped case, atomic-orbital labels can be assigned to each band group. The  $t_{2g}$  bands cross the Fermi level. Among the three  $t_{2g}$  bands, one band, denoted  $a_{1g}$ , is fully symmetric, while two  $e'_g$  bands are not. The  $a_{1g}$  band corresponds to a cobalt  $d_{z^2}$  orbital, hybridised with oxygen  $p_z$  orbitals. The fat band for the  $d_{z^2}$  orbital is represented on Fig. 7.3. This fat band has been calculated by projecting the Kohn-Sham states onto atomic orbitals on spheres centered around the cobalt atoms, with a radius of 1.302 Å. In particular, only the  $a_{1g}$  band crosses the Fermi level. This fact contrasts with previous *ab-initio* studies [53, 52], and will be explored more in the next chapter.

### 7.3.2 Comparison to the model non-interacting band

In Part II, we used a single-band model for the cobaltates. The non-interacting band corresponds to the symmetric  $a_{1g}$  band, which is the only band crossing the Fermi level in our study. We can now compare the model non-interacting band to our first-principle calculations. The comparison is displayed on Fig. 7.3d). We see that there is qualitative agreement between the model and the *ab-initio* bands. In the model, the  $a_{1g}$  band was parametrised by hopping parameters acting on a two-dimensional lattice. By construction, the two-dimensional model does not include dispersion along  $k_z$ . In the *ab-initio* calculation however, the dispersion is slightly modulated along  $k_z$ . Also, the model non-interacting bandwidth is smaller than its *ab-initio* counterpart. This can be

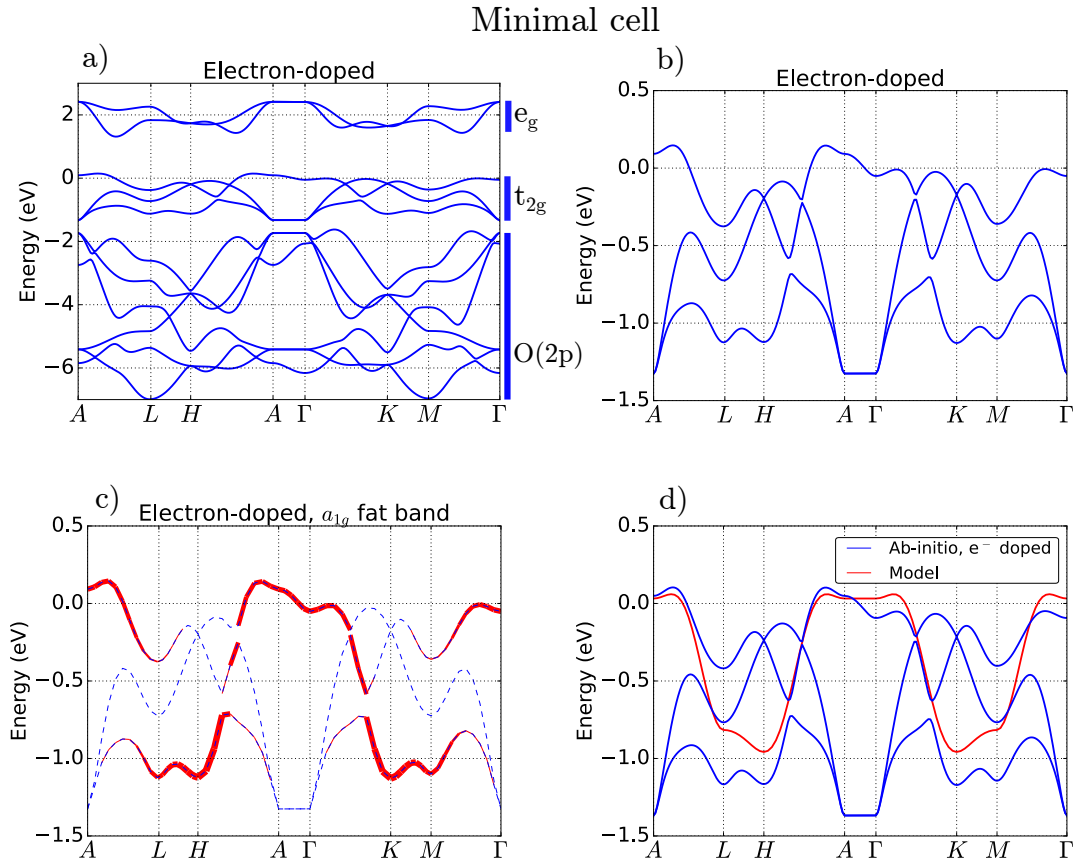


Figure 7.3: Band structures for  $\text{CoO}_2$  planes, minimal cell, doping with electrons. a) and b) Figures on expanded scales to show the low-energy bands. Oxygen  $2p$ ,  $t_{2g}$  and  $e_g$  bands are well separated between each other. From Fig b), there is only one type of Fermi-level crossing. c) Fat band for  $a_{1g}$ , the only band crossing the Fermi level. It was the band used to design the non-interacting model in Part II. d) Comparison between the electron-doped *ab-initio* band structure, and the non-interacting band of the model. The model is purely two-dimensional, so there is no dispersion along the  $k_z$  direction.

ascribed to the fact that the model band was extracted from calculations using explicit sodium ions. This sodium ions localise the electrons, as will be discussed later, resulting in a reduced bandwidth.

### 7.3.3 Orbital-projected density of states

From the band structure, it is possible to extract a density of states. Here, the Kohn-Sham eigenstates are projected onto atomic orbitals. The definition of this projection depends on a radius around each atom. The radii are  $1.302 \text{ \AA}$  for cobalt and  $0.820 \text{ \AA}$  for oxygen. The orbital-projected density of states is presented in Fig. 7.4. As in the band structure,

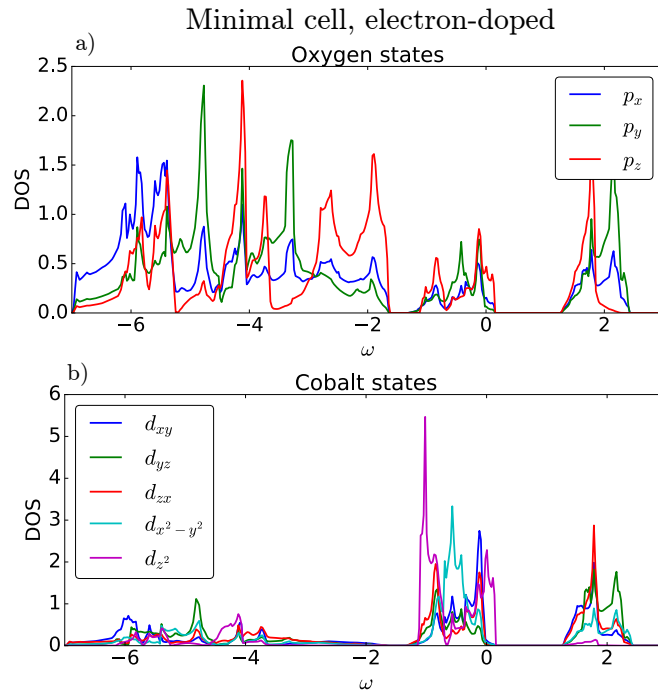


Figure 7.4: Orbital-projected densities of states. Top: Projection on oxygen orbitals. Bottom: Projection on cobalt orbitals.

we recognise three sets of bands. First, the oxygen-derived  $\text{O}(2p)$  bands are located between  $-7$  eV and  $-1.7$  eV. Then the cobalt-derived  $\text{Co}(3d)$  bands are split between the  $t_{2g}$  manifold (between  $-1.5$  eV and  $0.2$  eV) and the  $e_g$  manifold (between  $1$  eV and  $2.5$  eV). The oxygen states hybridise significantly with the cobalt bands. This hybridisation is stronger for  $e_g$  than for  $t_{2g}$ . Indeed, the  $e_g$  orbitals point towards the oxygen atoms, while the  $t_{2g}$  orbitals point in between the oxygen atoms.

The orthogonal frame attached to the lattice, used to define the directions  $(x, y, z)$  entering in the atomic orbitals expressions, does not correspond to the natural hexagonal frame created by the oxygen cage, in which the  $e_g$  and  $t_{2g}$  orbitals are usually defined. In the rotated frame, the  $a_{1g}$  orbital corresponds to  $d_{z^2}$ . The expressions for the other  $t_{2g}$  and  $e_g$  orbitals are more complicated and provided in Appendix B.1.

### 7.3.4 Partial-charge distribution in real space

It is possible to get an intuitive, real-space view of the various band characters described above. To do this, we consider the various Kohn-Sham states at the  $\Gamma$ -point:  $a_{1g}(\Gamma)$ , the sum of the two degenerate  $e'_g(\Gamma)$  and the sum of the two degenerate  $e_g(\Gamma)$ . In Fig. 7.5, we represent the quantity  $|\psi_{n,k=\Gamma}(\mathbf{r})|^2$ .

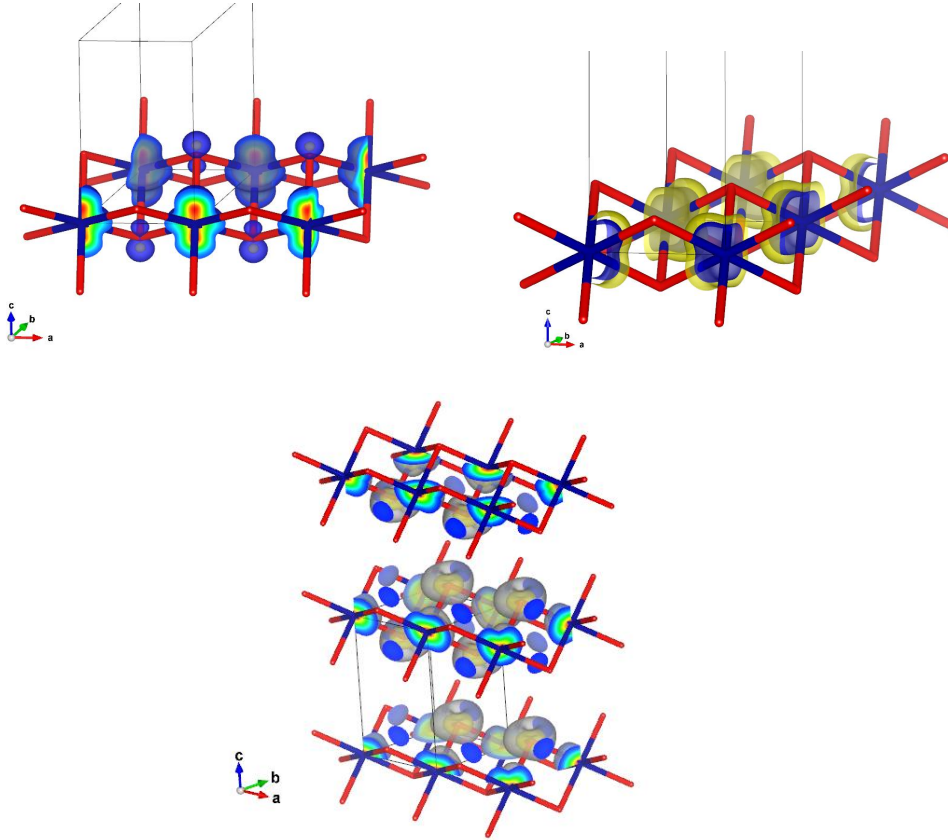


Figure 7.5: Real-space representations of the charges associated to various Kohn-Sham states. 1)  $a_{1g}(\Gamma)$  is an anti-bonding state between the  $\text{Co}(d_{z^2})$  and  $\text{O}(p_z)$  orbitals. 2)  $e'_g(\Gamma)$  is purely centered on Co atoms, with no hybridisation with O. 3)  $e_g(\Gamma)$  is strongly hybridised with O.

These pictures complete the view on the level of hybridisation between the oxygen states and the cobalt states. The Kohn-Sham state  $a_{1g}(\Gamma)$  results from a superposition between cobalt  $d_{z^2}$  and oxygen  $p_z$  states. From Fig. 7.5, this superposition is anti-bonding, with minima in the charge distribution between the cobalt and the oxygen atoms. One can speculate that the dispersion of the  $a_{1g}$  band arises from hopping processes between  $\text{Co}(d_{z^2})$  and  $\text{O}(2p_z)$  orbitals. A minimal model for the structure if this band is found in Appendix B.2.

In Fig. 7.5, the states  $e'_g(\Gamma)$  are purely centered around cobalt atoms, with virtually no hybridisation with oxygen. Their lobes point between oxygen atoms. One can speculate that the dispersion of the  $e'_g$  bands arises from direct hopping processes between cobalt atoms.

Finally, the states  $e_g(\Gamma)$  in Fig. 7.5 result from a strong hybridisation with oxygen  $p_x$  and  $p_y$  states. The main hopping process here is cobalt-to-oxygen hopping.

## 7.3.5 Fermi surface

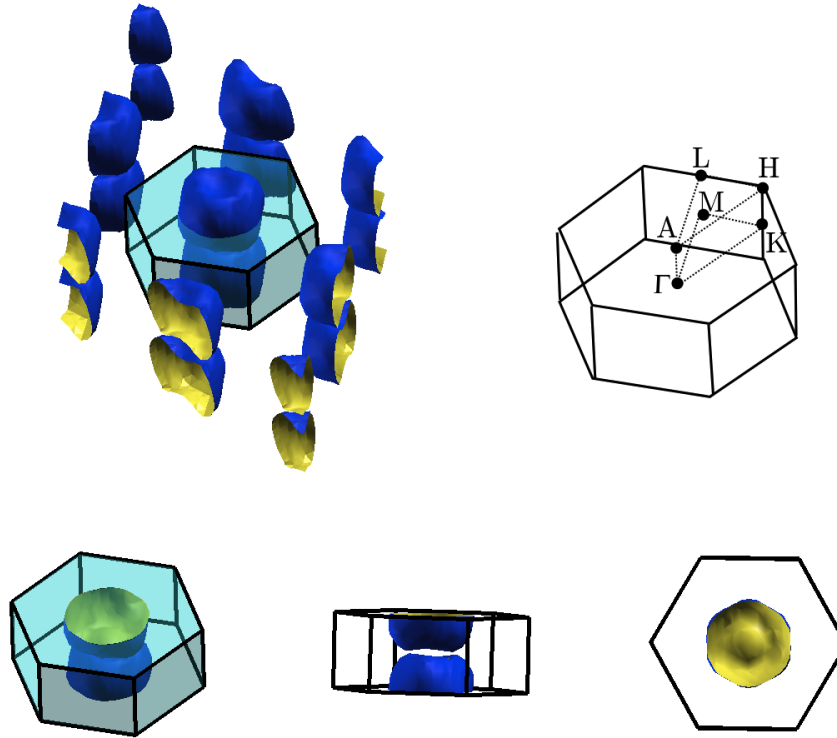


Figure 7.6: Fermi surface of the  $\text{CoO}_2$  planes in the  $aa$  stacking, doped with electrons, viewed with various angles. The  $\Gamma$  point is occupied. The Fermi surface consists of one sheet.

It is important to properly determine the Fermi surface of the  $\text{CoO}_2$  planes, because of the presence of numerous instabilities in the experimental phase diagram of the cobaltates. In particular, should the Fermi surface be nested, instabilities are expected at the nesting vector. They would appear as divergences in the static susceptibility at the nesting vector. However, in view of the very weak dispersion of the  $t_{2g}$  manifold, with a bandwidth of approximately 1 eV, precisely determining the Fermi-surface topology is a difficult task. It would require to know the Kohn-Sham eigenvalues to a precision of about 100 meV.

The Fermi surface of the  $\text{CoO}_2$  planes is represented of Fig. 7.6. It consists of a single hole pocket, centered around the  $A$  point (in the plane  $k_z = 1/2$ ). In particular, the  $\Gamma$  point (in the plane  $k_z = 0$ ) is not included in the hole pocket. This means that the weak dispersion along the  $k_z$  direction is enough to influence the Fermi-surface topology, which is truly 3D-like.

In contrast to what is found upon doping with sodium, and as already mentioned, a

single hole pocket is found for the  $\text{CoO}_2$  planes doped with electrons. There are no extra pockets in the  $\Gamma K$  direction.

The Fermi surface is almost isotropic in the  $(k_x, k_y)$  horizontal plane. There is only a slight hexagonal distortion, due to the underlying triangular lattice. Remarkably, we find that for our particular doping, the radius of the Fermi surface is half of the  $\Gamma M$  distance. The  $a_{1g}$  band crosses the Fermi level at the point  $\Gamma M/2$ .

## 7.4 Effect of the oxygen stacking on the band structure

In the actual compound, successive  $\text{CoO}_2$  planes are not equivalent, due to the vertical alternation of oxygen positions. The  $\text{CoO}_2$  planes actually follow an  $ab$ -type of stacking. Until now, we have simulated  $aa$ -types of stacking. It is in principle necessary to clarify the effect of oxygen stacking on the  $\text{CoO}_2$  band structure. In the  $ab$  stacking, the unit cell

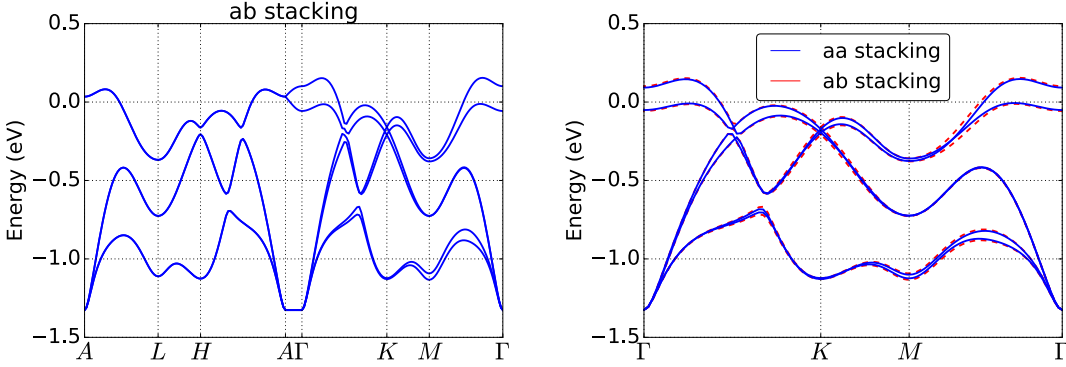


Figure 7.7: Band structures for the  $aa$  and  $ab$  stackings. In the  $ab$  stacking, the unit cell is doubled in the  $z$  direction, with inequivalent successive  $\text{CoO}_2$  planes. The  $ab$ -stacking band structure is shown on the left panel. On the right panel, the  $aa$ -stacking structure is folded and superimposed to the  $ab$  result. As far as the band structure is concerned, these stackings lead to equivalent results.

is doubled in the  $z$ -direction. In reciprocal space, this means that the first Brillouin zone is halved, and that there are twice as many bands. The  $ab$ -stacking band structure is represented on Fig. 7.7. It is possible to fold the bands of the  $aa$  calculations to compare them with the  $ab$  bands. As evidenced on Fig. 7.7, the band structures of the  $aa$  and  $ab$  stacking are equivalent. Hence, the oxygen stacking has virtually no influence on the band structure.

# 8 Impact of real-structure effects

In the previous chapter, we have obtained a band structure for simple  $\text{CoO}_2$  planes. These planes were considered as the minimal building blocks for the full compound,  $\text{Na}_{2/3}\text{CoO}_2$ . How are the previous band structures reliable in view of the actual, more complex material? In this chapter, we aim at a more realistic description of the band structure of the material. We analyse the effect of various key parameters on the band structure, and see how they influence the physical electronic processes.

## 8.1 Effect of sodium doping

One of our aims is to check the effect of doping with explicit sodium ions, as compared to electron-doping, which has been performed in the previous chapter. A priori, including the sodium ions should at least induce an external potential change. We shall see that doping with explicit sodium ions induces some important changes in the band structure, and hence in the key microscopic electronic processes. These changes are due to the local symmetry-breaking around each atom, Co and O, induced by the dopants. Since local symmetries are reduced, the Kohn-Sham wave-functions cannot take a symmetric form as those depicted in Fig. 7.5. The local-symmetry breaking particularly affects the anti-bonding state  $a_{1g}(\Gamma)$ , whose energy decreases upon doping with sodium. The symmetry-breaking also induces a slight charge-disproportionation around both Co and O atoms.

### 8.1.1 The tripled unit cell: presentation

In the unit formula  $\text{Na}_{2/3}\text{CoO}_2$ , the sodium content is a rational number. There are exactly 2 sodium ions per tripled  $(\text{CoO}_2)_3$  cell. We resort to tripled unit cells to simulate sodium-doping. A tripled unit cell contains 3 times more Co and O atoms, hence 3 times more Co and O bands than the minimal unit cell.

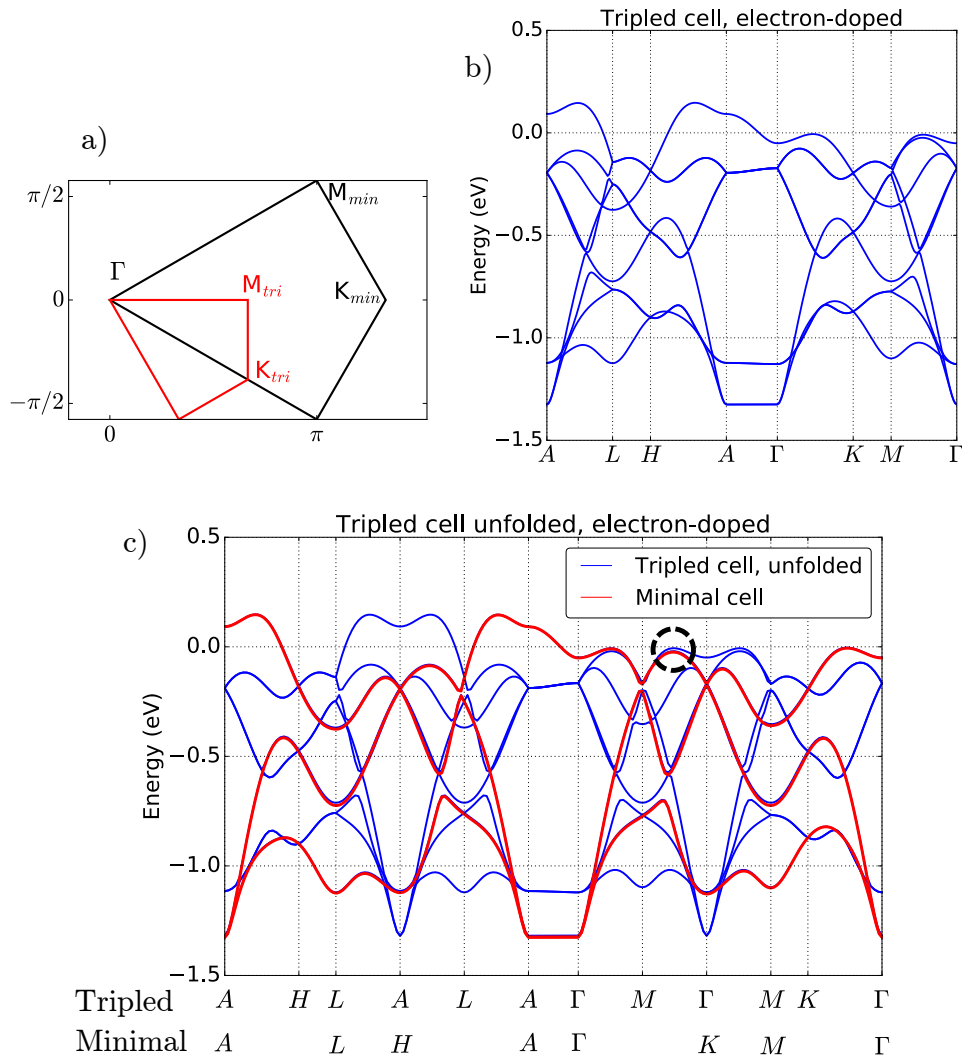


Figure 8.1: a) Brillouin zone for the minimal and the tripled cells. b) and c) Band structure for the tripled unit cell, doped with electrons. In c) the tripled cell band structure is superimposed to a minimal-cell one and the correspondence between the high-symmetry points is indicated below.

In principle, for electron-doping, the Kohn-Sham states for the tripled and the minimal unit cells are equivalent, since they correspond to the same physical system. As a first step, we compare electron-doped calculations for a minimal and a tripled unit cell, in order to clarify the correspondence of reciprocal-space points. The first Brillouin zone for the minimal and tripled cells is depicted in Fig. 8.1a). Since the tripled unit cell is larger in real-space, its reciprocal-space counterpart is smaller. In the case of electron-doping, it is possible to unfold the tripled-cell band structure, in such a way that it superimposes to the minimal cell one. This unfolding is presented in Fig. 8.1c). The correspondence

for the  $\mathbf{k}$ -point paths is presented under the figure. In Fig. 8.1c), we also circle some  $e'_g$  states between  $\Gamma$  and  $K$  for the tripled cell (between  $\Gamma$  and  $M$  for the minimal cell). These states will prove important in the next paragraph, because they will be responsible for the appearance of hole pockets.

There are two inequivalent sodium positions, Na1 and Na2, on top of cobalt atoms and on top of cobalt triangles, respectively. These two positions are illustrated in Fig. 2.2. A tripled unit cell is too small to reproduce even a part of the experimental sodium arrangement [10]. In the following, we work with two inequivalent sodium structures. Struct Na1 has two Na1 atoms, while Struct Na2 has two Na2 atoms. It is not possible to design a structure with one Na1 and one Na2 atom in a tripled cell, because they would lie too close to one another.

### 8.1.2 Sodium: a pure electron-donor?

So far, we have considered the sodium atoms as pure electron-donors. Is this assumption really correct? How much electrons does each sodium ion actually give to the  $\text{CoO}_2$  planes? Where do the sodium states lie in the band structure? Note that the presence of sodium can also lead to local lattice distortions; these will be discussed later.

In principle, each sodium ion wants to empty its  $3s$  shell, thus taking the configuration  $\text{Na}^+$ . To check whether this view is correct, we compute ion-projected densities of states for both structures, struct Na1 and struct Na2 (see Fig. 8.2). Here, the states are projected onto atomic orbitals within spheres centered around sodium, with a radius of  $3.32 \text{ \AA}$ . Most of the sodium  $3s$  states lie at high energies above the Fermi level, starting

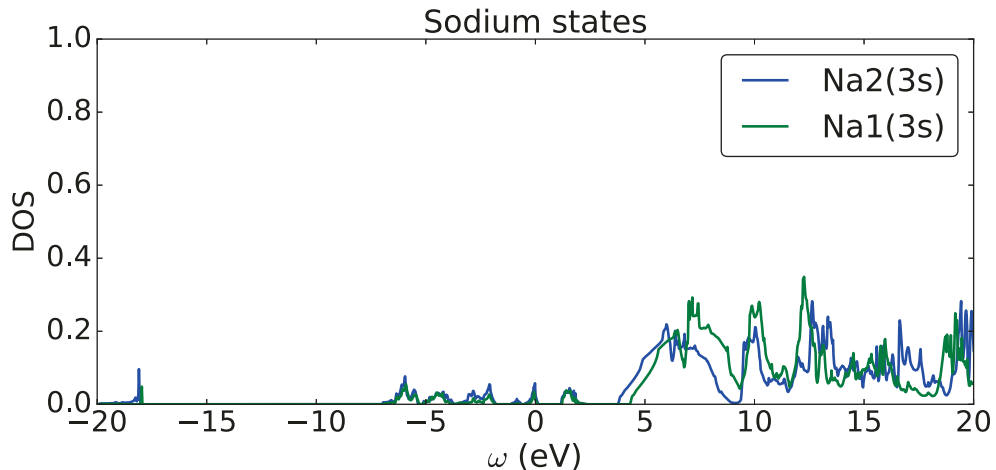


Figure 8.2: Sodium-projected density of states, performed on the two structures, struct Na1 and struct Na2. Only the  $s$  orbital component is shown.

from 4 eV. This confirms the ionic picture of sodium taking the local valence  $\text{Na}^+$ . These states are widely dispersive and very delocalised, resulting in a wide bandwidth. This is to be expected for the atomic principal quantum number  $n = 3$ . The local valence of sodium can be checked as well, again evaluated within a radius of 3.32 Å. We roughly find a local valence between 0.1 and 0.2 electron per  $s$  state per sodium ion. These numbers, however small, may even be overvalued by the fact that some oxygen  $2p$  electrons may tunnel into the Na spheres (the sodium potential being very shallow), thus artificially appearing as  $\text{Na}(3s)$  electrons.

### 8.1.3 Does sodium doping change the low-energy band structure?

The sodium-doped band structures, for both Struct Na1 and Struct Na2, are shown in Fig. 8.3. They are compared to electron-doped band structures. The main effect of sodium-doping is to reduce the bandwidth, as compared to electron-doping. This remark is true for the two sodium arrangements, with Na1 and Na2. This means that sodium-doping localises the charge carriers. Another important effect produced by sodium, happening on a scale of a few 100 meV, is the appearance of a hole pocket between  $\Gamma$  and  $M$  (see also the dotted black circle in Fig. 8.1). A change in the Fermi-surface topology is a significant fact, in view of the numerous instabilities developed by the cobaltates. These hole pockets have hence been intensely debated in the literature. Here, the hole pockets appear as a consequence of sodium-doping. They are present for both structures, with Na1 and Na2; they are absent for electron-doping.

In order to investigate more the  $e'_g$  states responsible for the hole pocket, we represent the partial-charge associated to these specific Kohn-Sham states. The partial-charge densities for the  $e'_g$  states, at a  $\mathbf{k}$ -point where the pocket appears, is represented in Fig. 8.4. Fig. 8.4 compares electron-doped, and sodium-doped with Na1 and Na2 settings. From the figure and from the explicit orbital decomposition, these states are roughly identical in these three settings. Hence, these  $e'_g$  states do not actually change nature upon doping with sodium.

In order to track the physical effect of sodium-doping on the electronic structure, we perform the following operation. We shrink the electron-doped band by a factor 0.96, accounting for the localisation induced by sodium. Then we shift it by 0.05 eV, in order to align the  $e'_g$  levels. The result is displayed in Fig. 8.5. Most of the bands fall on top of each other. The major discrepancy comes from the states around  $a_{1g}(\Gamma)$ . This might mean that sodium-doping mostly affects the state  $a_{1g}(\Gamma)$ .

Indeed, the presence of the sodium ions implies that the Kohn-Sham state  $a_{1g}(\Gamma)$  is not a symmetric anti-bonding state anymore, as represented in Fig. 7.5 for the case of electron-doping. In Fig. 8.6, the partial-charge densities of  $a_{1g}(\Gamma)$  for the electron-doped and sodium-doped settings are depicted.

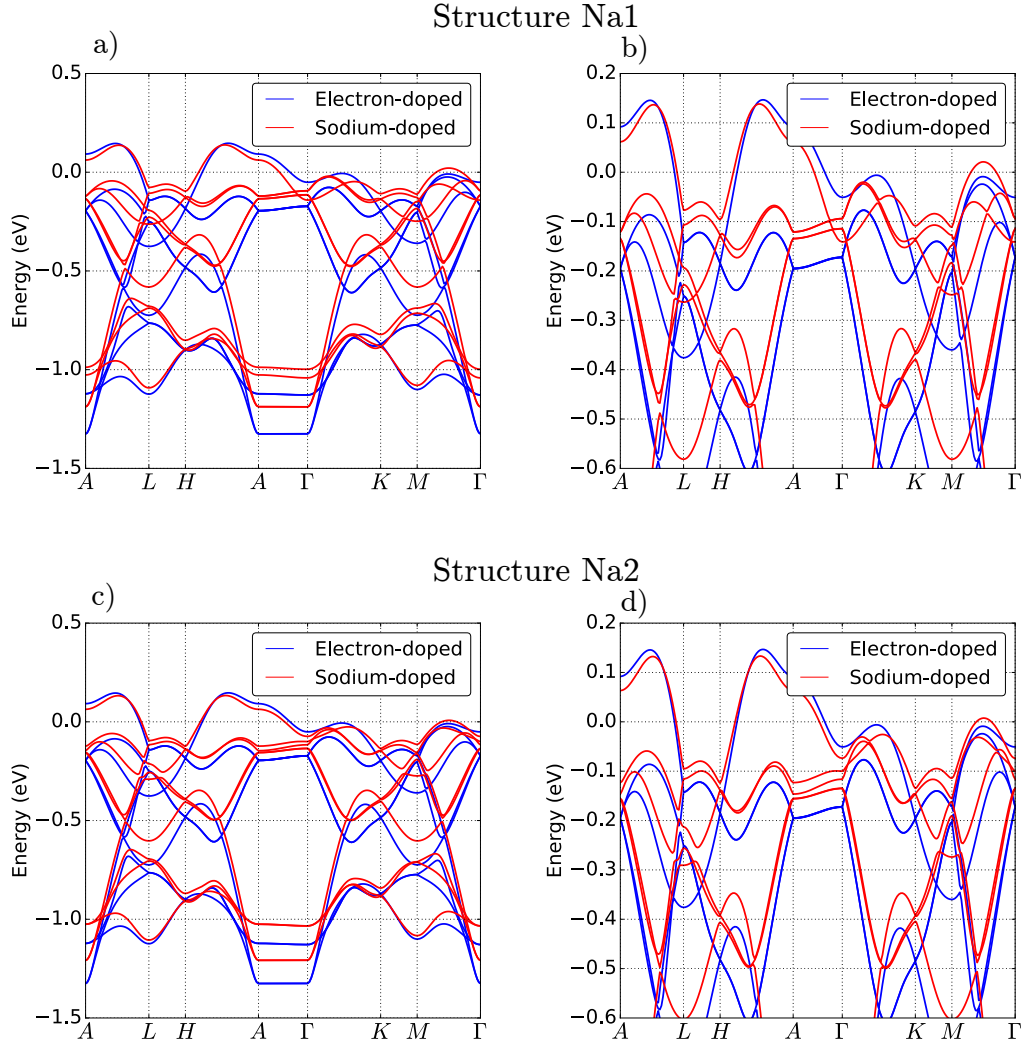


Figure 8.3: Band structure upon doping with sodium, compared to electron doping. a) and b) Structure Na1, displaying the same data on a different scale. c and d) Structure Na2, displaying the same data on a different scale.

When doping with Na2 ions, the state  $a_{1g}(\Gamma)$  becomes a superposition between various  $\text{Co}(t_{2g})$  and  $\text{O}(2p)$  atomic orbitals, and not only between  $\text{Co}(d_{z^2})$  and  $\text{O}(p_z)$ . This is visible in Fig. 8.6. Also, it is visible from the figure that not all oxygen atoms are equivalent.

When doping with Na1 ions, the different cobalt atoms in the unit cell become non-equivalent. This is not immediately visible in Fig. 8.6. However, one can look at the orbital-projections of the wave-function for  $a_{1g}(\Gamma)$ . The projection on  $d_{z^2}$  for cobalt atoms just under Na has a weight 0.235; the projection on  $d_{z^2}$  for cobalt atoms with no neighbouring Na is 0.292. This amounts roughly to a 25% difference of weight in the

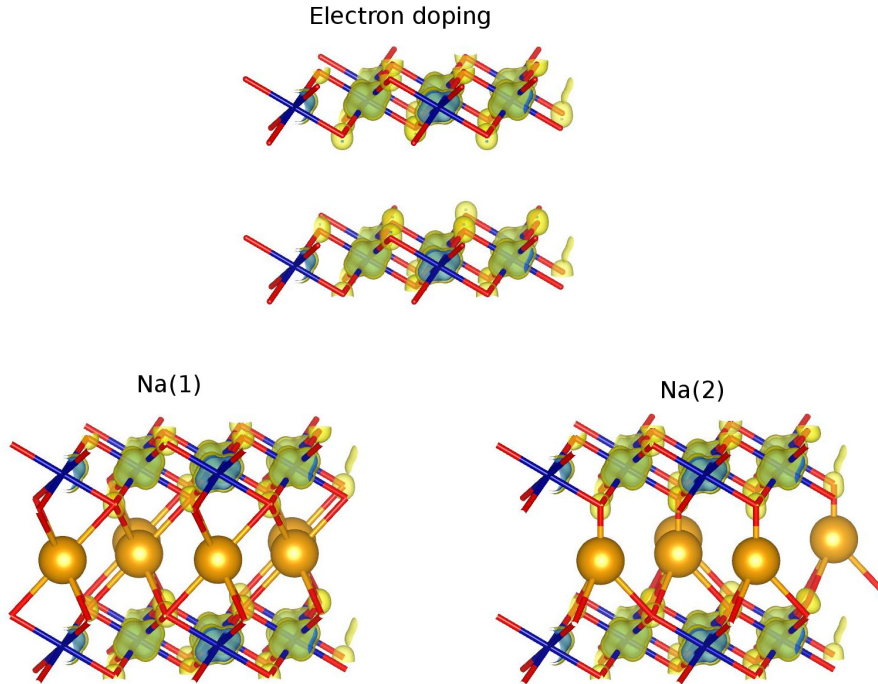


Figure 8.4: Partial-charge for the states forming the  $e'_g$  hole pocket. Results are displayed for tripled cells, both electron-doped and sodium-doped. Despite the differences in the presence or position of the sodium ions, the three partial charges displayed look very similar.

wave-function.

Hence, the presence of the sodium ions breaks local symmetries, implying that the particular state  $a_{1g}(\Gamma)$  is not a symmetric anti-bonding state when sodium is present. This state not being perfectly anti-bonding means that its energy is lowered with respect to the electron-doped case.

Sodium-doping hence induces a lowering of the energy of the state  $a_{1g}(\Gamma)$ , causing a part of the  $a_{1g}$  band to fall below the Fermi level. Since the electron count is a fixed number, some states from  $e'_g$  have to go above the Fermi level, causing the appearance of the  $e'_g$  hole pockets.

In conclusion, the doping technique, and in particular the explicit sodium doping, affects essentially the  $a_{1g}(\Gamma)$  Kohn-Sham state. By doing so, it changes the relative alignment of states, creating extra  $e'_g$  pockets.

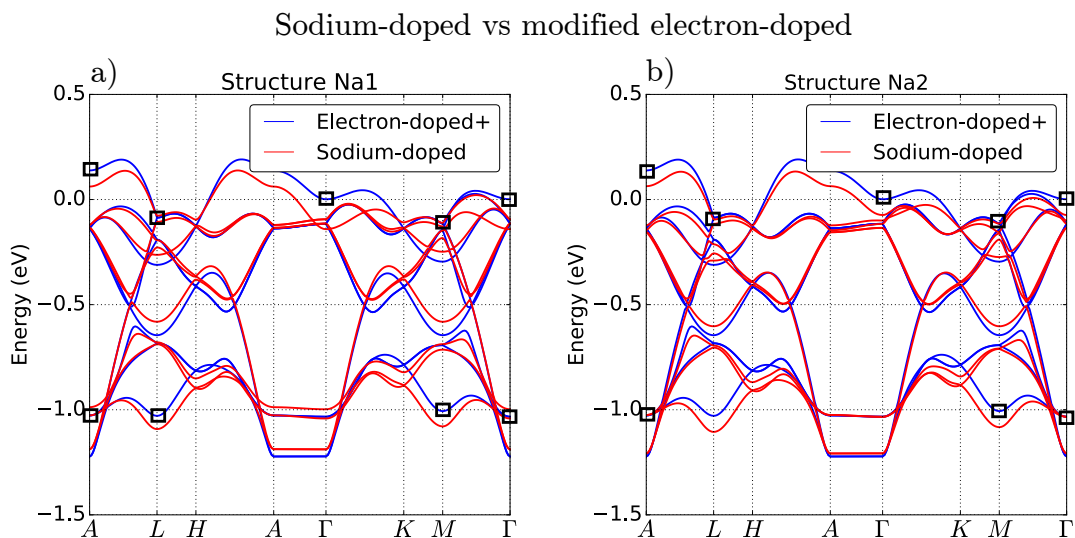


Figure 8.5: Band structures for sodium doping, compared to modified electron doping. The electron doping bands have been modified: they are compressed and shifted, as explained in the main text. The black boxes indicate, for the electron-doped curve, states with  $a_{1g}$  character.

#### 8.1.4 Local valence and sodium-induced charge disproportionation

In the sodium-doped cell, a slight charge-disproportionation occurs due to the presence of the sodium. As we have argued, when sodium is present, not all cobalt or oxygen atoms are equivalent. The sodium potential induces a rearrangement of charges.

There are some systematics in this rearrangement. When a sodium ion is present on top of another atom (cobalt or oxygen), then this atom attracts more charge.

In the structure Na1, the sodium ions are on top of cobalt atoms. Cobalt atoms with no neighbouring sodium have 7.27 electrons in their  $d$  shell, while cobalt atoms with sodium on top have 7.32 electrons in their  $d$  shell (defined within a sphere of radius 1.302 Å). Hence, the increase of electrons in the  $d$  shell due to the presence of sodium is around 1%. The local valence for oxygen is constant for the structure Na1.

In the structure Na2, the sodium ions are on top of oxygen atoms. Oxygen atoms with no neighbouring sodium have 3.43 electrons in their  $p$  shell, while oxygen atoms with sodium on top have 3.48 electrons in their  $p$  shell (defined within a sphere of radius 0.820 Å). This is again a small difference, of order 1%. There is no difference on the local valence of cobalt for the structure Na2.

Most importantly, it is interesting to note that the charge-disproportionation does not concern only the cobalt atoms. The charge is disproportionate between both the cobalt

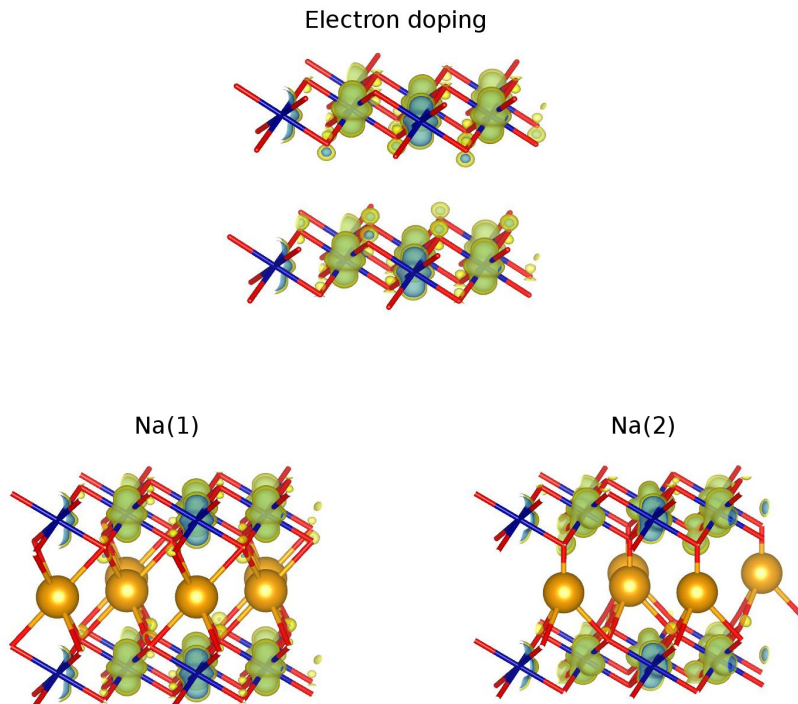


Figure 8.6: Partial-charge for the states  $a_{1g}(\Gamma)$ . Results are displayed for tripled cells, both electron-doped and sodium-doped. The potential created by the sodium introduces some differences between these Kohn-Sham states.

atoms and the oxygen atoms. We can speculate that this remark holds also for the real compound, where the charge-disproportionation has a larger amplitude.

## 8.2 Effect of the crystalline structure: interplanar distance and oxygen positions

In our previous calculations, we used experimentally-determined atomic positions. We did not perform atomic relaxation. In this section, we assess the sensitivity of the system to some atomic distances. We vary these distances to look for general trends that they may induce on the electronic structure.

## 8.2. Effect of the crystalline structure: interplanar distance and oxygen positions

### 8.2.1 interplanar distance

We start by varying the interplanar distance, keeping the cobalt-oxygen distances fixed within a  $\text{CoO}_2$  plane. We drastically vary the interplanar distance, in order to look for general trends.

The experimental interplanar distance is about  $5.4 \text{ \AA}$ . We keep  $ab$ -types of stacking, to have a more realistic  $k_z$  dispersion due to the oxygen positions. We first increase the interplanar distance by about 30%. The result is shown in Fig. 8.7. Most of the bands are relatively unaffected. However, upon increasing the interplanar distance, a dispersive band appears. This dispersive band encodes the fact that when a large vacuum region is created between the planes, free-electron modes can appear, that do not feel the effect of the external potential created by the  $\text{CoO}_2$  planes. When the interplanar distance is augmented, these free-electron modes go down in energy. A similar effect was observed in other layered materials such as for example graphite [151].

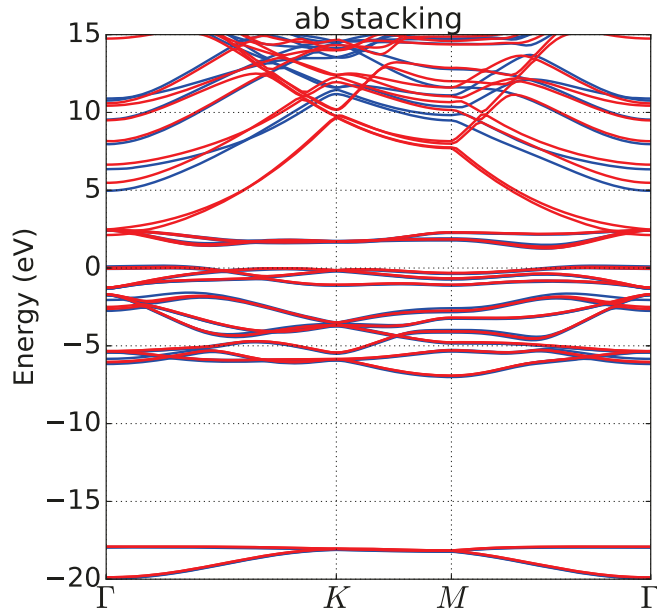


Figure 8.7: Augmented interplanar distance, from  $5.44 \text{ \AA}$  (experimental value, displayed in blue), to  $7.5 \text{ \AA}$  (displayed in red). A dispersive, free-electron band appears for the larger interplanar distance.

By lowering the interplanar distance by roughly 30%, another effect is observed, as depicted in Fig. 8.8. First, an energy gap opens up between the localised states (derived from oxygen  $2s$ ,  $2p$  and cobalt  $3d$ ) and the dispersive unoccupied states. Second, concerning the low-lying  $t_{2g}$  manifold, the band dispersion along  $k_z$  is more pronounced when the  $\text{CoO}_2$  planes are closer. This can be seen in the fact that replica form in the

$k_z$  direction.

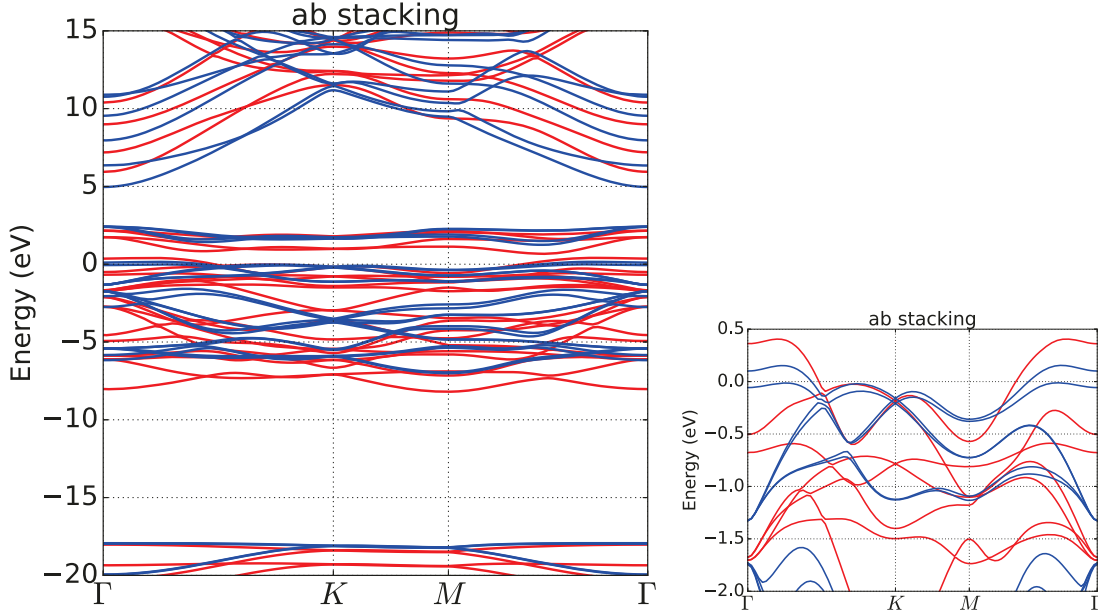


Figure 8.8: Lowered interplanar distance, from 5.44 Å (experimental value, displayed in blue), to 4 Å (displayed in red). The left and right panel display the same data on a different scale. Upon lowering the interplanar distance, the dispersion along  $k_z$  is more pronounced.

### 8.2.2 Oxygen positions

We vary the oxygen positions in the  $z$ -direction (equivalently, along the  $c$  axis), by keeping the interplanar distance fixed. Again we vary the oxygen positions by a large factor, in order to analyse general trends. The low-energy band structures for elongated and compressed oxygen octahedra are shown in Fig. 8.9. In both cases, the qualitative picture of the low-energy dispersion is the same. As expected, for elongated octahedra, the bandwidth is smaller, due to the smaller overlap between oxygen and cobalt. For the perfectly symmetric octahedra (elongated by 20 % with respect to the experiment) the crystal-field splitting between the  $a_{1g}$  and the  $e'_g$  states vanishes. This allows for mixing between these orbitals. For the compressed case, however, the degeneracy lifting for  $a_{1g}$  is more pronounced; this is particularly visible on the  $AL$  and  $\Gamma M$  segments.

Hence, there are clear trends for the variation of the electronic structure with structural degrees of freedom. In particular, changes in the interplanar distance or in the oxygen positions induces changes in the Fermi surface.

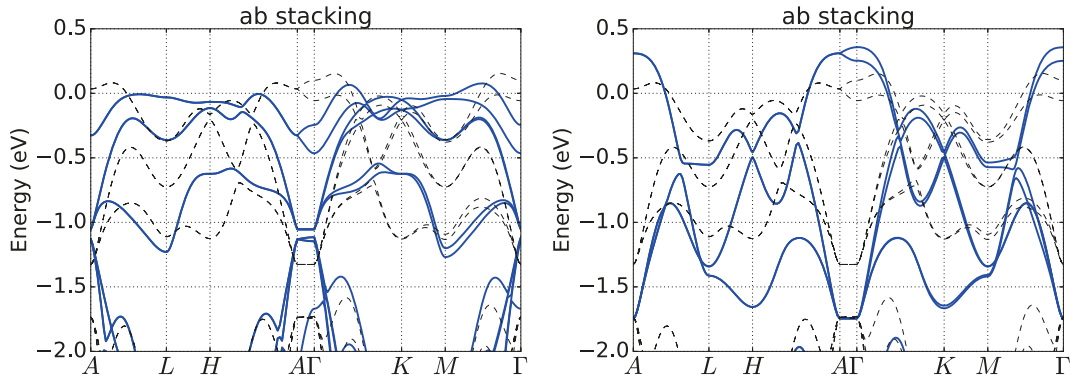


Figure 8.9: Band structures for various oxygen positions. On the left panel, the oxygen octahedra are elongated by 20% along the  $c$  axis with respect to the experiment. The present octahedra are symmetric. On the right panel, the octahedra are compressed by 20% along the  $c$  axis with respect to the experiment. In both panels, the band structure with oxygen positions corresponding to the experimental data is shown in dashed black.

### 8.3 Magnetism

From the experimental point of view, the system with sodium content  $x = 2/3$  should be close to a magnetic instability. Indeed, magnetic long-range order was detected for compounds with sodium contents greater or equal to  $x = 3/4$  [47]. The corresponding order was ferromagnetic within the  $\text{CoO}_2$  planes and antiferromagnetic in the direction perpendicular to the planes. In this section, we introduce the magnetic degree of freedom and perform spin-polarised calculations. The results are displayed for an  $aa$ -type of stacking, assuming a ferromagnetic solution (in- and out-of-plane). However, the  $ab$ -type of stacking was also calculated, assuming an antiferromagnetic solution out-of-plane. The results were similar, with similar staggered magnetic fields and total energies. The band structures corresponding to spin-polarised calculations for the undoped and the electron-doped cases in the  $aa$ -stacking are presented in Figs. 8.10 and 8.11. In both cases, the system is fully polarised, which is in line with the theoretical literature [52] (but not with experiments for these doping levels). The majority-spin  $t_{2g}$  bands are fully occupied. The total magnetisation is in agreement with this observation: it is 1 for the undoped case, and 0.333 for the doped case. Additionally, the cobalt ions are found to carry most of the magnetisation: the local moment is 0.8 per cobalt in the undoped case, and 0.28 per cobalt in the doped case.

Hence, our spin-polarised DFT calculations fail to reproduce some magnetic fluctuations evidenced at intermediate doping, with a crossover from antiferromagnetic to ferromagnetic in-plane correlations [46]. Our calculations capture well the tendency to ferromagnetism. However, they do not reproduce the competing tendency towards anti-ferromagnetism. These antiferromagnetic fluctuations may be due to short-range

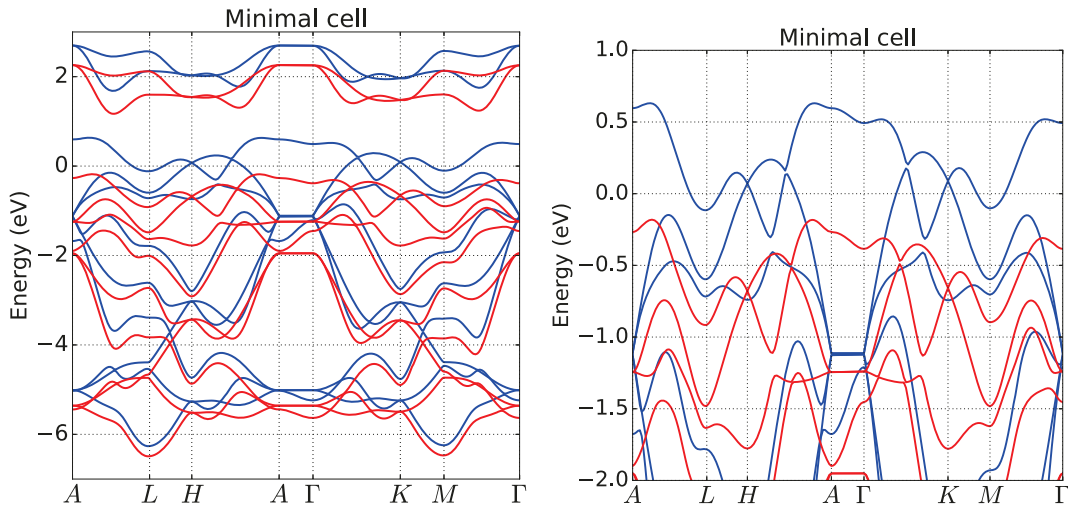


Figure 8.10: Magnetic (spin-polarised) band structure for an undoped cell. The majority-spin band is displayed in red, and the minority-spin in blue.

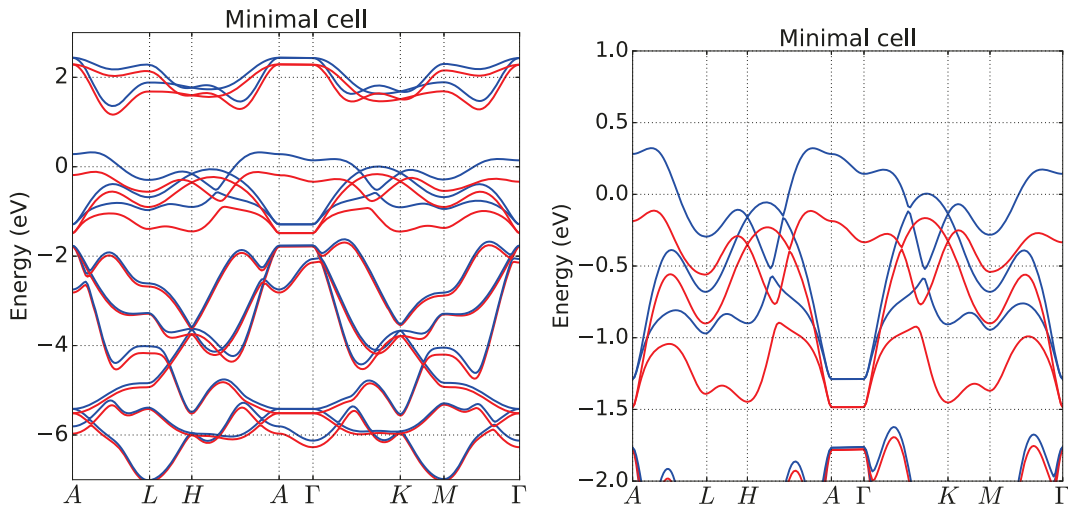


Figure 8.11: Magnetic (spin-polarised) band structure for a doped cell.

antiferromagnetic exchange interactions [78]. This effect is particularly challenging to reproduce within LDA or GGA without resorting to explicit symmetry-breaking.

It is important to keep in mind that magnetism may change the electronic band structure. By doing so, it may also change the topology of the Fermi surface.

# 9 *Ab initio* susceptibilities

In Part II, we performed an EDMFT study on an effective low-energy model for the cobaltates. We found that, in the high-doping regime, the interacting susceptibility could be approximated by its non-interacting counterpart, such that  $\chi \approx \chi_0$ . This result is true even for large interaction strengths and was found using a non-perturbative method. However, this conclusion has been drawn on an effective low-energy model. Considering higher-energy processes would involve more bands or frequency-dependent parameters  $U(\omega)$ ,  $V(\omega)$ ... In this chapter we combine this insight gained from EDMFT with *ab initio* calculations for the susceptibility.

In Chap. 7 and Chap. 8, we have computed the band structure for  $\text{CoO}_2$  planes and discussed its dependence on some physical parameters. In this chapter, we compute the *ab initio* susceptibility of doped  $\text{CoO}_2$  planes. We use two different approximations for the susceptibility, namely the non-interacting and the random-phase approximation. We interpret these results in terms of excitations of the electronic system. To make connections with our model study, we compare the non-interacting susceptibilities from the *ab initio* calculations to the model ones. Then, by a comparison between the RPA susceptibilities for the *ab initio* and model cases, we obtain an estimate for  $U$  and  $V$ .

The computation of the susceptibilities was done using the  $GW$  routines of the VASP package [152], where  $W$  is calculated, with a further implementation by Claudia Rödl to make the  $\mathbf{q}$ -dependent susceptibilities accessible. More details about the calculation of the non-interacting susceptibilities are provided in Appendix. D.

## 9.1 The non-interacting susceptibility: $\chi_0$

For the susceptibility calculations, we use a minimal cell within the *ab* stacking, doped with electrons. In Chap. 7, we analysed results obtained for a minimal cell within the *aa* stacking. The band structure for the *ab* stacking was found to be equivalent. In this chapter, we want to be able to capture any effect produced by the stacking of the real

structure. These effects can emerge from the matrix elements in the calculation of the non-interacting susceptibility. We use a  $18 \times 18 \times 4$   $\mathbf{k}$  point grid. The number of bands is converged to 128 bands. The broadening  $\eta$  is set to 0.1 eV. For the calculation of the susceptibility within the random-phase approximation, a  $\mathbf{q} + \mathbf{G}$  vector cutoff of 150 eV is introduced. The convergence was checked on the value of the microscopic (for the non-interacting susceptibility) and macroscopic (for the RPA susceptibility) dielectric function at  $\omega = 0$  for the high-symmetry  $\mathbf{q}$  points  $M$  and  $K$ . The dielectric function was converged to a precision of  $10^{-2}$ .

### 9.1.1 The *ab initio* non-interacting susceptibility

Let us first review the computed non-interacting susceptibility. The non-interacting susceptibility contains information about the transitions between individual Kohn-Sham states. Each allowed transition translates into a peak in the imaginary part of  $\chi_0$ . The height of the peak is given by the size of the matrix element connecting the two Kohn-Sham states. This is an independent-particle calculation, in the sense that it does not contain information about the reaction of all the particles in the system, upon excitation of a particle. The frequency dependence of the susceptibility is analysed by plotting  $\text{Im } \chi_0(\mathbf{q}, \omega)$ . This quantity is represented for three different  $\mathbf{q}$  points in Fig. 9.1. In our

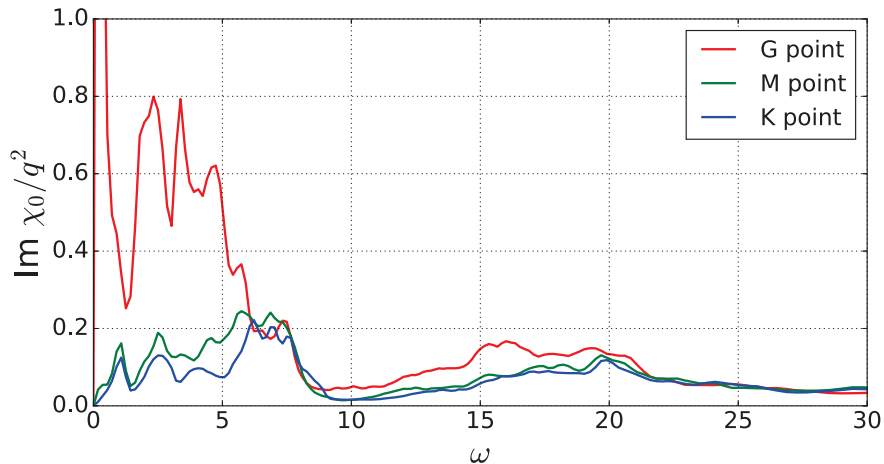


Figure 9.1: Imaginary part of the computed *ab initio* non-interacting susceptibility, divided by the square of the transferred momentum  $\mathbf{q}$ . The susceptibility was computed for two high-symmetry points,  $M$  and  $K$  and for  $G$ , which lies close to  $\Gamma$ .

case, the  $G$  point actually corresponds to the smallest point within the  $\mathbf{q}$  point mesh, of coordinates  $(0.05556, 0, 0)$  in the reciprocal-space basis. The  $G$  point is hence on the  $\Gamma M$  line. Moreover, in Fig. 9.1, we renormalised the curve by  $|\mathbf{q}|^2$ : this is because the non-interacting susceptibility at small  $\mathbf{q}$  goes as  $|\mathbf{q}|^2$ . Two main groups of transitions can be observed, the first one below 10 eV, the second one between 10 and 20 eV.

Fig. 9.2 gives an idea about the dispersion of the peaks in  $\text{Im } \chi_0$  along the paths  $\Gamma K$  and  $\Gamma M$ . Since the bands closest to the Fermi level are weakly dispersive, as they originate from localised  $3d$  states, the peaks in  $\text{Im } \chi_0$  disperse weakly as well.

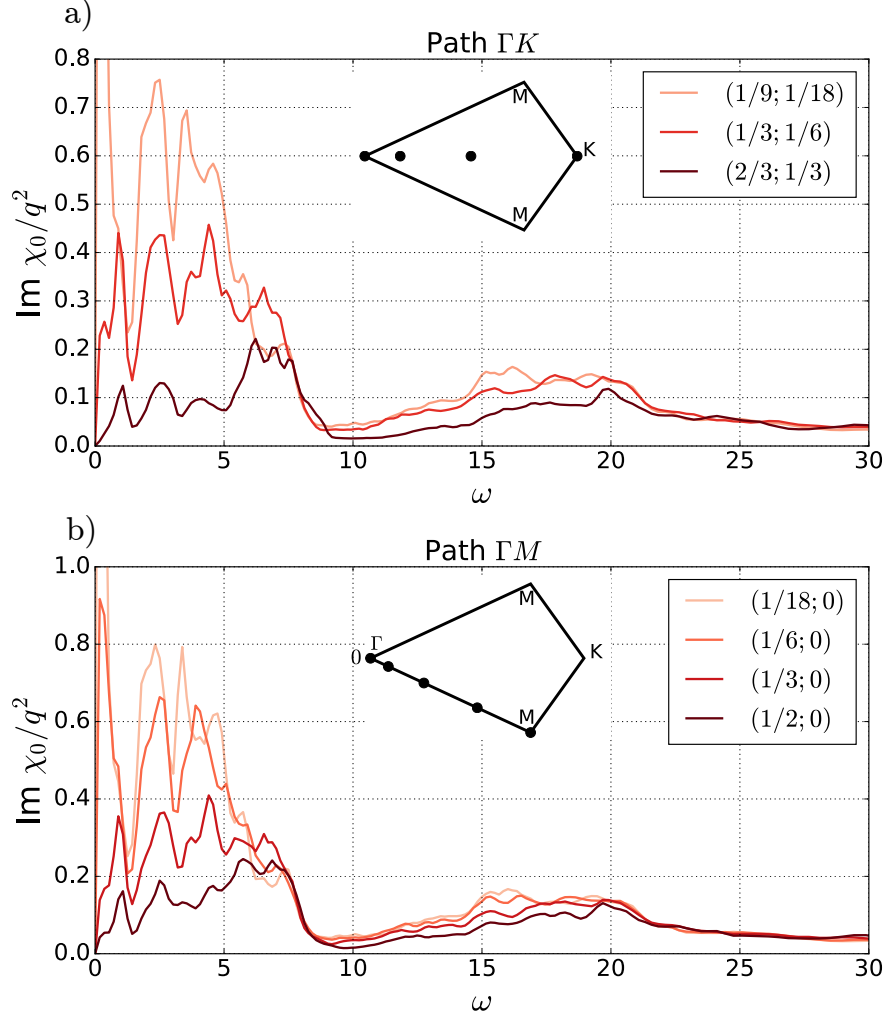


Figure 9.2: Analysis of the dispersion of the peaks in  $\text{Im } \chi_0$  along two inequivalent directions,  $\Gamma K$  and  $\Gamma M$ . The  $\mathbf{q}$  points along the paths are represented in the Brillouin zone in the insets. The legend corresponds to their coordinates in the reciprocal-lattice basis.

As already discussed, the various peaks of the non-interacting susceptibility in Fig. 9.1 can be directly assigned to individual transitions between Kohn-Sham states. We analyse this further by computing susceptibilities allowing for only some specific transitions and comparing the individual peaks to the full result of Fig. 9.1. This analysis is performed in Fig. 9.3. Hence, the peak at 1 eV correspond to intraband  $t_{2g}$  transitions. The broader peak at 2.5 eV corresponds to interband  $t_{2g}$  to  $e_g$  transitions.  $O(2p)$ -to- $t_{2g}$  transitions

are weak and located between 2.5 and 4.5 eV.  $O(2p)$ -to- $e_g$  transitions have much more weight, as expected from the strong hybridisation between the  $e_g$  states and oxygen. They are located between 3 and 9 eV.

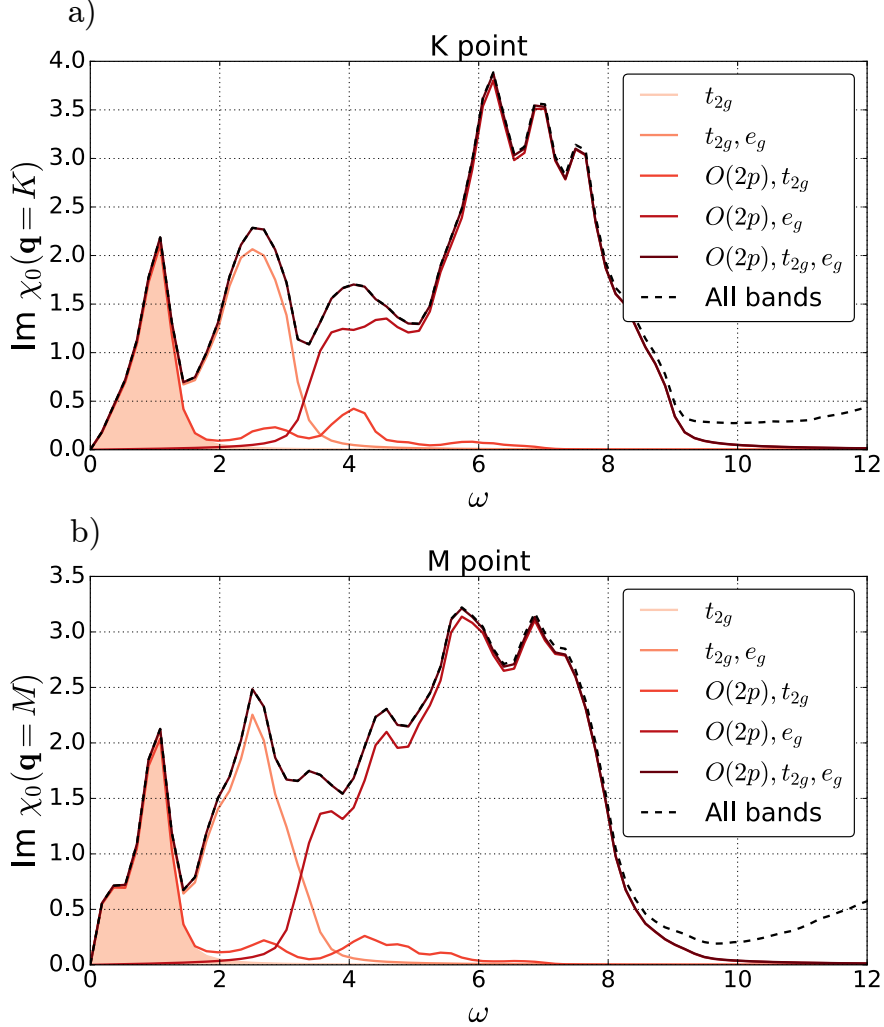


Figure 9.3: Analysis of  $\text{Im } \chi_0$  in terms of transitions between Kohn-Sham states. The low-energy part of the spectrum (up to 1.5 eV) is well reproduced by the intra  $t_{2g}$  transitions only. The transitions involving other bands occur at higher energies.

It is interesting to analyse the variations of  $\chi_0$  in reciprocal space. To this end, we analyse  $\text{Re } \chi_0(\mathbf{q}, \omega = 0)$ . The zero-frequency value of the susceptibility is important, because a possible divergence would signal a second-order transition (see Appendix D). For  $\mathbf{q} \neq 0$ , at zero frequency,  $\chi_0$  is purely real. In Fig. 9.4, the non-interacting susceptibility is computed both from an all-band and from a  $t_{2g}$ -only calculation. We see that the non-interacting susceptibility is  $\mathbf{q}$  dependent in both cases. In the all-band calculation, the maximum is located at the  $M$  point. This calculation contains transitions from all bands,

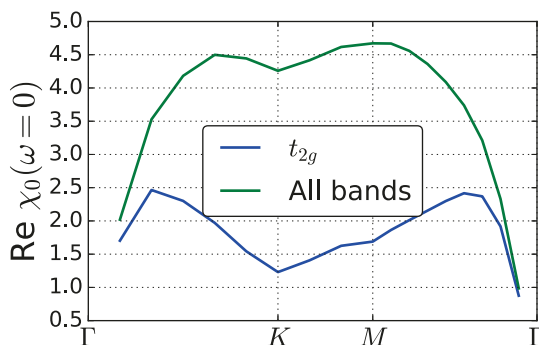


Figure 9.4: Real part of the static susceptibility,  $\text{Re } \chi_0(\mathbf{q}, \omega = 0)$ . The susceptibility was computed both using only intra- $t_{2g}$  transitions and using all bands. The numerical values are different, as well as the dispersion, with the location of maxima.

including high-energy transitions. The intra- $t_{2g}$  calculation leads to a different dispersion. For intra- $t_{2g}$  transitions only, Fig. 9.4 shows that the maxima in  $\text{Re } \chi_0(\mathbf{q}, \omega = 0)$  are located roughly at  $\Gamma M/2$  and  $\Gamma K/3$ . One can actually expect that the locus of the maxima is a cylinder of radius  $\Gamma M/2$ , centered around  $\Gamma$ . The  $t_{2g}$ -only calculation only contains low-energy transitions, between states close to the Fermi surface. In a metal with a nested Fermi surface, the  $\mathbf{q}$  dependence of  $\chi_0(\omega = 0)$  is dictated by the topology of the Fermi surface: a divergence is found at the nesting vectors. However, in our case, no divergence is found and the difference between the all-band and the  $t_{2g}$ -only calculations shows the importance of higher-energy transitions. They involve states not necessarily close to the Fermi surface, and contribute significantly to the dispersion of the all-band non-interacting susceptibility.

It is possible to interpret the particular dispersion of  $\text{Re } \chi_0(\mathbf{q}, \omega = 0)$  in the  $t_{2g}$ -only case. The dominant transitions appear to be those connecting the  $\Gamma$ -point to the Fermi surface. These transitions are characterised by vectors of length  $\Gamma M/2$ , approximately. The Fermi surface is located roughly halfway between  $\Gamma$  and  $M$  (see band structure on Fig. 7.7). Around the  $\Gamma$ -point, the states have energies close to the Fermi energy and the band is almost flat, resulting in a large density of states (a van Hove singularity). This creates a large phase space for transitions, numerically translating into the particular  $\mathbf{q}$  dependence of Fig. 9.4.

### 9.1.2 Comparison to the model

The *ab initio* non-interacting susceptibility can be compared to the non-interacting susceptibility of the model. On the model side, only transitions within the  $a_{1g}$ -like band are computed. The closest possible comparison is between the single-band model calculation and an *ab initio* computation, where we only allow for transitions within the

$t_{2g}$  manifold.

Let us first review the frequency dependence of  $\chi_0$  in Fig. 9.5. In the calculation of the Lindhard formula for the model, a broadening  $\eta = 0.05$  eV was introduced. The  $\mathbf{k}$  point discretisation creates wiggles for the model data. The curves for the *ab initio* and the

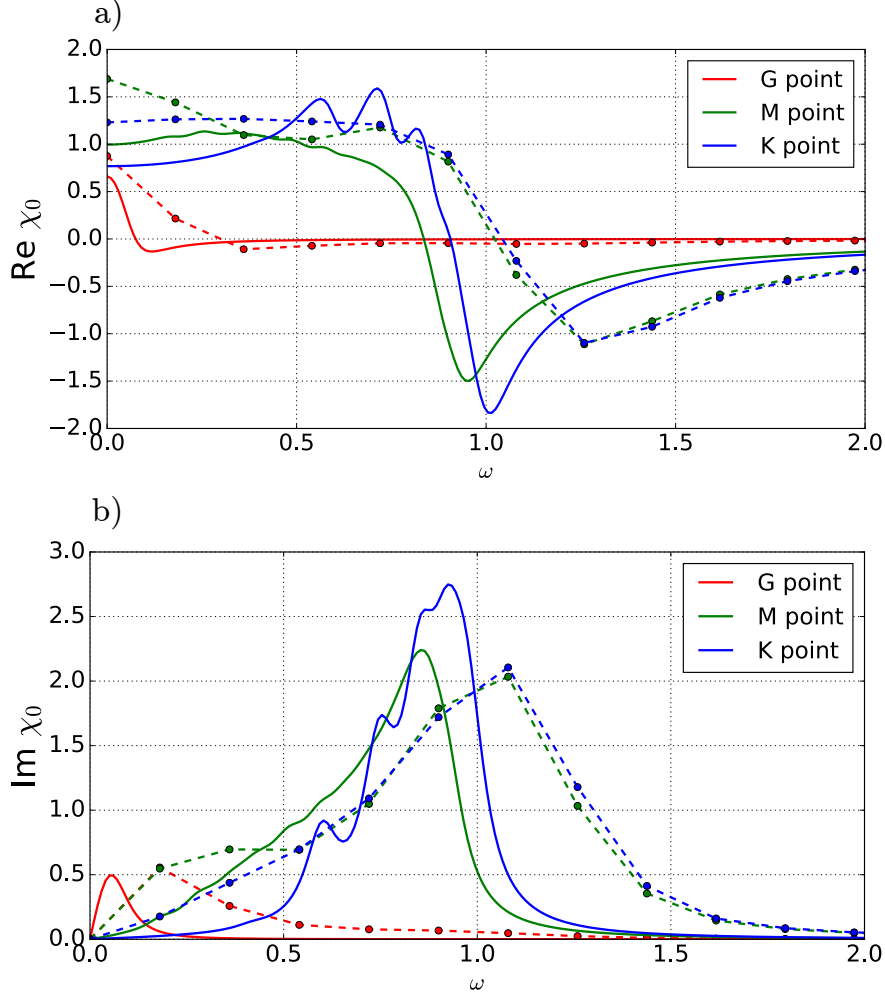


Figure 9.5: Real and imaginary part of the non-interacting susceptibility. For the model, we used the Lindhard formula. For the *ab initio* calculation, we computed a response function allowing only for intra- $t_{2g}$  transitions. Full line: model. Dashed line: *Ab initio*.

model in Fig. 9.5 look very similar. For the three high-symmetry  $\mathbf{q}$  points, the frequency trends are the same for the two systems. Only, the larger *ab initio* bandwidths make the peaks broader. For the  $G$  point, the only contributing spectral weight comes from transitions in the vicinity of the Fermi surface. The similarity between the model and *ab initio* susceptibilities is quite remarkable, given that we are comparing a one-band system to a three-band system. This means that  $e'_g$ -to- $a_{1g}$  transitions do not contribute

## 9.2. The susceptibility in the random-phase approximation (RPA): $\chi_{\text{RPA}}$

significantly to the three-band calculation.

We check that the model and *ab initio* non-interacting susceptibilities also agree at  $\omega = 0$  in reciprocal-space in Fig. 9.6. The qualitative agreement between the two types of

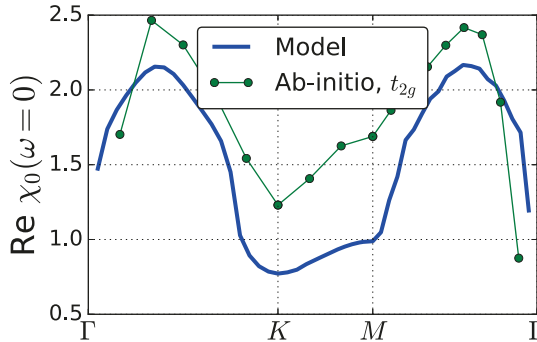


Figure 9.6: Zero-frequency value of the non-interacting susceptibility on a  $\mathbf{q}$  point path. The zero-frequency component is purely real. Comparison between model and *ab initio* calculations. The *ab initio* susceptibility was calculated with intra- $t_{2g}$  transitions only.

calculations is good again.

To conclude, we have shown that the model is able to reproduce the non-interacting susceptibility  $\chi_0$ , at least qualitatively. To compare model and *ab initio* non-interacting susceptibilities, one needs to restrict the transitions to intra- $t_{2g}$  only in the *ab initio* calculation.

## 9.2 The susceptibility in the random-phase approximation (RPA): $\chi_{\text{RPA}}$

In this section, we present *ab initio* results obtained within the Random-Phase Approximation (RPA). The RPA is interesting because it can give a first idea about the effects of interactions.

### 9.2.1 The *ab initio* RPA susceptibility

As for the non-interacting susceptibility, it is possible to examine both the frequency-dependence and the reciprocal-space dependence of the RPA susceptibility. We start by presenting the frequency-dependence. The behaviour of  $\chi_{\text{RPA}}$  is the combined result of two ingredients: the independent-particle neutral excitations, as in  $\chi_0$ , and the collective plasmon excitations<sup>1</sup>. These two ingredients can be understood with the formula of the

<sup>1</sup>Here we do not take into account the fact that all quantities are matrices in reciprocal space. This is equivalent to saying that we neglect crystal local-field effects, which are expected to be small.

susceptibility in the random-phase approximation:

$$\chi_{\text{RPA}}(\mathbf{q}, \omega) = \frac{\chi_0(\mathbf{q}, \omega)}{1 + v_C(\mathbf{q})\chi_0(\mathbf{q}, \omega)}, \quad (9.1)$$

where  $v_C$  is the long-range Coulomb interaction. The spectrum for  $\chi_{\text{RPA}}$  involves its imaginary part, which is given by:

$$\text{Im } \chi_{\text{RPA}}(\mathbf{q}, \omega) = \frac{1}{v_C(\mathbf{q})} \frac{\text{Im } \epsilon_{\text{RPA}}(\mathbf{q}, \omega)}{(\text{Re } \epsilon_{\text{RPA}}(\mathbf{q}, \omega))^2 + (\text{Im } \epsilon_{\text{RPA}}(\mathbf{q}, \omega))^2}, \quad (9.2)$$

where we have introduced the dielectric function

$$\epsilon^{-1}(\mathbf{q}, \omega) = 1 - v_C(\mathbf{q})\chi(\mathbf{q}, \omega), \quad (9.3)$$

where  $\chi$  is the exact many-body susceptibility. Eq. (9.3) is an exact relation, defining the dielectric function. Within the random-phase approximation,  $\epsilon$  takes the expression:

$$\epsilon_{\text{RPA}}(\mathbf{q}, \omega) = 1 + v_C(\mathbf{q})\chi_0(\mathbf{q}, \omega). \quad (9.4)$$

Analysing Eq. (9.2), we see that a peak in the RPA susceptibility have two possible origins:

- A peak in  $\text{Im } \epsilon_{\text{RPA}}$ : these peaks have the same origin as the peaks in the non-interacting susceptibility, owing to Eq. (9.4);
- When  $\text{Im } \epsilon_{\text{RPA}}$  is small, a zero in  $\text{Re } \epsilon_{\text{RPA}}$ : these peaks are called plasmon peaks. They are collective excitations of the correlated electronic system.

We analyse the plasmons by plotting the dielectric function in Fig. 9.7. Typically, owing to the Kramers-Kronig relations, a zero in the real part of the dielectric function comes together with a set of peaks in the imaginary part. By analysing the real part of the dielectric function, we detect two plasmons. The first one is actually a set of sharp plasmons between 5 and 8 eV, which can be connected to the cobalt *3d* states. The second plasmon is more shallow and connects to the oxygen *2p* states.

These observations on the plasmons can be confirmed by plotting  $\text{Im } \chi_{\text{RPA}}(\mathbf{q}, \omega)$  for high-symmetry points, as in Fig. 9.8. Some remarks from the model study in Part II also apply here. The numerical values taken by  $\text{Im } \chi_{\text{RPA}}$  are around one order of magnitude less than  $\text{Im } \chi_0$ . The spectral weight is much reduced at low frequencies, between  $\omega = 0$  and 10 eV, where the non-interacting susceptibility has most of its weight. The two plasmons, detected by analysing  $\text{Re } \epsilon_{\text{RPA}}$ , are present in the spectrum of  $\chi_{\text{RPA}}$ . The plasmon at 8 eV is much sharper than the one at 22 eV.

Let us now discuss the  $\mathbf{q}$  dependence part of the RPA susceptibility, with  $\text{Re } \chi_{\text{RPA}}(\mathbf{q}, \omega = 0)$ . As evidenced with the frequency-dependence analysis, the values of the RPA suscep-

## 9.2. The susceptibility in the random-phase approximation (RPA): $\chi_{RPA}$

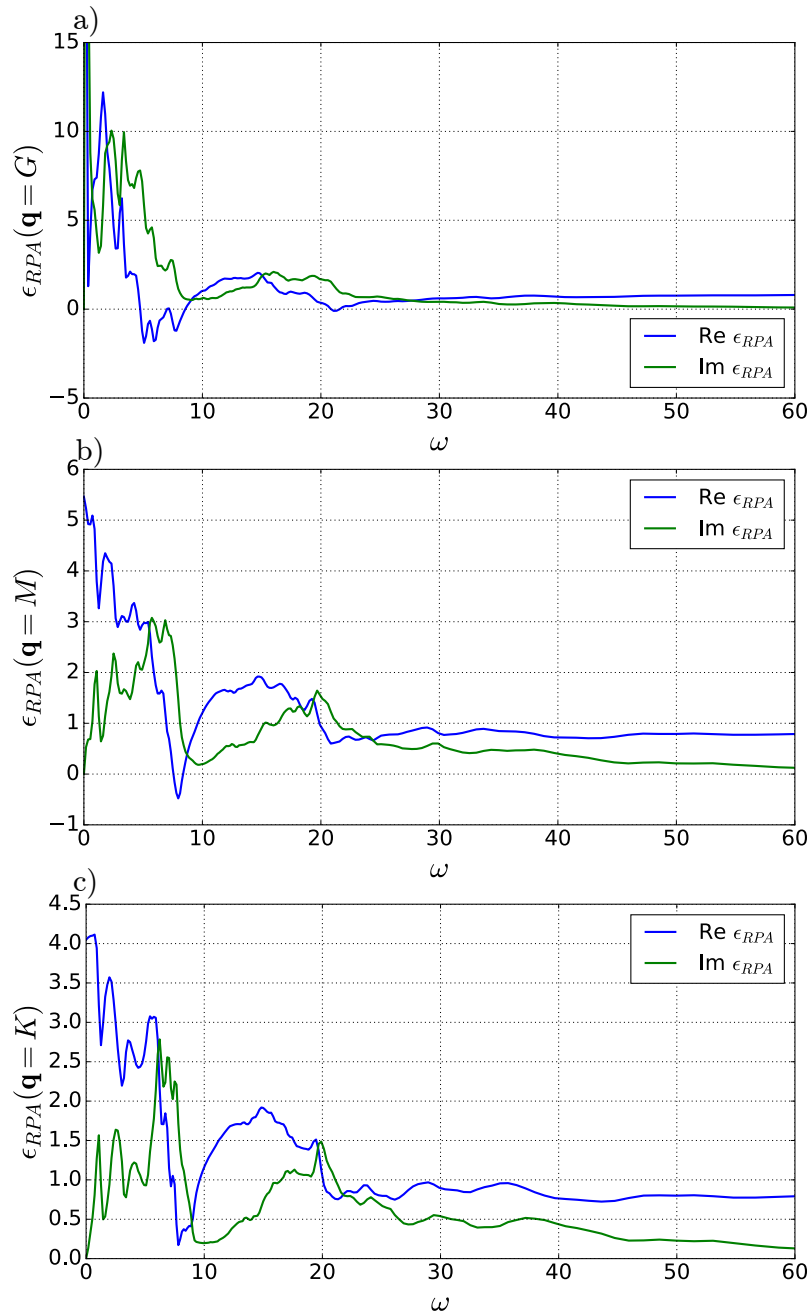
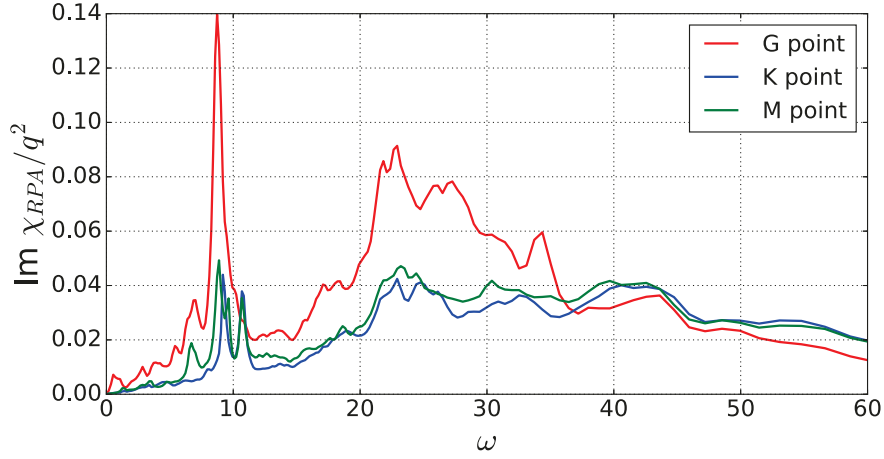
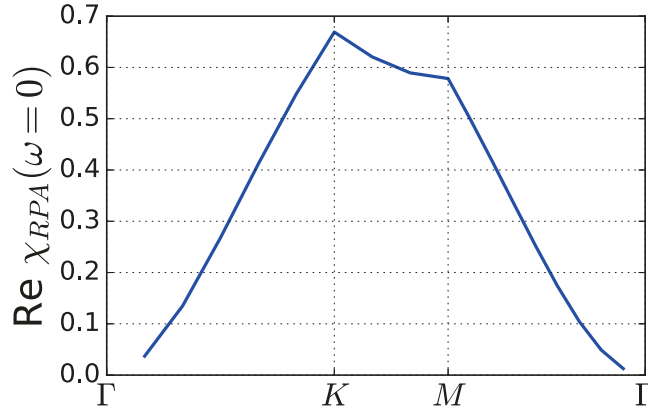


Figure 9.7: The computed *ab initio* RPA dielectric function at 3 different wavevectors  $\mathbf{q}$ . A peak in the imaginary part corresponds to a neutral independent-particle excitation. A plasmon can be detected as a zero in the real part of the dielectric function. In this system, there is a clear plasmon at frequency 8 eV for small  $\mathbf{q}$ . It can be related to the  $3d$  peaks in  $\chi_0$  at lower frequencies. Another, shallow plasmon is visible at 22 eV. It is a typical feature of many oxides and originates from the  $O(2p)$  states.


 Figure 9.8: Imaginary part of the computed *ab initio* RPA susceptibility.

 Figure 9.9: Zero-frequency component of the *ab initio* RPA susceptibility, on a  $\mathbf{q}$  path.

tibility are much reduced compared to their non-interacting counterparts, see Fig. 9.4. Another remark is that the  $\mathbf{q}$  dependence is different from what was observed in the non-interacting case. In the non-interacting case, the susceptibility was maximum at the  $M$ -point. Now, in RPA, the maximum is located at the  $K$ -point.

Hence, the choice of an approximation method (here, non-interacting or RPA) is important. It has a crucial impact on the frequency dependence of the susceptibility and also on the  $\mathbf{q}$  dependence. This is to be expected in extended systems, where the long-range Coulomb interaction gives rise to plasmons that are found at higher frequencies than the interband transitions.

### 9.2.2 Comparison to the model

We have shown in section 9.1.2 that the non-interacting susceptibility is well-reproduced by the model, provided that one restricts the transitions to the  $t_{2g}$  manifold in the *ab initio* calculation. Is it possible to connect the RPA susceptibilities of the model and the *ab initio* case, as well?

Similarly to Eq. (9.1), the RPA susceptibility on the model is computed from the non-interacting susceptibility, as:

$$\chi_{\text{RPA}}(\mathbf{q}, \omega) = \frac{\chi_0(\mathbf{q}, \omega)}{1 + v_{\mathbf{q}}\chi_0(\mathbf{q}, \omega)}, \quad (9.5)$$

where, on the model,  $v_{\mathbf{q}}$  is parametrised by  $U$  and  $V$ .  $U$  and  $V$  are partially screened Coulomb interaction terms. They are screened by all transitions that are not occurring inside the low-energy window. Compared to the bare Coulomb interaction, their values are hence much reduced. In the following, we estimate the values of  $U$  and  $V$  by performing a RPA calculation for both the model and the *ab initio* cases; then we fit the values of  $U$  and  $V$  such that the RPA susceptibilities for the two systems match.

This method can be better justified by making a connection to the constrained random-phase approximation (cRPA) [127, 128, 129]. cRPA splits the bands into low-energy bands (i.e., closest to the Fermi level; we call them  $d$  bands for simplicity; in our specific case they correspond to  $t_{2g}$ ) and high-energy bands (we call them  $p$  bands here, but these also include unoccupied and higher-energy bands). Following this, the total polarisation is split into:

$$P = P_{dd} + P_{\text{rest}}, \quad (9.6)$$

i.e., the contribution from the  $d$  bands only is taken apart. Now,  $P_{\text{rest}}$ , which mainly contains diagrams from high-energy processes, is approximated as its first-order, bubble diagram:

$$\begin{aligned} P_{\text{rest}} &\approx P_{\text{rest}}^0 \\ &= P_{pd}^0 + P_{pp}^0, \end{aligned} \quad (9.7)$$

which is the sum of  $pd$  components (connecting the  $p$  and  $d$  subspaces) and  $pp$  components (within the  $p$  subspace). Having split the polarisation function, the Dyson equation for the screened interaction:

$$W = v_C + v_C P W, \quad (9.8)$$

where  $v_C$  is the bare Coulomb interaction, can be split into:

$$\begin{cases} W_{\text{rest}} &= v_C + v_C(P_{pd}^0 + P_{pp}^0)W_{\text{rest}}, \\ W &= W_{\text{rest}} + W_{\text{rest}}P_{dd}W, \end{cases} \quad (9.9)$$

where we have introduced a partially-screened quantity,  $W_{\text{rest}}$ . According to the second line of Eq. (9.9), the effective interacting parameters of the model correspond to  $W_{\text{rest}}$ .  $W_{\text{rest}}$  is a partially screened Coulomb interaction: it is screened by all the high-energy bands. Furthermore, since  $P_{pd}^0 + P_{pp}^0$  is a non-local and a dynamical quantity, the resulting  $W_{\text{rest}}$  is in principle also non-local and dynamical.

In usual cRPA,  $W_{\text{rest}}$  is projected on Wannier orbitals. The static part of the result is then interpreted as  $U$  and  $V$ . Here, we take a different route. We compute the RPA susceptibility for both the model and the *ab initio* system. For the model, the RPA susceptibility is parametrised by  $U$  and  $V$ .

In the following, we fit  $U$  and  $V$  such that the RPA *ab initio* and model results best match. Since  $U$  and  $V$  account for the non-locality of the partial screening, we do this fit on the  $\mathbf{q}$  dependent component  $\text{Re } \chi_{\text{RPA}}(\mathbf{q}, \omega = 0)$ . The difference to cRPA is the following. In cRPA,  $V$  is the nearest-neighbour matrix element of  $W_{\text{rest}}$ . Here,  $U$  and  $V$  are effective parameters that simulate the overall behaviour of  $W_{\text{rest}}$  in an optimised way. Results for  $U$  and  $V$  will be different whenever  $W_{\text{rest}}$  is relatively long-ranged. The result for various  $U$  and  $V$  parameters is presented in Fig. 9.10. When varying the local  $U$  parameter, the model RPA susceptibility changes most at high momentum. When varying the non-local  $V$  parameter, the model RPA susceptibility changes most at low momentum.  $U$  being local and  $V$  non-local, means that  $U$  influences what happens at higher momentum than  $V$ , which is reasonable since small  $\mathbf{q}$  corresponds to large distances. As a result of Fig. 9.10, the optimal fit is  $U = 1.8$  and  $V = 0.5$ .

We now turn to the analysis of the frequency-dependence of the RPA susceptibility for the model. The real part of the dielectric function is displayed in Fig. 9.11 for various types of calculations. There are two groups of curves to be distinguished in Fig. 9.11. On the one hand, the model and the *ab initio* dielectric functions, where the *ab initio* results from intra- $t_{2g}$  transitions only, display a similar behaviour. This is to be expected since they originate from a similar  $\chi_0$ , see Fig. 9.5. A plasmon, corresponding to a zero-crossing of the real part of the dielectric function, appears between 1 eV and 1.5 eV. On the other hand, the *ab initio* curve obtained from transitions involving all the bands has a distinct behaviour. There, a plasmon is also expected, but at larger energies, around 9 eV.

Taking the optimised values  $U = 1.8$  and  $V = 0.5$ , we examine the frequency-dependence of the RPA susceptibilities. The model and *ab initio* susceptibilities are presented in Fig. 9.12. The *ab initio* susceptibility in Fig. 9.12 is computed for all bands. On the frequency axis, the two susceptibilities do not agree, as expected from the analysis of

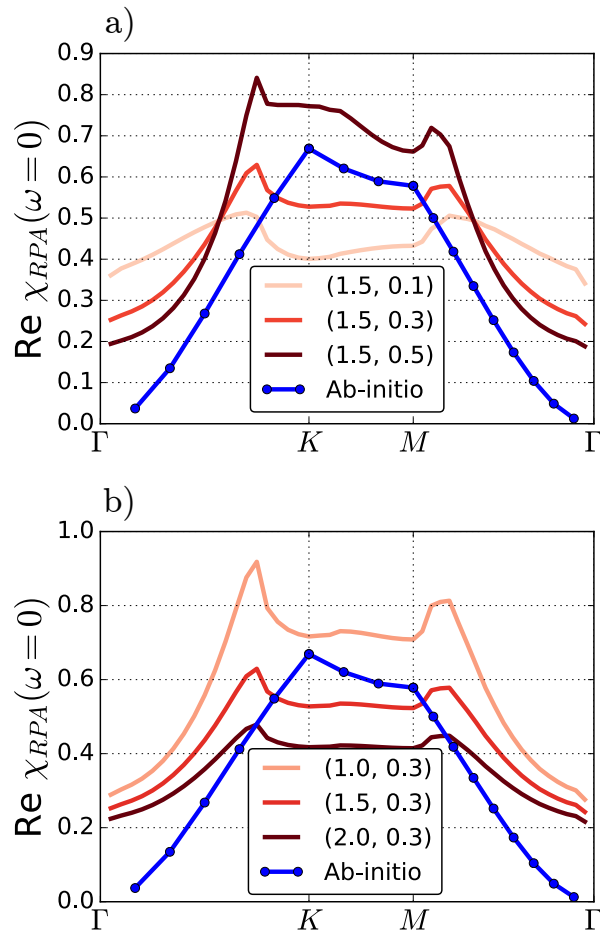


Figure 9.10: Zero-frequency component on the RPA susceptibility on a  $\mathbf{q}$  point path. Comparison between model and *ab initio* calculations, for various interaction parameters  $U$  and  $V$ . The interaction parameters are indicated in the legend, as the couple  $(U, V)$ . In panel a),  $U$  is fixed to the value 1.5; in panel b)  $V$  is fixed to the value 0.3.

Fig. 9.11. The model RPA susceptibility features a plasmon at low frequencies (close to 0 eV at small  $\mathbf{q}$ ; close to 2 eV for wavevectors at the edge of the reduced Brillouin zone). The *ab initio* susceptibility features a plasmon at higher frequency, around 9 eV. This strong disagreement in the frequency dependence, as opposed to the static picture of Fig. 9.10, can be traced back to the fact that  $U$  and  $V$  are static quantities. Their frequency dependence may be a crucial ingredient, if one wants to reproduce spectra.

### 9.3 Discussion

In this chapter, we have attempted to move one step forward in the *ab initio* prediction of many-body susceptibilities, in an effort to merge insights from a model treated by

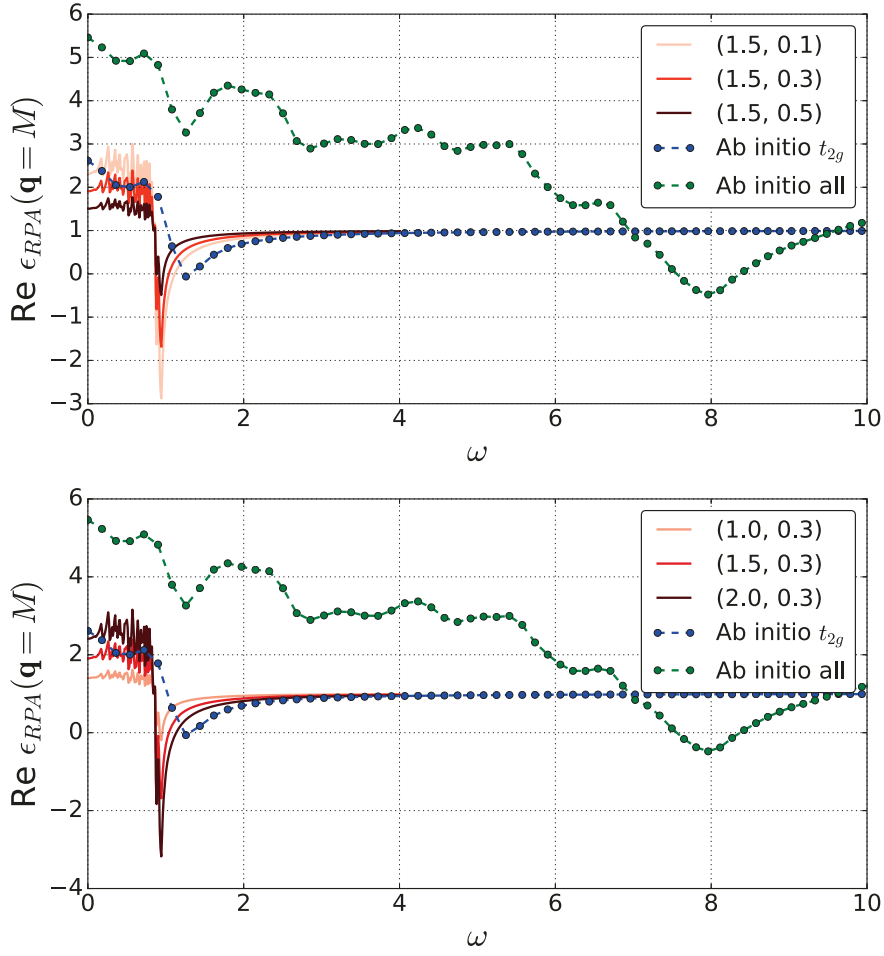


Figure 9.11: Real part of the RPA dielectric function for the model (full lines) and for the *ab initio* cases (dotted lines). For the model, various interaction parameters are used. The interaction parameters are indicated in the legend, as the couple  $(U, V)$ . For the *ab initio* two types of calculations are displayed: a calculation using only intra- $t_{2g}$  transitions and a calculation using all bands. The frequency at which  $\text{Re } \epsilon$  crosses zero corresponds to a plasmon.

non-perturbative methods and from an *ab initio* perspective on a material.

We have first shown that the non-interacting susceptibility of the  $t_{2g}$  manifold only could be well reproduced by the model extracted from Piefke *et al.* [121] (Fig. 9.5). The model hence describes well the low-energy side of the imaginary part of the non-interacting *ab initio* susceptibility. However, for the real part, due to the Kramers-Kronig relations, the model is not enough even at zero frequency and an all-band *ab initio* calculation is necessary (Fig. 9.6).

A RPA calculation for both the model and the *ab initio* systems allowed us to draw

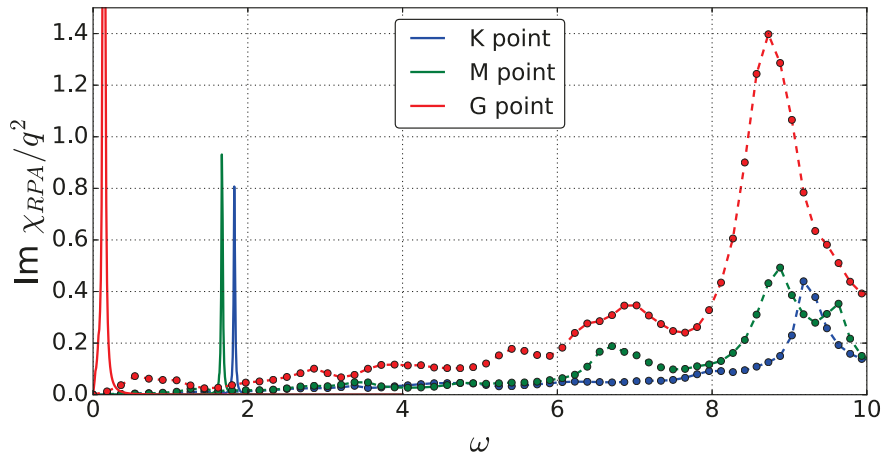


Figure 9.12: Imaginary part of the computed *ab initio* and model RPA susceptibilities. The model susceptibility was calculated assuming  $U = 1.8$ ,  $V = 0.5$ . Full line: model susceptibility. Dots: *ab initio* using all bands. The *ab initio* values are multiplied by a factor 10 for more visibility.

an estimate for the interaction parameters  $U$  and  $V$ , in a spirit similar to cRPA. This estimate amounts to  $U = 1.8$  eV and  $V = 0.5$  eV. This value of  $U$  is significantly smaller than the experimental estimate  $U = 5$  eV, deduced from the presence of a satellite at 11 eV in photoemission [55]. Also,  $V$  is rather large: it sets the system close to, or in the ordered phase of the phase diagram on Fig. 6.1. We thus have been able to couple a one-band model to an *ab initio* calculation.

In our *ab initio* calculations using the random-phase approximation, we found a plasmon at 9 eV. We showed that this plasmon cannot be reproduced by a static value of  $U$  using the model, as expected. The effect of a frequency dependent  $W(\mathbf{r}, \mathbf{r}', \omega)$  on low-energy observables was already found to be relevant in other contexts [153, 154, 155, 156, 157, 158]. In addition, we could speculate that the 11 eV satellite found in photoemission by Hasan *et al.* [55] could be connected to our 9 eV plasmon.

Now, it is still necessary to define a consistent way of merging the EDMFT observation that  $\chi \approx \chi_0$ , with an *ab initio* calculation. One possibility could be to split the polarisation between a high-frequency part, treated within RPA, and a low-frequency part, treated beyond the RPA and observed to be close to the non-interacting limit. In particular, this merge may have the important physical consequence that the 9 eV plasmon is modified.



## Conclusion **Part IV**



## 10 Conclusion and perspectives

In this work we have shown, using sodium cobaltates as a case study, how to gain insight from both a strongly-correlated and a first-principles perspective. Capturing the physical properties of  $\text{Na}_{2/3}\text{CoO}_2$  is challenging for both these approaches. Since they provide complementary results, these methodologies can be used as a combination to determine the active degrees of freedom in the cobaltates and how they interact.

In Part I, we have given an introduction to the field of correlated electronic systems and to some computational schemes.

In Part II, we have performed an Extended Dynamical Mean-Field Theory (EDMFT) study of an extended Hubbard model on a triangular lattice, which can be considered as a simplified model for the cobaltates. We have shown that exchange and correlation effects arise in different ways according to the observable one is looking at. For one-particle spectra, a lower Hubbard satellite is found at large local interaction  $U$ . Concerning two-particle (electron-hole) observables, we find a weak renormalisation of the charge susceptibility by correlations. This observation contrasts with results from the Random-Phase Approximation (RPA), where screening systematically reduces the charge susceptibility. High doping is a regime where the RPA, which contains only variations from the Hartree potential, has problems. Hence, it could be useful to design an alternative mean-field scheme specifically tailored for high doping, taking into account variations beyond Hartree. This could be considered in future work. Moreover, we found a region of the phase diagram with a negative static screened interaction. An effectively attractive screened interaction raises questions: What physical reality is hidden in this region? Is there a symmetry-broken phase? Some ingredients of this region are reminiscent of the Wigner transition: low carrier density and high interaction strength compared to the kinetic energy.

In Part III, we adopted an *ab initio* perspective to study a realistic electronic structure of the cobaltates. We analysed the Density-Functional Theory (DFT) band structure, focusing on detailed microscopic processes such as hopping and hybridisation of cobalt

with oxygen. We found that the  $a_{1g}$  and  $e_g$  cobalt-derived bands are the result of hopping processes via the oxygen atoms, while the  $e'_g$  bands result from a direct hopping between adjacent cobalt atoms. Furthermore, we analysed the effect of sodium doping. We saw that the main effect of a sodium atom was to lower local symmetries around its neighbouring cobalt or oxygen atom. Depending on the sodium position, a hole is created on an oxygen, or an electron is added to a cobalt, hence creating a charge disproportionation. This charge disproportionation spreads over both the cobalt and oxygen atoms. Finally, we studied the effect of correlations on *ab initio* susceptibilities. We systematically compared the susceptibilities from model and *ab initio* calculations, which led us to an estimate of a local  $U \approx 1.8$  eV and a nearest-neighbour  $V \approx 0.5$  eV. The *ab initio* results confirm the validity of the model in the low-frequency regime, whereas the model results suggest an approximation for the low-frequency part of the response function, that might be used in the *ab initio* context. Making a prediction for the susceptibilities, however, still requires to define how to consistently merge processes from different energy scales.

The findings listed above result from a general methodology, that can be applied to other systems. Each method employed above sheds a different light on the physics of cobaltates at high doping. However, more synergies can still be achieved. First, it is important to connect low-energy and high-energy calculations in a systematic way. This follows from renormalisation group ideas. Each energy window should be addressed with dedicated methods and approximations. A connector is needed to bridge the gap between the different results for the different energy scales. One possibility for such a consistent combination is the  $GW + \text{DMFT}$  scheme. Second, results from the strongly-correlated methodology can inspire new *ab initio* approximations in regimes away from half-filling. Third, the *ab initio* perspective is important to interpret microscopic processes. It helps to understand the hopping processes behind a band structure, and the screening processes behind the values of  $U$  and  $V$ .

This work opens up perspectives for the future. The *ab initio* calculations stressed the importance of the hybridisation of cobalt and oxygen. It could be instructive to include the oxygen states in the low-energy model. The most relevant non-local Coulomb interaction would then be the repulsion between cobalt and neighbouring oxygen electrons. Such a study could help to understand how specifically a kagomé superstructure can arise as a symmetry-broken state. Another point would be to elucidate the negative-screened-interaction region on the Hubbard model. In order to better understand the physical nature of this phase and the connections to a Wigner charge-ordered phase, further studies are needed, performing exact diagonalisation on small clusters containing few charge carriers. Finally, the *ab initio* analysis could be pursued, with the detailed description of additional microscopic processes such as the crystal local-field effects. A further analysis could be divided in terms of low- and high-energy, or long- and short-range electronic processes.

# Appendices





# A Conventions

## A.1 Notations

### A.1.1 Time and frequencies

- $\tau$  denotes the imaginary time variable,  $t$  the real time variable
- $\beta$  denotes the inverse temperature
- $\mathcal{T}$  denotes the real time ordering operator
- $\mathcal{T}_\tau$  denotes the imaginary time ordering operator
- $\omega$  denotes the real-axis frequency variable
- $i\omega_n = i\frac{(2n+1)\pi}{\beta}$  denotes a fermionic Matsubara frequency
- $i\nu_n = i\frac{2n\pi}{\beta}$  denotes a bosonic Matsubara frequency

### A.1.2 Space and momentum

- $\mathbf{k}$  and  $\mathbf{q}$  denote momentum variables for fermionic and bosonic quantities, respectively
- $\mathbf{R}_i$  denotes the position of a Wannier site
- $\mathbf{r}$  denotes a position in the continuum

### A.1.3 Operators

- $c^\dagger, c$  denote second-quantised creation and annihilation operators, respectively
- $c^*, c$  denote conjugate Grassmann variables corresponding to  $c^\dagger, c$

## Appendix A. Conventions

---

- $\mathcal{H}$  denotes a Hamiltonian
- $\Psi$  denotes a many-body state
- $v_C(\mathbf{q})$  denotes the bare Coulomb repulsion
- $v_{\mathbf{q}}$  denotes an effective Coulomb repulsion on a lattice

### A.1.4 Units

- Unless specified otherwise,  $\hbar = m_e = e^2 = 4\pi\epsilon_0 = 1$ .
- All energies are in electron-volts (eV).

## A.2 Fourier transforms

### A.2.1 Time-frequency domain

For real time and frequencies, the direct and inverse Fourier transforms are defined as:

$$\begin{aligned} f(\omega) &= \int_{-\infty}^{+\infty} dt e^{i\omega t} f(t), \\ f(t) &= \int_{-\infty}^{+\infty} \frac{d\omega}{2\pi} e^{-i\omega t} f(\omega). \end{aligned} \tag{A.1}$$

For any imaginary-time  $\beta$ -periodic or  $\beta$ -antiperiodic function  $f(\tau)$ , the direct and inverse Fourier transforms are defined as:

$$\begin{aligned} f(i\omega_n) &= \int_0^\beta d\tau f(\tau) e^{i\omega_n \tau}, \\ f(\tau) &= \frac{1}{\beta} \sum_{n=-\infty}^{\infty} f(i\omega_n) e^{-i\omega_n \tau}. \end{aligned} \tag{A.2}$$

### A.2.2 Space domain

In the continuum, in a crystal of volume  $\Omega$  with a periodic potential, the Fourier transform is defined as:

$$\begin{aligned} f(\mathbf{k} + \mathbf{G}) &= \int_{\Omega} d\mathbf{r} f(\mathbf{r}) e^{-i(\mathbf{k} + \mathbf{G}) \cdot \mathbf{r}}, \\ f(\mathbf{r}) &= \frac{1}{\Omega} \sum_{\mathbf{k}, \mathbf{G}} f(\mathbf{k} + \mathbf{G}) e^{i(\mathbf{k} + \mathbf{G}) \cdot \mathbf{r}}, \end{aligned} \tag{A.3}$$

where  $\mathbf{G}$  is a vector of the reciprocal lattice and  $\mathbf{k}$  belongs to the first Brillouin zone.

For a function  $f(\mathbf{R})$  defined on a Bravais lattice (BL), the direct and inverse Fourier transforms to the Brillouin zone (BZ) are defined as:

$$\begin{aligned} f(\mathbf{k}) &= \sum_{\mathbf{R}_i \in \text{BL}} e^{-i\mathbf{k}\mathbf{R}_i} f(\mathbf{R}_i), \\ f(\mathbf{R}_i) &= \frac{1}{N_{\mathbf{k}}} \sum_{\mathbf{k} \in \text{BZ}} e^{i\mathbf{k}\mathbf{R}_i} f(\mathbf{k}). \end{aligned} \quad (\text{A.4})$$

### A.3 Propagators

The zero-temperature time-ordered one-body Green's function in real time is defined as:

$$G(\mathbf{x}_1, t_1; \mathbf{x}_2, t_2) = -i \langle \Psi_0 | \mathcal{T} \hat{c}(\mathbf{x}_1, t_1) \hat{c}^\dagger(\mathbf{x}_2, t_2) | \Psi_0 \rangle, \quad (\text{A.5})$$

where  $\mathbf{x} = (\mathbf{r}, \sigma)$  and  $\Psi_0$  is the many-body ground-state of the system.

The corresponding Lehmann representation is

$$\begin{aligned} G(\mathbf{x}_1, \mathbf{x}_2, \omega) &= \sum_{A^{(N+1)}} \frac{\langle \Psi_0 | \hat{c}(\mathbf{x}_1) | \Psi_A^{(N+1)} \rangle \langle \Psi_A^{(N+1)} | \hat{c}^\dagger(\mathbf{x}_2) | \Psi_0 \rangle}{\omega - (E_A^{(N+1)} - E_0) + i\eta} \\ &+ \sum_{B^{(N-1)}} \frac{\langle \Psi_B^{(N-1)} | \hat{c}(\mathbf{x}_1) | \Psi_0 \rangle \langle \Psi_0 | \hat{c}^\dagger(\mathbf{x}_2) | \Psi_B^{(N-1)} \rangle}{\omega - (E_0 - E_B^{(N-1)}) - i\eta}. \end{aligned} \quad (\text{A.6})$$

It is obtained by introducing a complete set of states in Eq. (A.5) and using the formula:

$$\theta(t) = - \int_{-\infty}^{+\infty} \frac{d\omega}{2\pi} \frac{e^{-i\omega t}}{\omega + i\eta}, \quad \eta = 0^+. \quad (\text{A.7})$$

The finite-temperature time-ordered Green's function on a lattice is defined in imaginary-time as:

$$G_{ij}(\tau) = - \langle \mathcal{T}_\tau c_i(\tau) c_j^\dagger(0) \rangle. \quad (\text{A.8})$$

The corresponding Lehmann representation is

$$G(\mathbf{k}, i\omega_n) = \frac{1}{Z_G} \sum_{a,b} |\langle a | c_{\mathbf{k}} | b \rangle|^2 \frac{e^{-\beta E'_a} + e^{-\beta E'_b}}{i\omega_n + E'_a - E'_b}, \quad (\text{A.9})$$

where  $Z_G$  is the partition function;  $a$  are eigenstates of the system with energy  $E_a$  and number of particles  $N_a$  (with  $E'_a = E_a - \mu N_a$ ).



# B The cobalt $3d$ orbitals in the octahedral environment

## B.1 Rotation of the $3d$ orbitals

Conventionally,  $e_g$  and  $t_{2g}$  orbitals are referenced in a basis with octahedral symmetry with axes pointing towards the edges of the octahedron. In VASP, we use a rotated frame, most convenient to treat the triangular planes. We want to express our  $3d$  orbitals in this rotated frame.

$X, Y, Z$  denote coordinates in the octahedral frame;  $x, y, z$  denote coordinates in the rotated frame. The rotation matrices are expressed as:

$$O = \begin{pmatrix} 1/\sqrt{2} & 0 & -1/\sqrt{2} \\ -1/\sqrt{6} & 2/\sqrt{6} & -1/\sqrt{6} \\ 1/\sqrt{3} & 1/\sqrt{3} & 1/\sqrt{3} \end{pmatrix}, \quad O^{-1} = \begin{pmatrix} 1/\sqrt{2} & -1/\sqrt{6} & 1/\sqrt{3} \\ 0 & 2/\sqrt{6} & 1/\sqrt{3} \\ -1/\sqrt{2} & -1/\sqrt{6} & 1/\sqrt{3} \end{pmatrix}. \quad (\text{B.1})$$

For a given point  $M$  in space with coordinates  $(x_M, y_M, z_M)$  in the rotated frame:

$$\begin{aligned} OM &= x_M \mathbf{e}_x + y_M \mathbf{e}_y + z_M \mathbf{e}_z \\ &= \left( \frac{x_M}{\sqrt{2}} - \frac{y_M}{\sqrt{6}} + \frac{z_M}{\sqrt{3}} \right) \mathbf{e}_X + \left( \frac{y_M \sqrt{2}}{\sqrt{3}} + \frac{z_M}{\sqrt{3}} \right) \mathbf{e}_Y + \left( -\frac{x_M}{\sqrt{2}} - \frac{y_M}{\sqrt{6}} + \frac{z_M}{\sqrt{3}} \right) \mathbf{e}_Z, \end{aligned} \quad (\text{B.2})$$

yielding the following coordinates in the octahedral frame:

$$\begin{aligned} X_M &= \frac{x_M}{\sqrt{2}} - \frac{y_M}{\sqrt{6}} + \frac{z_M}{\sqrt{3}}, \\ Y_M &= \frac{y_M \sqrt{2}}{\sqrt{3}} + \frac{z_M}{\sqrt{3}}, \\ Z_M &= -\frac{x_M}{\sqrt{2}} - \frac{y_M}{\sqrt{6}} + \frac{z_M}{\sqrt{3}}. \end{aligned} \quad (\text{B.3})$$

## Appendix B. The cobalt 3d orbitals in the octahedral environment

---

In the octahedral environment, the 3d orbitals split into the  $t_{2g}$  and the  $e_g$  manifolds. The  $t_{2g}$  manifold is spanned by the vectors  $d_{XY}$ ,  $d_{YZ}$  and  $d_{ZX}$ . Due to the compression of the oxygen octahedra along the  $c$ -axis, the  $t_{2g}$  manifold further splits into one  $a_{1g}$  (symmetric) state and two  $e'_g$  states:

$$a_{1g} : \quad \frac{1}{\sqrt{3}} (d_{XY} + d_{YZ} + d_{ZX}) \quad (\text{B.4})$$

$$e'_g : \quad \frac{1}{\sqrt{3}} \left( d_{XY} + e^{\pm \frac{2i\pi}{3}} d_{YZ} + e^{\mp \frac{2i\pi}{3}} d_{ZX} \right) \quad (\text{B.5})$$

As an example, let us compute explicitly the  $a_{1g}$  state in the rotated basis:

$$\begin{aligned} a_{1g} &= \frac{1}{\sqrt{3}} (d_{XY} + d_{YZ} + d_{ZX}) \\ &\sim \frac{1}{\sqrt{3}} (|XY\rangle + |YZ\rangle + |ZX\rangle) \\ &= \frac{1}{\sqrt{3}} \left[ \left( \frac{x_M}{\sqrt{2}} - \frac{y_M}{\sqrt{6}} + \frac{z_M}{\sqrt{3}} \right) \left( \frac{y_M\sqrt{2}}{\sqrt{3}} + \frac{z_M}{\sqrt{3}} \right) \right. \\ &\quad + \left( \frac{y_M\sqrt{2}}{\sqrt{3}} + \frac{z_M}{\sqrt{3}} \right) \left( -\frac{x_M}{\sqrt{2}} - \frac{y_M}{\sqrt{6}} + \frac{z_M}{\sqrt{3}} \right) \\ &\quad \left. + \left( -\frac{x_M}{\sqrt{2}} - \frac{y_M}{\sqrt{6}} + \frac{z_M}{\sqrt{3}} \right) \left( \frac{x_M}{\sqrt{2}} - \frac{y_M}{\sqrt{6}} + \frac{z_M}{\sqrt{3}} \right) \right] \\ &= \frac{1}{2\sqrt{3}} [2z_M^2 - (x_M^2 + y_M^2)] \\ &\sim d_{z^2}. \end{aligned} \quad (\text{B.6})$$

Thus, in the rotated basis, the  $a_{1g}$  state corresponds to a  $d_{z^2}$  state. With a similar derivation we find for the  $e'_g$  states:

$$\begin{aligned} &\frac{1}{\sqrt{3}} \left( d_{XY} + e^{2i\pi/3} d_{YZ} + e^{-2i\pi/3} d_{ZX} \right) \\ &= -\frac{e^{-2i\pi/3}}{\sqrt{3}} d_{x^2-y^2} + \frac{e^{-i\pi/6}}{\sqrt{3}} d_{xy} - \frac{e^{-2i\pi/3}}{\sqrt{6}} d_{yz} + \frac{e^{-i\pi/6}}{\sqrt{6}} d_{zx}, \end{aligned} \quad (\text{B.7})$$

and

$$\begin{aligned} &\frac{1}{\sqrt{3}} \left( d_{XY} + e^{-2i\pi/3} d_{YZ} + e^{2i\pi/3} d_{ZX} \right) \\ &= -\frac{e^{+2i\pi/3}}{\sqrt{3}} d_{x^2-y^2} + \frac{e^{+i\pi/6}}{\sqrt{3}} d_{xy} - \frac{e^{+2i\pi/3}}{\sqrt{6}} d_{yz} + \frac{e^{+i\pi/6}}{\sqrt{6}} d_{zx}. \end{aligned} \quad (\text{B.8})$$

The two previous expressions for the  $e'_g$  states, Eqs. B.7B.8, can be combined to yield

real-valued orbitals. The  $e'_g$  states are thus spanned by the two real-valued vectors:

$$\frac{1}{\sqrt{6}}d_{x^2-y^2} + \frac{1}{\sqrt{2}}d_{xy} + \frac{1}{2\sqrt{3}}d_{yz} + \frac{1}{2}d_{zx}, \quad (\text{B.9})$$

$$\frac{1}{\sqrt{2}}d_{x^2-y^2} - \frac{1}{\sqrt{6}}d_{xy} + \frac{1}{2}d_{yz} + \frac{1}{2\sqrt{3}}d_{zx}. \quad (\text{B.10})$$

The  $e_g$  states are spanned by the vectors  $d_{X^2-Y^2}$  and  $d_{Z^2}$ , which take the following expressions in the rotated basis:

$$d_{X^2-Y^2} = \frac{1}{2}d_{x^2-y^2} - \frac{1}{2\sqrt{3}}d_{xy} - \frac{1}{\sqrt{2}}d_{yz} + \frac{1}{\sqrt{6}}d_{zx}, \quad (\text{B.11})$$

$$d_{Z^2} = \frac{1}{2\sqrt{3}}d_{x^2-y^2} + \frac{1}{2}d_{xy} - \frac{1}{\sqrt{6}}d_{yz} - \frac{1}{\sqrt{2}}d_{zx}. \quad (\text{B.12})$$

As a conclusion, the 3d orbitals take the following expressions in the rotated frame:

$$a_{1g} : \quad \quad \quad d_{z^2}, \quad (\text{B.13a})$$

$$e'_{g1} : \quad \quad \quad \frac{1}{\sqrt{6}}d_{x^2-y^2} + \frac{1}{\sqrt{2}}d_{xy} + \frac{1}{2\sqrt{3}}d_{yz} + \frac{1}{2}d_{zx}, \quad (\text{B.13b})$$

$$e'_{g2} : \quad \quad \quad \frac{1}{\sqrt{2}}d_{x^2-y^2} - \frac{1}{\sqrt{6}}d_{xy} + \frac{1}{2}d_{yz} + \frac{1}{2\sqrt{3}}d_{zx}, \quad (\text{B.13c})$$

$$e_{g1} : \quad \quad \quad \frac{1}{2}d_{x^2-y^2} - \frac{1}{2\sqrt{3}}d_{xy} - \frac{1}{\sqrt{2}}d_{yz} + \frac{1}{\sqrt{6}}d_{zx}, \quad (\text{B.13d})$$

$$e_{g2} : \quad \quad \quad \frac{1}{2\sqrt{3}}d_{x^2-y^2} + \frac{1}{2}d_{xy} - \frac{1}{\sqrt{6}}d_{yz} - \frac{1}{\sqrt{2}}d_{zx}. \quad (\text{B.13e})$$

## B.2 Model for the $\text{Co}(a_{1g})\text{-O}$ hybridised complex

We want to give a meaning to the  $a_{1g}$  orbital, which is hybridised with the oxygen, and to its band dispersion featuring an effective negative nearest-neighbour hopping.

Let us consider a 3-atom model composed of two  $d_{z^2}$  orbitals and a  $p_z$  orbital in-between, in a  $120^\circ$ -configuration, similarly as in the actual cobalt planes. This model is depicted in Fig. ??.

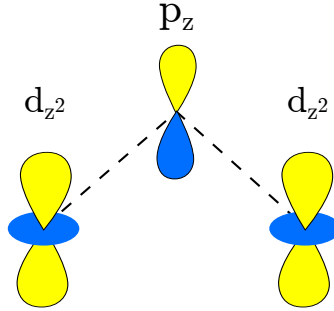


Figure B.1: Schematic figure of a Co - O - Co hybridised complex. The cobalt atoms contribute with a  $d_{z^2}$  orbital, while the oxygen atom contributes with a  $p_z$  orbital. The sign of the wavefunction is indicated with a blue or yellow colour. In the real material, the oxygen atoms are located above and below the cobalt plane. Here, in particular, we sketch a combination leading to the state  $a_{1g}(\Gamma)$ , which is an antibonding combination of the constituting atomic orbitals.

The system is a charge-transfer system. We fix the local level of the  $d_{z^2}$  orbitals to 0, and the local level of  $p_z$  to  $-\Delta$ . We consider hopping between neighbouring orbitals (i.e., from  $d_{z^2}$  to  $p_z$ ), of amplitude  $t$ . The corresponding Hamiltonian, in the basis  $(d_{z_1^2}, p_z, d_{z_2^2})$ , reads:

$$\mathcal{H} = \begin{pmatrix} 0 & -t & 0 \\ -t & -\Delta & -t \\ 0 & -t & 0 \end{pmatrix}. \quad (\text{B.14})$$

There are 3 eigenvalues to this Hamiltonian:

$$\text{Sp}(\mathcal{H}) = \left\{ -\frac{\Delta}{2} - \frac{\sqrt{\Delta^2 + 8t^2}}{2} ; 0 ; -\frac{\Delta}{2} + \frac{\sqrt{\Delta^2 + 8t^2}}{2} \right\} \quad (\text{B.15})$$

The lowest eigenvalue (denoted  $E_-$ ) corresponds to the eigenvector:

$$|\psi_0\rangle = \frac{t}{\sqrt{2t^2 + E_-^2}}(d_{z_1^2} + d_{z_2^2}) - \frac{E_-}{\sqrt{2t^2 + E_-^2}}p_z, \quad (\text{B.16})$$

## B.2. Model for the $\text{Co}(a_{1g})\text{-O}$ hybridised complex

---

which has most of its weight on the oxygen, and which is in a bonding configuration between the oxygen and the cobalt. In the real system, this corresponds to the oxygen  $p_z$  state.

The next eigenvalue, 0, corresponds to the eigenvector:

$$|\psi_1\rangle = \frac{1}{\sqrt{2}}(d_{z_1^2} - d_{z_2^2}). \quad (\text{B.17})$$

This state has no hybridisation to the oxygen. It is antibonding, with a node between the two cobalts. In the real system, this corresponds to the state  $a_{1g}(K)$ .

The highest eigenvalue (denoted  $E_+$ ) corresponds to the eigenvector:

$$|\psi_2\rangle = \frac{t}{\sqrt{2t^2 + E_+^2}}(d_{z_1^2} + d_{z_2^2}) - \frac{E_+}{\sqrt{2t^2 + E_+^2}}p_z, \quad (\text{B.18})$$

which has mostly cobalt character, with an antibonding hybridisation with the oxygens. In the real cobaltates, this corresponds to the state  $a_{1g}(\Gamma)$ .



# C Negative screening in the Hubbard dimer

We show that a negative static screening is not an artifact of the EDMFT approximation, but can happen as a physical fact. We exemplify this on an exactly solvable model.

Let us define the Hubbard dimer at 1/4-filling via the Hamiltonian:

$$H = U \sum_{i=1,2} n_{i\uparrow} n_{i\downarrow} - t \sum_{\sigma} (c_{1\sigma}^{\dagger} c_{2\sigma} + c_{2\sigma}^{\dagger} c_{1\sigma}) - \mu \sum_i n_i, \quad (\text{C.1})$$

where  $\mu$  is chosen such as to have 1 electron per dimer.

The charge susceptibility can be computed exactly. On the Matsubara axis, the local (diagonal) component is:

$$\begin{aligned} \chi_{11}(i\nu_n) &= \frac{1}{4} \left[ \frac{1}{i\nu_n - 2t} - \frac{1}{i\nu_n + 2t} \right] \\ &= -\frac{t}{\nu_n^2 + 4t^2}. \end{aligned} \quad (\text{C.2})$$

This is a lorentzian centered around 0. The value at the Matsubara frequency  $\nu_n = 0$  is:

$$\chi_{11}(i\nu_n = 0) = -\frac{1}{4t}, \quad (\text{C.3})$$

which goes to infinity when  $t \rightarrow 0$ . With the formula  $W_{ij} = v_{ij} + v_{ik}\chi_{kl}v_{lj}$ , we find that for  $\nu_n = \omega = 0$ :

$$W_{11}(\omega = 0) = W_{\text{loc}}(\omega = 0) = U - \frac{U^2}{4t}, \quad (\text{C.4})$$

which becomes negative as soon as  $U/(4t) > 1$ . Hence, the fact that the local part of  $W$  becomes negative is not an artifact of an approximation. It happens in our exactly-solvable model.

We find that, for the off-diagonal element of the susceptibility:  $\chi_{12} = -\chi_{11}$ . From this,

## Appendix C. Negative screening in the Hubbard dimer

---

the local part of the polarisation can be computed:

$$P_{loc} = -\frac{\chi_{11}}{1 - 2U\chi_{11}}. \quad (\text{C.5})$$

Notice the factor  $2U$  in the denominator. When  $\chi_{loc}$  grows big, then  $P_{loc}$  develops a pole, which is exactly what is detected in our EDMFT study.

# D Susceptibilities

## D.1 Analytical expressions

In linear-response theory, the variation of the expectation value of an observable  $\hat{O}$  when applying a small perturbation that couples a field  $F$  to a probe  $\hat{P}$  is given by the Kubo formula at zero-temperature:

$$\chi_{OP}(\mathbf{r}_1, t_1; \mathbf{r}_2, t_2) = \frac{\delta \langle \hat{O}(\mathbf{r}_1, t_1) \rangle}{\delta F(\mathbf{r}_2, t_2)} = -i\theta(t_1 - t_2) \langle \Psi_0 | [\hat{O}(\mathbf{r}_1, t_1) \hat{P}(\mathbf{r}_2, t_2)] | \Psi_0 \rangle, \quad (\text{D.1})$$

where the expectation value corresponds to the unperturbed Hamiltonian and  $\Psi_0$  is the ground many-body state. A divergence of the static susceptibility means that any arbitrarily small applied field induces a finite change in the observable  $O$ . A divergence of the static susceptibility corresponds by definition to a second-order phase transition. The particular case with which we deal in this thesis is the charge susceptibility, corresponding to the correlator  $\chi_{OP}$  with  $O = P = n$ .

Inserting a completeness relation and taking the Fourier transform, one derives the Lehmann representation:

$$\chi(\mathbf{r}_1, \mathbf{r}_2, \omega) = \sum_{A^{(N)}} \left[ \frac{\langle \Psi_0 | n(\mathbf{r}_1) | \Psi_A \rangle \langle \Psi_A | n(\mathbf{r}_2) | \Psi_0 \rangle}{\omega + E_0 - E_A + i\eta} - \frac{\langle \Psi_A | n(\mathbf{r}_1) | \Psi_0 \rangle \langle \Psi_0 | n(\mathbf{r}_2) | \Psi_A \rangle}{\omega + E_A - E_0 + i\eta} \right], \quad (\text{D.2})$$

which has poles at neutral-excitation energies, corresponding to transitions from the ground state to an excited state with  $N$  electrons.

The susceptibility is causal. Hence, it is analytic in the complex upper half-plane. A relationship can be derived using Cauchy's r esidus theorem, connecting the real and

## Appendix D. Susceptibilities

---

imaginary parts of  $\chi$ . This is the Kramers-Kronig relation:

$$\text{Re } \chi(\omega) = \frac{1}{\pi} \int_{-\infty}^{+\infty} d\omega' \frac{\text{Im } \chi(\omega')}{\omega' - \omega}, \quad (\text{D.3})$$

$$\text{Im } \chi(\omega) = -\frac{1}{\pi} \int_{-\infty}^{+\infty} d\omega' \frac{\text{Re } \chi(\omega')}{\omega' - \omega}. \quad (\text{D.4})$$

For some simple systems, the susceptibility in the absence of interactions (the non-interacting susceptibility) is given by the Lindhard formula. For the case of a single-band model on a lattice, we use the following expression:

$$\chi^0(\mathbf{q}, z) = \frac{1}{N_{\mathbf{k}}} \sum_{\mathbf{k}} \frac{n_F(\epsilon_{\mathbf{k}+\mathbf{q}}) - n_F(\epsilon_{\mathbf{k}})}{z - (\epsilon_{\mathbf{k}+\mathbf{q}} - \epsilon_{\mathbf{k}})}, \quad (\text{D.5})$$

where  $n_F$  is the Fermi-Dirac distribution function,  $N_{\mathbf{k}}$  is the number of  $\mathbf{k}$ -points in the grid and  $\epsilon_{\mathbf{k}}$  denotes a single-particle energy. On the real axis, one takes  $z = \omega + i\eta$ ,  $\eta = 0^+$ ; on the imaginary axis  $z = i\nu_n$ .

For the case of the continuum, we use the following formula involving one-particle states (in our case Kohn-Sham states) [159, 160]:

$$\begin{aligned} \chi_{\mathbf{G}\mathbf{G}'}^0(\mathbf{q}, \omega) &= \frac{2}{\Omega} \sum_{n, n', \mathbf{k}} (n_F(\epsilon_{n'\mathbf{k}+\mathbf{q}}) - n_F(\epsilon_{n\mathbf{k}})) \\ &\times \frac{\langle \psi_{n'\mathbf{k}+\mathbf{q}} | e^{i(\mathbf{q}+\mathbf{G})\mathbf{r}} | \psi_{n\mathbf{k}} \rangle \langle \psi_{n\mathbf{k}} | e^{-i(\mathbf{q}+\mathbf{G}')\mathbf{r}'} | \psi_{n'\mathbf{k}+\mathbf{q}} \rangle}{\omega - (\epsilon_{n'\mathbf{k}+\mathbf{q}} - \epsilon_{n\mathbf{k}}) + i\eta}. \end{aligned} \quad (\text{D.6})$$

Here  $\psi$  is a one-particle state. In this thesis we have worked with  $\mathbf{G} = \mathbf{G}' = 0$ , which reduced the susceptibilities to scalar quantities.

# Bibliography

- [1] Claude Fouassier, Guy Matejka, Jean-Maurice Reau, and Paul Hagenmuller. Sur de nouveaux bronzes oxygénés de formule  $\text{Na}_x\text{CoO}_2$ . le système cobalt-oxygène-sodium. *Journal of Solid State Chemistry*, 6(4):532 – 537, 1973.
- [2] I. Terasaki, Y. Sasago, and K. Uchinokura. Large thermoelectric power in  $\text{NaCo}_2\text{O}_4$  single crystals. *Phys. Rev. B*, 56:R12685–R12687, Nov 1997.
- [3] Kazunori Takada, Hiroya Sakurai, Eiji Takayama-Muromachi, Fujio Izumi, Ruben A. Dilanian, and Takayoshi Sasaki. Superconductivity in two-dimensional  $\text{CoO}_2$  layers. *Nature*, 422:53–55, March 2003.
- [4] Philip W Anderson. More is different. *Science*, 177(4047):393–396, 1972.
- [5] Kenneth G. Wilson. The renormalization group and critical phenomena. *Rev. Mod. Phys.*, 55:583–600, Jul 1983.
- [6] P. Hohenberg and W. Kohn. Inhomogeneous electron gas. *Phys. Rev.*, 136:B864–B871, Nov 1964.
- [7] W. Kohn and L. J. Sham. Self-consistent equations including exchange and correlation effects. *Phys. Rev.*, 140:A1133–A1138, Nov 1965.
- [8] Giovanni Onida, Lucia Reining, and Angel Rubio. Electronic excitations: density-functional versus many-body green’s-function approaches. *Rev. Mod. Phys.*, 74:601–659, Jun 2002.
- [9] Antoine Georges, Gabriel Kotliar, Werner Krauth, and Marcelo J. Rozenberg. Dynamical mean-field theory of strongly correlated fermion systems and the limit of infinite dimensions. *Rev. Mod. Phys.*, 68:13–125, Jan 1996.
- [10] H. Alloul, I. R. Mukhamedshin, T. A. Platova, and A. V. Dooglav. Na ordering imprints a metallic kagomé lattice onto the  $\text{Co}$  planes of  $\text{Na}_{2/3}\text{CoO}_2$ . *EPL (Europhysics Letters)*, 85(4):47006, 2009.
- [11] Charles Kittel. *Introduction to Solid State Physics*. John Wiley & Sons, 1966.

## Bibliography

---

- [12] David Pines and Philippe Nozières. *The Theory of Quantum Liquids*. Perseus, 1999.
- [13] Antoine Georges. Strongly correlated electron materials: Dynamical mean-field theory and electronic structure. In A. Avella and F. Mancini, editors, *Lectures on the physics of highly correlated electron systems VIII*, volume 715 of *Troisième cycle de la Suisse Romande, EPFL, 2002*, pages 3–74. AIP Conference Proceedings, March 2004. arXiv:cond-mat/0403123.
- [14] Masatoshi Imada, Atsushi Fujimori, and Yoshinori Tokura. Metal-insulator transitions. *Rev. Mod. Phys.*, 70:1039–1263, Oct 1998.
- [15] LD Landau. The theory of a fermi liquid. *Sov. Phys. JETP*, 3(1):920–925, 1957.
- [16] LD Landau. Oscillations in a fermi liquid. *Sov. Phys. JETP*, 5(1):101–108, 1957.
- [17] LD Landau. On the theory of the fermi liquid. *Sov. Phys. JETP*, 8(1):70–74, 1959.
- [18] Andrea Damascelli, Zahid Hussain, and Zhi-Xun Shen. Angle-resolved photoemission studies of the cuprate superconductors. *Rev. Mod. Phys.*, 75:473–541, Apr 2003.
- [19] J. H. de Boer and E. J. W. Verwey. Semi-conductors with partially and with completely filled 3d-lattice bands. *Proc. Phys. Soc.*, 49(4S):59, 1937.
- [20] N. F. Mott and R. Peierls. Discussion of the paper by de boer and verwey. *Proc. Phys. Soc.*, 49(4S):72, 1937.
- [21] J. Hubbard. Electron correlations in narrow energy bands. *Proc. Roy. Soc. (London) A*, 276(1365):238, 1963.
- [22] J. Hubbard. Electron correlations in narrow energy bands. ii. the degenerate band case. *Proc. Roy. Soc. (London) A*, 277(1369):237, 1964.
- [23] J. Hubbard. Electron correlations in narrow energy bands. iii. an improved solution. *Proc. Roy. Soc. (London) A*, 281(1386):401, 1964.
- [24] Junjiro Kanamori. Electron correlation and ferromagnetism of transition metals. *Progress of Theoretical Physics*, 30(3):275–289, 1963.
- [25] Martin C Gutzwiller. Effect of correlation on the ferromagnetism of transition metals. *Physical Review Letters*, 10(5):159, 1963.
- [26] Antoine Georges and Gabriel Kotliar. Hubbard model in infinite dimensions. *Phys. Rev. B*, 45:6479–6483, Mar 1992.
- [27] Olivier Parcollet, Michel Ferrero, Thomas Ayral, Hartmut Hafermann, Priyanka Seth, and I S Krivenko. TRIQS: The Toolbox for Research in Interacting Quantum Systems. *Computer Physics Communications*, 196:398, 2015.

- [28] A. Fujimori, I. Hase, H. Namatame, Y. Fujishima, Y. Tokura, H. Eisaki, S. Uchida, K. Takegahara, and F. M. F. de Groot. Evolution of the spectral function in mott-hubbard systems with  $d^1$  configuration. *Phys. Rev. Lett.*, 69:1796–1799, Sep 1992.
- [29] J. G. Bednorz and K. A. Müller. Possible hightc superconductivity in the ba-la-cu-o system. *Zeitschrift für Physik B Condensed Matter*, 64(2):189–193, 1986.
- [30] M. K. Wu, J. R. Ashburn, C. J. Torng, P. H. Hor, R. L. Meng, L. Gao, Z. J. Huang, Y. Q. Wang, and C. W. Chu. Superconductivity at 93 k in a new mixed-phase y-ba-cu-o compound system at ambient pressure. *Phys. Rev. Lett.*, 58:908–910, Mar 1987.
- [31] J. Wang, J. B. Neaton, H. Zheng, V. Nagarajan, S. B. Ogale, B. Liu, D. Viehland, V. Vaithyanathan, D. G. Schlom, U. V. Waghmare, N. A. Spaldin, K. M. Rabe, M. Wuttig, and R. Ramesh. Epitaxial bifeo<sub>3</sub> multiferroic thin film heterostructures. *Science*, 299(5613):1719–1722, 2003.
- [32] T. Kimura, T. Goto, H. Shintani, K. Ishizaka, T. Arima, and Y. Tokura. Magnetic control of ferroelectric polarization. *Nature*, 426(6962):55–58, 11 2003.
- [33] N. Hur, S. Park, P. A. Sharma, J. S. Ahn, S. Guha, and S-W. Cheong. Electric polarization reversal and memory in a multiferroic material induced by magnetic fields. *Nature*, 429(6990):392–395, 05 2004.
- [34] A P Ramirez. Colossal magnetoresistance. *Journal of Physics: Condensed Matter*, 9(39):8171, 1997.
- [35] Lide M. Rodriguez-Martinez and J. Paul Attfield. Cation disorder and size effects in magnetoresistive manganese oxide perovskites. *Phys. Rev. B*, 54:R15622–R15625, Dec 1996.
- [36] S. Middey, J. Chakhalian, P. Mahadevan, J.W. Freeland, A.J. Millis, and D.D. Sarma. Physics of ultrathin films and heterostructures of rare-earth nickelates. *Annual Review of Materials Research*, 46(1):305–334, 2016.
- [37] E. Pavarini, S. Biermann, A. Poteryaev, A. I. Lichtenstein, A. Georges, and O. K. Andersen. Mott transition and suppression of orbital fluctuations in orthorhombic  $3d^1$  perovskites. *Phys. Rev. Lett.*, 92:176403, Apr 2004.
- [38] Jan M. Tomczak, Ferdi Aryasetiawan, and Silke Biermann. Effective bandstructure in the insulating phase versus strong dynamical correlations in metallic vo<sub>2</sub>. *Phys. Rev. B*, 78:115103, Sep 2008.
- [39] J. Zaanen, G. A. Sawatzky, and J. W. Allen. Band gaps and electronic structure of transition-metal compounds. *Phys. Rev. Lett.*, 55:418–421, Jul 1985.

## Bibliography

---

- [40] Q. Huang, M. L. Foo, R. A. Pascal, J. W. Lynn, B. H. Toby, Tao He, H. W. Zandbergen, and R. J. Cava. Coupling between electronic and structural degrees of freedom in the triangular lattice conductor  $\text{Na}_x\text{CoO}_2$ . *Phys. Rev. B*, 70:184110, Nov 2004.
- [41] C. de Vaulx, M.-H. Julien, C. Berthier, S. Hébert, V. Pralong, and A. Maignan. Electronic correlations in  $\text{CoO}_2$ , the parent compound of triangular cobaltates. *Phys. Rev. Lett.*, 98:246402, Jun 2007.
- [42] G. Lang, J. Bobroff, H. Alloul, P. Mendels, N. Blanchard, and G. Collin. Evidence of a single nonmagnetic  $\text{Co}^{3+}$  state in the  $\text{Na}_1\text{CoO}_2$  cobaltate. *Phys. Rev. B*, 72:094404, Sep 2005.
- [43] M. Roger, D. J. P. Morris, D. A. Tennant, M. J. Gutmann, J. P. Goff, J. U. Hoffmann, R. Feyerherm, E. Dudzik, D. Prabhakaran, A. T. Boothroyd, N. Shannon, B. Lake, and P. P. Deen. Patterning of sodium ions and the control of electrons in sodium cobaltate. *Nature*, 445(7128):631–634, 02 2007.
- [44] H. W. Zandbergen, M. Foo, Q. Xu, V. Kumar, and R. J. Cava. Sodium ion ordering in  $\text{Na}_x\text{CoO}_2$ : Electron diffraction study. *Phys. Rev. B*, 70:024101, Jul 2004.
- [45] Maw Lin Foo, Yayu Wang, Satoshi Watauchi, H. W. Zandbergen, Tao He, R. J. Cava, and N. P. Ong. Charge ordering, commensurability, and metallicity in the phase diagram of the layered  $\text{Na}_x\text{CoO}_2$ . *Phys. Rev. Lett.*, 92:247001, Jun 2004.
- [46] G. Lang, J. Bobroff, H. Alloul, G. Collin, and N. Blanchard. Spin correlations and cobalt charge states: Phase diagram of sodium cobaltates. *Phys. Rev. B*, 78:155116, Oct 2008.
- [47] T. F. Schulze, M. Brühwiler, P. S. Häflicher, S. M. Kazakov, Ch. Niedermayer, K. Mattenberger, J. Karpinski, and B. Batlogg. Spin fluctuations, magnetic long-range order, and fermi surface gapping in  $\text{Na}_x\text{CoO}_2$ . *Phys. Rev. B*, 78:205101, Nov 2008.
- [48] J. Bobroff, G. Lang, H. Alloul, N. Blanchard, and G. Collin. Nmr study of the magnetic and metal-insulator transitions in  $\text{Na}_{0.5}\text{CoO}_2$ : A nesting scenario. *Phys. Rev. Lett.*, 96:107201, Mar 2006.
- [49] G. J. Shu and F. C. Chou. Ferrimagnetic ordering and spin entropy of field-dependent intermediate spins in  $\text{Na}_{0.82}\text{CoO}_2$ . *Phys. Rev. B*, 93:140402, Apr 2016.
- [50] T. A. Platova, I. R. Mukhamedshin, H. Alloul, A. V. Dooglav, and G. Collin. Nuclear quadrupole resonance and x-ray investigation of the structure of  $\text{Na}_{2/3}\text{CoO}_2$ . *Phys. Rev. B*, 80:224106, Dec 2009.
- [51] D.J. Singh, G.B. Wilson-Short, D. Kasinathan, M. Suewattana, and M. Fornari. Electronic structure and disorder in  $\text{Na}_x\text{CoO}_2$  and  $\text{SrRh}_2\text{O}_4$ . *Solid State Sciences*,

- 9(7):604 – 607, 2007. Bordeaux June 2006 1st International Symposium on structure-Property Relationships in Solid State Materials.
- [52] Peihong Zhang, Weidong Luo, Marvin L. Cohen, and Steven G. Louie. Fermi surface of  $\text{Na}_x\text{CoO}_2$ . *Phys. Rev. Lett.*, 93:236402, Nov 2004.
- [53] D. J. Singh. Electronic structure of  $\text{NaCo}_2\text{O}_4$ . *Phys. Rev. B*, 61:13397–13402, May 2000.
- [54] D. J. Singh. Quantum critical behavior and possible triplet superconductivity in electron-doped  $\text{CoO}_2$  sheets. *Phys. Rev. B*, 68:020503, Jul 2003.
- [55] M. Z. Hasan, Y.-D. Chuang, D. Qian, Y. W. Li, Y. Kong, A. Kuprin, A. V. Fedorov, R. Kimmerling, E. Rotenberg, K. Rossnagel, Z. Hussain, H. Koh, N. S. Rogado, M. L. Foo, and R. J. Cava. Fermi surface and quasiparticle dynamics of  $\text{Na}_{0.7}\text{CoO}_2$  investigated by angle-resolved photoemission spectroscopy. *Phys. Rev. Lett.*, 92:246402, Jun 2004.
- [56] H.-B. Yang, Z.-H. Pan, A. K. P. Sekharan, T. Sato, S. Souma, T. Takahashi, R. Jin, B. C. Sales, D. Mandrus, A. V. Fedorov, Z. Wang, and H. Ding. Fermi surface evolution and Luttinger theorem in  $\text{Na}_x\text{CoO}_2$ : A systematic photoemission study. *Phys. Rev. Lett.*, 95:146401, Sep 2005.
- [57] J. Geck, S. V. Borisenko, H. Berger, H. Eschrig, J. Fink, M. Knupfer, K. Koepernik, A. Koitzsch, A. A. Kordyuk, V. B. Zabolotnyy, and B. Büchner. Anomalous quasiparticle renormalization in  $\text{Na}_{0.73}\text{CoO}_2$ : Role of interorbital interactions and magnetic correlations. *Phys. Rev. Lett.*, 99:046403, Jul 2007.
- [58] D. Qian, L. Wray, D. Hsieh, L. Viciu, R. J. Cava, J. L. Luo, D. Wu, N. L. Wang, and M. Z. Hasan. Complete  $d$ -band dispersion relation in sodium cobaltates. *Phys. Rev. Lett.*, 97:186405, Nov 2006.
- [59] D. Qian, L. Wray, D. Hsieh, L. Viciu, R. J. Cava, J. L. Luo, D. Wu, N. L. Wang, and M. Z. Hasan. Complete  $d$ -band dispersion relation in sodium cobaltates. *Phys. Rev. Lett.*, 97:186405, Nov 2006.
- [60] H.-B. Yang, S.-C. Wang, A. K. P. Sekharan, H. Matsui, S. Souma, T. Sato, T. Takahashi, T. Takeuchi, J. C. Campuzano, R. Jin, B. C. Sales, D. Mandrus, Z. Wang, and H. Ding. Arpes on  $\text{Na}_{0.6}\text{CoO}_2$ : Fermi surface and unusual band dispersion. *Phys. Rev. Lett.*, 92:246403, Jun 2004.
- [61] T. Arakane, T. Sato, T. Takahashi, T. Fujii, and A. Asamitsu. Evidence for transition of Fermi-surface topology in highly doped  $\text{Na}_x\text{CoO}_2$ . *Phys. Rev. B*, 81:115132, Mar 2010.
- [62] T. Arakane, T. Sato, T. Takahashi, T. Fujii, and A. Asamitsu. Angle-resolved photoemission study of the doping evolution of a three-dimensional Fermi surface in  $\text{Na}_x\text{CoO}_2$ . *New Journal of Physics*, 13(4):043021, 2011.

## Bibliography

---

- [63] O. I. Motrunich and Patrick A. Lee. Possible effects of charge frustration in  $\text{Na}_x\text{CoO}_2$ : Bandwidth suppression, charge orders, and resurrected resonating valence bond superconductivity. *Phys. Rev. B*, 69:214516, Jun 2004.
- [64] Sen Zhou, Meng Gao, Hong Ding, Patrick A. Lee, and Ziqiang Wang. Electron correlation and fermi surface topology of  $\text{Na}_x\text{CoO}_2$ . *Phys. Rev. Lett.*, 94:206401, May 2005.
- [65] H. Ishida, M. D. Johannes, and A. Liebsch. Effect of dynamical coulomb correlations on the fermi surface of  $\text{Na}_{0.3}\text{CoO}_2$ . *Phys. Rev. Lett.*, 94:196401, May 2005.
- [66] C. A. Marianetti, G. Kotliar, and G. Ceder. Role of hybridization in  $\text{Na}_x\text{CoO}_2$  and the effect of hydration. *Phys. Rev. Lett.*, 92:196405, May 2004.
- [67] C. A. Marianetti and G. Kotliar. Na-induced correlations in  $\text{Na}_x\text{CoO}_2$ . *Phys. Rev. Lett.*, 98:176405, Apr 2007.
- [68] C. A. Marianetti, K. Haule, and O. Parcollet. Quasiparticle dispersion and heat capacity of  $\text{Na}_{0.3}\text{CoO}_2$ : A dynamical mean-field theory study. *Phys. Rev. Lett.*, 99:246404, Dec 2007.
- [69] Liebsch, A. and Ishida, H. Coulomb correlations do not fill the  $e'_g$  hole pockets in  $\text{Na}_{0.3}\text{CoO}_2$ . *Eur. Phys. J. B*, 61(4):405–411, 2008.
- [70] W. Koshibae and S. Maekawa. Electronic state of a  $\text{CoO}_2$  layer with hexagonal structure: A kagomé lattice structure in a triangular lattice. *Phys. Rev. Lett.*, 91:257003, Dec 2003.
- [71] G. Khaliullin, W. Koshibae, and S. Maekawa. Low energy electronic states and triplet pairing in layered cobaltate. *Phys. Rev. Lett.*, 93:176401, Oct 2004.
- [72] Giniyat Khaliullin and Ji ř Chaloupka. Origin of strong correlations and superconductivity in  $\text{Na}_x\text{CoO}_2$ . *Phys. Rev. B*, 77:104532, Mar 2008.
- [73] Sylvain Landron and Marie-Bernadette Lepetit. *Ab initio* evaluation of the local effective interactions in the superconducting compound  $\text{Na}_{0.35}\text{CoO}_2 \cdot 1.3\text{H}_2\text{O}$ . *Phys. Rev. B*, 74:184507, Nov 2006.
- [74] Sylvain Landron and Marie-Bernadette Lepetit. Importance of  $t_{2g}-e_g$  hybridization in transition metal oxides. *Phys. Rev. B*, 77:125106, Mar 2008.
- [75] A. Bourgeois, A. A. Aligia, T. Kroll, and M. D. Núñez Regueiro. Electronic structure and fermi-surface topology of  $\text{Na}_x\text{CoO}_2$ . *Phys. Rev. B*, 75:174518, May 2007.
- [76] A. Bourgeois, A. A. Aligia, and M. J. Rozenberg. Dynamical mean field theory of an effective three-band model for  $\text{Na}_x\text{CoO}_2$ . *Phys. Rev. Lett.*, 102:066402, Feb 2009.

- 
- [77] Oleg E. Peil, Antoine Georges, and Frank Lechermann. Strong correlations enhanced by charge ordering in highly doped cobaltates. *Phys. Rev. Lett.*, 107:236404, Nov 2011.
- [78] Frank Lechermann. Correlation effects on the doped triangular lattice in view of the physics of sodium-rich  $\text{Na}_x\text{CoO}_2$ . *Phys. Rev. Lett.*, 102:046403, Jan 2009.
- [79] Lewin Boehnke and Frank Lechermann. Competing orders in  $\text{Na}_x\text{CoO}_2$  from strong correlations on a two-particle level. *Phys. Rev. B*, 85:115128, Mar 2012.
- [80] L. Boehnke and F. Lechermann. Getting back to  $\text{Na}_x\text{CoO}_2$ : Spectral and thermoelectric properties. *physica status solidi (a)*, 211(6):1267–1272, 2014.
- [81] Aljoscha Wilhelm, Frank Lechermann, Hartmut Hafermann, Mikhail I. Katsnelson, and Alexander I. Lichtenstein. From hubbard bands to spin-polaron excitations in the doped mott material  $\text{Na}_x\text{CoO}_2$ . *Phys. Rev. B*, 91:155114, Apr 2015.
- [82] Qimiao Si and J. Llewellyn Smith. Kosterlitz-Thouless Transition and Short Range Spatial Correlations in an Extended Hubbard Model. *Physical Review Letters*, 77(16):3391, 1996.
- [83] Anirvan M Sengupta and Antoine Georges. Non-Fermi-liquid behavior near a  $T=0$  spin-glass transition. *Physical Review B*, 52(14):10295–10302, 1995.
- [84] Henrik Kajueter. *Interpolating Perturbation Scheme for Correlated Electron Systems*. PhD thesis, Rutgers University, 1996.
- [85] Ping Sun and Gabriel Kotliar. Extended dynamical mean-field theory and GW method. *Physical Review B*, 66(8):085120, aug 2002.
- [86] Ping Sun and Gabriel Kotliar. Many-body approximation scheme beyond GW. *Physical Review Letters*, 92:196402, 2004.
- [87] A. I. Lichtenstein and M. I. Katsnelson. Antiferromagnetism and  $\mathbf{d}$ -wave superconductivity in cuprates: A cluster dynamical mean-field theory. *Phys. Rev. B*, 62:R9283–R9286, Oct 2000.
- [88] Gabriel Kotliar, Sergej Y. Savrasov, Gunnar Pálsson, and Giulio Biroli. Cellular dynamical mean field approach to strongly correlated systems. *Phys. Rev. Lett.*, 87:186401, Oct 2001.
- [89] Kieron Burke. *The ABC of DFT*. [dft.uci.edu/doc/g1.pdf](http://dft.uci.edu/doc/g1.pdf), 2007.
- [90] J. P. Perdew and Alex Zunger. Self-interaction correction to density-functional approximations for many-electron systems. *Phys. Rev. B*, 23(10):5048, 1981.
- [91] D. M. Ceperley and B. J. Alder. Ground state of the electron gas by a stochastic method. *Phys. Rev. Lett.*, 45(7):566, 1980.

## Bibliography

---

- [92] John P. Perdew, Kieron Burke, and Matthias Ernzerhof. Generalized gradient approximation made simple. *Phys. Rev. Lett.*, 77:3865–3868, Oct 1996.
- [93] Erich Runge and E. K. U. Gross. Density-functional theory for time-dependent systems. *Phys. Rev. Lett.*, 52:997–1000, Mar 1984.
- [94] C.A. Ullrich et A.D. C.A. Ullrich and A.D. Bandrauk. *Fundamentals of Time-Dependent Density-Functional Theory*, volume Lecture Notes in Physics 837, chapter Atoms and Molecules in strong Laser Fields. Springer, 2012.
- [95] Silke Biermann. Dynamical mean field theory-based electronic structure calculations for correlated materials. In Springer, editor, *Topics in current chemistry*, volume 347, pages 303–345, 2014.
- [96] Gabriel Kotliar and Dieter Vollhardt. Strongly correlated materials: Insights from dynamical mean field theory. *Physics Today*, page 53, March 2004.
- [97] John W. Negele and Henri Orland. *Quantum many-particle systems*. Addison-Wesley New York, 1988.
- [98] Walter Metzner and Dieter Vollhardt. Correlated lattice fermions in  $d = \infty$  dimensions. *Phys. Rev. Lett.*, 62:324–327, Jan 1989.
- [99] Thomas Ayrál, Silke Biermann, and Philipp Werner. Screening and nonlocal correlations in the extended hubbard model from self-consistent combined  $gw$  and dynamical mean field theory. *Phys. Rev. B*, 87:125149, Mar 2013.
- [100] J. Hubbard. Calculation of partition functions. *Phys. Rev. Lett.*, 3:77–78, Jul 1959.
- [101] Matteo Gatti, Valerio Olevano, Lucia Reining, and Ilya V. Tokatly. Transforming nonlocality into a frequency dependence: A shortcut to spectroscopy. *Phys. Rev. Lett.*, 99:057401, Aug 2007.
- [102] Lars Hedin. New method for calculating the one-particle green’s function with application to the electron-gas problem. *Phys. Rev.*, 139:A796–A823, Aug 1965.
- [103] S. Biermann, F. Aryasetiawan, and A. Georges. First-Principles Approach to the Electronic Structure of Strongly Correlated Systems: Combining the GW Approximation and Dynamical Mean-Field Theory. *Physical Review Letters*, 90(8):086402, 2003.
- [104] P. Hansmann, T. Ayrál, L. Vaugier, P. Werner, and S. Biermann. Long-range coulomb interactions in surface systems: A first-principles description within self-consistently combined  $gw$  and dynamical mean-field theory. *Phys. Rev. Lett.*, 110:166401, Apr 2013.

- 
- [105] Takao Kotani, Mark van Schilfgaarde, and Sergey V. Faleev. Quasiparticle self-consistent  $gw$  method: A basis for the independent-particle approximation. *Phys. Rev. B*, 76:165106, Oct 2007.
- [106] F. Lechermann, A. Georges, A. Poteryaev, S. Biermann, M. Posternak, A. Yamasaki, and O. K. Andersen. Dynamical mean-field theory using wannier functions: A flexible route to electronic structure calculations of strongly correlated materials. *Phys. Rev. B*, 74:125120, Sep 2006.
- [107] Markus Aichhorn, Leonid Pourovskii, Veronica Vildosola, Michel Ferrero, Olivier Parcollet, Takashi Miyake, Antoine Georges, and Silke Biermann. Dynamical mean-field theory within an augmented plane-wave framework: Assessing electronic correlations in the iron pnictide lafeaso. *Phys. Rev. B*, 80:085101, Aug 2009.
- [108] Thomas Ayral, Philipp Werner, and Silke Biermann. Spectral properties of correlated materials: Local vertex and nonlocal two-particle correlations from combined  $gw$  and dynamical mean field theory. *Phys. Rev. Lett.*, 109:226401, Nov 2012.
- [109] A. Camjayi, K. Haule, V. Dobrosavljevic, and G. Kotliar. Coulomb correlations and the wigner-mott transition. *Nat Phys*, 4(12):932–935, 12 2008.
- [110] Chisa Hotta and Nobuo Furukawa. Strong coupling theory of the spinless charges on triangular lattices: Possible formation of a gapless charge-ordered liquid. *Phys. Rev. B*, 74:193107, Nov 2006.
- [111] Chisa Hotta and Nobuo Furukawa. Filling dependence of a new type of charge ordered liquid on a triangular lattice system. *Journal of Physics: Condensed Matter*, 19(14):145242, 2007.
- [112] Mitake Miyazaki, Chisa Hotta, Shin Miyahara, Keisuke Matsuda, and Nobuo Furukawa. Variational monte carlo study of a spinless fermion  $t$ - $v$  model on a triangular lattice: Formation of a pinball liquid. *Journal of the Physical Society of Japan*, 78(1):014707, 2009.
- [113] Stefan Wessel and Matthias Troyer. Supersolid hard-core bosons on the triangular lattice. *Phys. Rev. Lett.*, 95:127205, Sep 2005.
- [114] Dariush Heidarian and Kedar Damle. Persistent supersolid phase of hard-core bosons on the triangular lattice. *Phys. Rev. Lett.*, 95:127206, Sep 2005.
- [115] R. G. Melko, A. Paramekanti, A. A. Burkov, A. Vishwanath, D. N. Sheng, and L. Balents. Supersolid order from disorder: Hard-core bosons on the triangular lattice. *Phys. Rev. Lett.*, 95:127207, Sep 2005.
- [116] Xue-Feng Zhang, Raoul Dillenschneider, Yue Yu, and Sebastian Eggert. Supersolid phase transitions for hard-core bosons on a triangular lattice. *Phys. Rev. B*, 84:174515, Nov 2011.

## Bibliography

---

- [117] L. Cano-Cortés, A. Ralko, C. Février, J. Merino, and S. Fratini. Geometrical frustration effects on charge-driven quantum phase transitions. *Phys. Rev. B*, 84:155115, Oct 2011.
- [118] Luca F. Tocchio, Claudius Gros, Xue-Feng Zhang, and Sebastian Eggert. Phase diagram of the triangular extended hubbard model. *Phys. Rev. Lett.*, 113:246405, Dec 2014.
- [119] Ryui Kaneko, Luca F. Tocchio, Roser Valentí, Federico Becca, and Claudius Gros. Spontaneous symmetry breaking in correlated wave functions. *Phys. Rev. B*, 93:125127, Mar 2016.
- [120] Ryui Kaneko, Luca F. Tocchio, Roser Valentí, and Claudius Gros. Emergent lattices with geometrical frustration in doped extended hubbard models. arXiv:1606.06520, June 2016.
- [121] Christoph Piefke, Lewin Boehnke, Antoine Georges, and Frank Lechermann. Considerable nonlocal electronic correlations in strongly doped  $\text{Na}_x\text{CoO}_2$ . *Phys. Rev. B*, 82:165118, Oct 2010.
- [122] V I Anisimov, A I Poteryaev, M A Korotin, A O Anokhin, and G Kotliar. First-principles calculations of the electronic structure and spectra of strongly correlated systems: dynamical mean-field theory. *Journal of Physics: Condensed Matter*, 9(35):7359, 1997.
- [123] Vladimir I Anisimov, F Aryasetiawan, and A I Lichtenstein. First-principles calculations of the electronic structure and spectra of strongly correlated systems: the lda + u method. *Journal of Physics: Condensed Matter*, 9(4):767, 1997.
- [124] A. I. Lichtenstein and M. I. Katsnelson. *Ab initio* calculations of quasiparticle band structure in correlated systems: Lda++ approach. *Phys. Rev. B*, 57:6884–6895, Mar 1998.
- [125] Nicola Marzari and David Vanderbilt. Maximally localized generalized wannier functions for composite energy bands. *Phys. Rev. B*, 56:12847–12865, Nov 1997.
- [126] Ivo Souza, Nicola Marzari, and David Vanderbilt. Maximally localized wannier functions for entangled energy bands. *Phys. Rev. B*, 65:035109, Dec 2001.
- [127] F. Aryasetiawan, M. Imada, A. Georges, G. Kotliar, S. Biermann, and A. I. Lichtenstein. Frequency-dependent local interactions and low-energy effective models from electronic structure calculations. *Phys. Rev. B*, 70:195104, Nov 2004.
- [128] Loïc Vaugier. *Electronic Structure of Correlated Materials from First-Principles: Hubbard interaction and Hund’s exchange*. PhD thesis, Ecole polytechnique, 2011.

- 
- [129] Loïc Vaugier, Hong Jiang, and Silke Biermann. Hubbard  $u$  and hund exchange  $j$  in transition metal oxides: Screening versus localization trends from constrained random phase approximation. *Phys. Rev. B*, 86:165105, Oct 2012.
- [130] Thomas Ayrál. *Nonlocal Coulomb Interactions and Electronic Correlations: Novel Many-Body Approaches*. PhD thesis, Ecole polytechnique, Sept. 2015.
- [131] A. N. Rubtsov, M. I. Katsnelson, and A. I. Lichtenstein. Dual boson approach to collective excitations in correlated fermionic systems. *Annals of Physics*, 327:1320, may 2012.
- [132] Philipp Werner, Armin Comanac, Luca de' Medici, Matthias Troyer, and Andrew Millis. Continuous-Time Solver for Quantum Impurity Models. *Physical Review Letters*, 97(7):076405, aug 2006.
- [133] Philipp Werner, Emanuel Gull, Olivier Parcollet, and Andrew J. Millis. Momentum-selective metal-insulator transition in the two-dimensional Hubbard model: An 8-site dynamical cluster approximation study. *Physical Review B*, 80(4):045120, 2009.
- [134] Hartmut Hafermann, Kelly R. Patton, and Philipp Werner. Improved estimators for the self-energy and vertex function in hybridization-expansion continuous-time quantum Monte Carlo simulations. *Physical Review B*, 85(20):205106, 2012.
- [135] Ambroise van Roekeghem. *Electronic Coulomb Correlations in Transition Metal Pnictides*. PhD thesis, Ecole polytechnique, 2014.
- [136] R. K. Bryan. Maximum entropy analysis of oversampled data problems. *European Biophysics Journal*, pages 165–174, 1990.
- [137] A. Amaricci, A. Camjayi, K. Haule, G. Kotliar, D. Tanasković, and V. Dobrosavljević. Extended hubbard model: Charge ordering and wigner-mott transition. *Phys. Rev. B*, 82:155102, Oct 2010.
- [138] M. M. Radonjić, D. Tanasković, V. Dobrosavljević, K. Haule, and G. Kotliar. Wigner-mott scaling of transport near the two-dimensional metal-insulator transition. *Phys. Rev. B*, 85:085133, Feb 2012.
- [139] Erik GCP van Loon, Friedrich Krien, Hartmut Hafermann, Evgeny A Stepanov, Alexander I Lichtenstein, and Mikhail I Katsnelson. Double occupancy in dynamical mean-field theory and the dual boson approach. *Physical Review B*, 93(15):155162, 2016.
- [140] E.K.U. Gross, F.J. Dobson, and M. Petersilka. *Density Functional Theory*. Springer, New York, 1996.
- [141] Thomas Ayrál. Private communication, 2016.

## Bibliography

---

- [142] E. Wigner. On the interaction of electrons in metals. *Phys. Rev.*, 46:1002–1011, Dec 1934.
- [143] A. Toschi, A. A. Katanin, and K. Held. Dynamical vertex approximation: A step beyond dynamical mean-field theory. *Phys. Rev. B*, 75:045118, Jan 2007.
- [144] Thomas Ayrál and Olivier Parcollet. Mott physics and spin fluctuations: A unified framework. *Phys. Rev. B*, 92:115109, Sep 2015.
- [145] Thomas Ayrál and Olivier Parcollet. Mott physics and spin fluctuations: A functional viewpoint. *Phys. Rev. B*, 93:235124, Jun 2016.
- [146] G. Kresse and J. Furthmüller. Efficiency of ab-initio total energy calculations for metals and semiconductors using a plane-wave basis set. *Comput. Mater. Sci.*, 6(1):15, 1996.
- [147] G. Kresse and J. Furthmüller. Efficient iterative schemes for *ab initio* total-energy calculations using a plane-wave basis set. *Phys. Rev. B*, 54(16):11169, 1996.
- [148] P. E. Blöchl. Projector augmented-wave method. *Phys. Rev. B*, 50(24):17953, 1994.
- [149] G. Kresse and D. Joubert. From ultrasoft pseudopotentials to the projector augmented-wave method. *Phys. Rev. B*, 59(3):1758, 1999.
- [150] John P. Perdew, Kieron Burke, and Matthias Ernzerhof. Generalized gradient approximation made simple [phys. rev. lett. 77, 3865 (1996)]. *Phys. Rev. Lett.*, 78:1396–1396, Feb 1997.
- [151] A. G. Marinopoulos, Lucia Reining, Angel Rubio, and Valerio Olevano. *Ab initio* study of the optical absorption and wave-vector-dependent dielectric response of graphite. *Phys. Rev. B*, 69:245419, Jun 2004.
- [152] M. Shishkin and G. Kresse. Implementation and performance of the frequency-dependent gw method within the paw framework. *Phys. Rev. B*, 74(3):035101, 2006.
- [153] Jan M. Tomczak, Michele Casula, Takashi Miyake, Ferdi Aryasetiawan, and Silke Biermann. Combined gw and dynamical mean-field theory: Dynamical screening effects in transition metal oxides. *EPL (Europhysics Letters)*, 100(6):67001, 2012.
- [154] Jan M. Tomczak, M. Casula, T. Miyake, and S. Biermann. Asymmetry in band widening and quasiparticle lifetimes in srvo<sub>3</sub>: Competition between screened exchange and local correlations from combined gw and dynamical mean-field theory gw + DMFT. *Phys. Rev. B*, 90:165138, Oct 2014.
- [155] Philipp Werner, Michele Casula, Takashi Miyake, Ferdi Aryasetiawan, Andrew J. Millis, and Silke Biermann. Satellites and large doping and temperature dependence of electronic properties in hole-doped bafe<sub>2</sub>as<sub>2</sub>. *Nat Phys*, 8(4):331–337, 04 2012.

- [156] Michele Casula, Alexey Rubtsov, and Silke Biermann. Dynamical screening effects in correlated materials: Plasmon satellites and spectral weight transfers from a green's function ansatz to extended dynamical mean field theory. *Phys. Rev. B*, 85:035115, Jan 2012.
- [157] Matteo Gatti and Matteo Guzzo. Dynamical screening in correlated metals: Spectral properties of  $\text{SrVO}_3$  in the  $gw$  approximation and beyond. *Phys. Rev. B*, 87:155147, Apr 2013.
- [158] Philipp Werner, Rei Sakuma, Fredrik Nilsson, and Ferdi Aryasetiawan. Dynamical screening in  $\text{La}_2\text{CuO}_4$ . *Phys. Rev. B*, 91:125142, Mar 2015.
- [159] H. Ehrenreich and M. H. Cohen. Self-consistent field approach to the many-electron problem. *Phys. Rev.*, 115(4):786, 1959.
- [160] M. Gajdoš, K. Hummer, G. Kresse, J. Furthmüller, and F. Bechstedt. Linear optical properties in the projector-augmented wave methodology. *Phys. Rev. B*, 73(4):045112, 2006.





**Titre :** Etude des cobaltates fortement dopés par calculs premiers principes et théorie du champ moyen dynamique étendue

**Mots clefs :** Corrélations électroniques, Simulations *ab initio*, Oxydes de cobalt

**Résumé :** Les cobaltates dopés au sodium,  $\text{Na}_x\text{CoO}_2$ , présentent un riche diagramme de phase en fonction du dopage. Dans cette thèse, nous nous intéressons à la structure électronique du composé fortement dopé  $x = 2/3$ . Afin de traiter ce problème complexe, nous combinons une approche sur modèle et une approche *ab initio*.

Nous examinons d'abord l'effet des corrélations électroniques au niveau d'un modèle de Hubbard étendu sur réseau triangulaire par la théorie du champ moyen dynamique étendue. Cette approche permet d'identifier une phase métallique, une transition vers une phase ordonnée de charge, et, curieusement, une région où l'interaction de Coulomb

écranée statique devient attractive.

Nous complétons cette étude en clarifiant les détails microscopiques du matériau réel à l'aide de simulations *ab initio*. En particulier, nous étudions l'effet du dopage au sodium, de la structure cristalline ou du magnétisme sur la structure de bandes électronique. Puis nous calculons la susceptibilité de charge selon les premiers principes en nous appuyant sur les résultats de l'étude sur modèle.

En conclusion, nous discutons comment combiner les approches sur modèle et *ab initio* pour prédire les propriétés électroniques de matériaux complexes tels que les oxydes.

**Title :** Cobaltates in the high-doping regime: Insights from first-principles calculations and extended dynamical mean-field theory

**Keywords :** Electronic correlations, *Ab initio* calculations, Cobalt oxides

**Abstract :** Sodium-doped cobaltates,  $\text{Na}_x\text{CoO}_2$ , display a rich phase diagram as a function of doping. In this thesis, we focus on the electronic structure of the  $x = 2/3$ , strongly-doped compound. In order to treat this complex problem, we combine a model and an *ab initio* approach.

We first study the effects of electronic correlations on an extended Hubbard model on a triangular lattice using the extended dynamical mean-field theory. We identify a metallic phase, a transition to a charge-ordered phase, and, surprisingly, a region with an attractive static screened Coulomb

interaction.

Next, we clarify the microscopic details of the real material with *ab initio* simulations. In particular, we study the effect of sodium doping, of the crystalline arrangement and of magnetism on the electronic band structure. We compute the charge susceptibility from first principles, based on the results from the model study.

As a conclusion, we discuss how to combine model and *ab initio* approaches to predict the electronic properties of complex materials, such as oxides.